NASA Contractor Report 145359

Experimental Assessment of Theory for Refraction of Sound by a Shear Layer

Robert H. Schlinker and Roy K. Amiet

United Technologies Research Center
East Hartford, Connecticut 06108

Contract NAS1-14973
June 1978

NASA
National Aeronautics and
Space Administration

Langley Research Center
Hampton, Virginia 23665

Experimental Assessment of Theory for Refraction of Sound by a Shear Layer

TABLE OF CONTENTS

Page

TABLE OF CONTENTS (Cont'd)

EXPERIMENTAL ASSESSMENT OF THEORY FOR REFRACTION OF SOUND BY A SHEAR LAYER

By

Robert H. Schlinker and Roy K. Amiet

SUMMARY

A theoretical and experimental investigation was conducted to determine the refraction angle and amplitude changes associated with sound transmission through a circular, open-jet shear layer. Experiments were performed using a 0.91 m diameter open jet in the United Technologies Research Center (UTRC) Acoustic Research Tunnel. Free stream Mach number was varied from 0.1 to 0.4.

For measurements directed toward assessment of the refraction angle correction, a discrete tone acoustic source with a frequency range of 1 kHz to 10 kHz, was situated in the airstream. Sound wave front angle change was measured for several axial source locations and two off-axis source positions. Refraction was observed to be significant at Mach numbers of 0.1 and greater. The experimental results were compared with an existing refraction theory which was extended in the present study to account for off-axis source positions.

Good agreement between the refraction angle correction theory and experiment was obtained over the test Mach number, frequency and angle measurement range for all on-axis acoustic source locations. For off-axis source positions, good agreement was obtained at a source-to-shear layer separation distance greater than the jet radius. Measureable differences between theory and experiment occurred at a source-to-shear layer separation distance less than one jet radius. This disagreement, at present, is not viewed as a failure of the theoretical angle correction. Rather, it is believed due to the sensitivity of the experimental method to small changes in the assumed zero-thickness shear layer position at small source-to-shear layer separation distance. As previously predicted, experimental results indicate that axial variations in shear layer thickness and shear layer divergence need not be included in the refraction correction procedure. The frequency independence of the analysis was also verified.

Theory for the refraction amplitude change associated with sound transmission through a shear layer could not be verified due to limitations of the experimental technique. Indirect verification of the theory, however, was achieved over a limited range of frequency and Mach numbers using previously published experimental results.

A shear layer turbulence scattering experiment was conducted at 90° to the open jet axis for the same freestream Mach numbers and axial source locations used in the refraction study. Significant discrete tone spectrum broadening and tone amplitude changes were observed at open jet Mach numbers above 0.2 and at acoustic source frequencies greater than 5 kHz. More severe turbulence scattering was observed for downstream source locations. Consequently, sound radiated at angles close to the jet axis will encounter greater turbulence scattering than that radiated at 90° to the open jet.

INTRODUCTION

Open jet acoustic test facilities are currently used to investigate the effect of forward flight on aeroacoustic noise mechanisms. The technique permits studying a wide variety of problems such as airframe noise, model propeller and rotor noise, isolated airfoil and blown flap noise, and jet noise forward flight effects. For tests conducted at free stream Mach numbers less than 0.1, measurements outside the airstream can be used to directly infer the source noise characteristics. However, at higher Mach numbers, the open jet technique is susceptible to errors due to the presence of the shear layer through which the sound is transmitted. The shear layer serves to refract, reflect, and scatter the sound radiated from the model. These effects significantly alter the acoustic source directivity pattern and hence alter the conclusions drawn from a particular experiment.

The lack of a firm understanding of these effects has created a clear need for a validated shear layer correction procedure. The present study was undertaken to experimentally assess the refraction angle change due to propagation through a shear layer with a lesser effort devoted to the refraction amplitude change. Existing refraction theory was extended to treat the case of an off-axis source. Both on-axis and off-axis acoustic source locations were tested for a circular jet geometry. Acoustic source frequency and jet Mach number were also varied to evaluate the dependence on these parameters If the thoery could be validated, a correction procedure would be available for reducing far-field noise data acquired in open jet test facilities.

Previous Theoretical Investigations

Because the use of open jet wind tunnels for determining the acoustic radiation properties of test models is a relatively new technique, methods have only recently become available for correcting the acoustic data obtained in such a facility for the effects of refraction. However, the refraction problem had received previous attention because of its importance in the jet noise problem. The case of refraction of a plane sound wave by a plane, zero thickness shear layer was first correctly treated by Ribner (ref. 1) and Miles (ref. 2). Gottlieb (ref. 3) extended the analysis to the case of a point source beneath a plane shear layer. Graham and Graham (ref. 4) considered the problem of a plane wave interacting with a finite thickness shear layer and subsequent publications of theirs consider the field of specific singularities near a shear layer. Amiet (ref. 5) and others also considered the sound field of specific source types near a shear layer.

The above studies were not concerned with correcting acoustic wind tunnel data, however, and further analysis of the problem was needed. In particular, a method was required which made no assumptions regarding the nature of the sources (e.g., monopole, dipole, etc.), since, in general, the nature and distribution of sources in a given test are unknown. Subsequently, Amiet (ref. 6) derived a correction procedure which applied both an angle change and an amplitude change to the data. This assumed a plane zero thickness shear layer. It was only by this separation of angle and amplitude effects that it was possible to arrive at a correction independent of source type. The problem was also analyzed by Jacques (ref. 7) who arrived at the same result for refraction by a plane shear layer, and also considered the case of a source on the centerline of a cylindrical shear layer of zero thickness. The solution for refraction by a thick cylindrical shear layer with a source on the centerline was given by Tester and Morfey (ref. 8) and for a thick plane shear layer by Amiet (ref. 9). This work of Amiet also gives a review of the several correction procedures.

The above corrections are in algebraic closed form. Candel (ref. 10) recently developed a numerical ray tracing procedure which appears to give results very close to the closed form solutions. Recent studies by Tester and Burrin (ref. 11) indicate that the axial variation of the shear layer has little effect on the refraction corrections. Thus, it is possible to model the open jet shear layer without axial variations.

References 6-11, above, rely on the technique of correcting both angle and amplitude. Mani (ref. 12) employed a different approach to the problem, but this appears to be less well established than the above mentioned techniques of correcting angle and amplitude.

Previous Experimental Investigations

Few experimental studies exist documenting the shear layer refraction and scattering characteristics. Amiet (ref. 6) reported the results of an exploratory experiment for the angle correction which tended to support the theoretical predictions in reference 6. Candel et al. (ref. 13) provided an experimental assessment of a refraction theory in addition to presenting preliminary results for turbulence scattering in an open jet. Similarly, Ahuja et al. (ref. 14) recently reported an assessment of the refraction theory of reference 11. Also included was an exploratory study of turbulence scattering at low jet Mach numbers and low acoustic source frequencies. All of the above experimental investigations were limited to on-axis source locations.

Method of Approach

In the present study, the refraction angle change was assessed by cross-correlating far-field microphones to measure the local sound wavefront propagation angle outside the open jet. Knowing the propagation angle, the acoustic ray normal to the wavefront was traced back to the shear layer crossing point. In determining this point, the shear layer was assumed to be cylindrical with a radius equal to the inlet nozzle radius and to have zero thickness. From this, the original propagation angle inside the shear layer was determined for comparison with refraction angle correction theory. The original analysis of Amiet presented in references 6 and 9 was extended here to accommodate off-axis acoustic source locations. The refraction amplitude correction was assessed with a dipole acoustic source located in the open jet airstream. The difference between the measured far-field tone directivity and the theoretical dipole directivity pattern inside the jet represents the amplitude correction. Here, the theoretical angle correction was used to link propagation angles inside and outside the airstream. The experimental amplitude corrections were then compared to the refraction theory discussed later.

A simple experiment was also conducted to assess the importance of turbulence scattering. A discrete tone was used to investigate spectrum broadening effects as well as changes in the tone amplitude. Various frequencies and Mach numbers were employed to determine when scattering effects become significant. The importance of turbulence length scale changes on the scattering phenomenon was also investigated by locating the acoustic source at various axial stations.

LIST OF SYMBOLS

A	Cross-sectional area of ray tube
a	Radius of tunnel
AMP	Amplitude correction function
B_1, B_2	Discrete tone amplitude measured at microphones, m_1, m_2
c_o	Sound speed
C_1	Constant in amplitude correction function
D/Dt	$\partial/\partial t + U\, \partial/\partial x$
$d\underline{\ell}$	Vector defining side of ray tube
f	Acoustic source frequency, Hz
G_1, G_2	Microphone sensitivity
g	$1- h/a$
H	Cross-correlation amplitude
h	Source-to-shear layer distance. Also corresponds to source-to-lip-line distance.
h'	Distance between source and quarter velocity point in shear layer
$\hat{i}$, $\hat{j}$, $\hat{k}$	Unit vectors in x, y, z directions
$\bar{k}$	Normalized by ω/c_o
k_x, k_y, k_z	x, y or z wavenumber
ℓ	Microphone separation distance
M	Mach number of stream
m_1, m_2	Denote far-field microphones
$\hat{n}_e$	Unit vector from retarded source position to shear layer crossing point

LIST OF SYMBOLS (Cont'd)

$\hat{n}_1$, $\hat{n}_2$	Unit vector along ray path beneath shear layer and above shear layer, respectively
P	Pressure
P_1', P_2'	Random noise measured at microphones m_1, m_2
R	Reflection coefficient
R_o	Inlet nozzle radius, 0.455 m
R, $R_{1/2}$	Local radius and radius of half velocity line ($U/U_o = 0.5$) in shear layer
r	Source - observer distance
r_1	Distance from source-to-shear layer crossing point
r_2	Distance from shear layer crossing point to far field
S	Cross-correlation function
SPL	Sound pressure level
T	Transmission coefficient
t	Time
U , U_o	Local stream velocity in shear layer and potential core velocity
V	Voltage signal
w	z component of perturbation velocity
X_o	Acoustic ray shear layer crossing point
X, Y	Axial and transverse coordinates in the horizontal plane coinciding with open jet axis
x, y, z	Cartesian coordinates rotated by α from x, y', z'
x, y', z'	Cartesian coordinates fixed to laboratory frame

LIST OF SYMBOLS (Cont'd)

α	Angle made by tangent plane
β^2	$1- M^2$
γ	$\varphi + \alpha$
Δ_p	Phase lag between speaker output and acoustic signal arriving at microphone
Δr	Difference between source to individual microphone distances
Δ, Δ'	Phase difference between microphones due to propagation path length differences at $M = 0$ and $M \neq 0$
Δ_1, Δ_2	Phase lag between individual microphone input and output
Δ_a, Δ_s	Signal phase lag between input and output of amplifier and speaker
Δ_T, Δ_T'	Total phase difference between microphone output signals at $M = 0$ and $M \neq 0$
δ	Shear layer thickness
ζ^2	$(1- M \cos \theta)^2 - \cos^2\theta$
η_1, η_2	Phase difference between individual microphones
$\boldsymbol{\Theta}$	$k_x x + k_y y - \omega t$
θ	Polar angle
θ_m	Far field microphone measurement angle
Λ	Total phase lag between signal generator and acoustic signal arriving at microphone
μ_o, μ_1	Angle between microphone array and wavefront at $M = 0$ and $M \neq 0$
ρ	Density
τ	Cross-correlation function delay time

LIST OF SYMBOLS (Cont'd)

Φ	Velocity potential
ϕ	Polar angle
ω	Radian frequency
$< >$	Time average of fluctuating signal

Subscripts

i	Incident
v	Reflected
t	Transmitted
c	Corrected
m	Measured

DESCRIPTION OF THE EXPERIMENT

Acoustic Research Tunnel

The experimental study was conducted in the UTRC Acoustic Research Tunnel. A detailed description of the facility is given in reference 15. The tunnel, shown schematically in figure 1 is an open-circuit, open-jet design. The inlet is provided with a high length-to-diameter ratio honeycomb section and a series of turbulence suppression screens. These features, in conjunction with a large tunnel contraction, provide a spatially uniform, temporally steady flow with a controlled test section turbulence level of approximately 0.2 percent. An inlet nozzle with a radius, $R_o = 0.455$ m, was employed in the present test program. Turbulence generators and grids can be inserted upstream of the nozzle to provide various wake profiles (ref. 16) and a range of turbulence levels (ref. 17) in the test section.

The open jet test section is surrounded by a sealed anechoic chamber 4.9 m high, 5.5 m long (axial direction,), and 6.7 m wide. The interior walls of the chamber, shown in figure 2, are lined with 0.3 m fiberglass wedges. The chamber has been found to be anechoic (ref. 15) for broadband noise over a 200 Hz to 20 kHz range of calibration frequencies. That is, the sound pressure followed a 6 dB decay curve per doubling of source-observer separation distance within approximately 1/2 dB over this frequency range.

Since pure tone source frequencies were used in the present experiment, intensity versus distance calibration measurements were made to verify the free field behavior. For these tests a speaker was located on the centerline of the open jet test section. A microphone was traversed radially outwards from the acoustic source at various angles to the jet axis. Figure 3 shows a typical result at 90° to the jet centerline. The intensity changes followed the inverse-square law decreasing approximately 6 dB with doubling of distance over the 1 kHz to 10 kHz frequency range. Similar results were obtained at f = 12.5, 16, 20 and 25 kHz. These tests verified the anechoic characteristics of the facility for pure tones over the frequency range employed in the present study. It should be noted that a pure tone provides a more severe test for evaluating free field characteristics than random noise.

The test section airflow enters the diffuser by a collector that has anechoic treatment on its flow impingement lip. Initial facility tests reported in reference 15 identified an acoustic coupling between the inlet nozzle and the collector lip resulting in edge tones at high tunnel speeds. To suppress this noise mechanism, triangular tabs (see figure 4) were distributed around the nozzle periphery to disturb the azimuthal symmetry of the shear layer and prevent the generation of feedback tones. On the other hand, the shear layer thickness is increased by the tabs as will be discussed in the section on Shear Layer Growth. Despite this alteration of shear layer width, the measured angle change associated with the wavefront propagation through the finite thickness shear layer showed good agreement with the change calculated using the circular vortex sheet theory developed in the present study.

The diffuser in figure 1 operates unstalled and is thus not a major source of background noise. To avoid tunnel fan noise from propagating upstream into the anechoic chamber a Z-shaped muffling section with two right angle bends and parallel treated baffles is located between the diffuser and the fan. The 1500 hp centrifugal fan exhausts to the atmosphere through an exhaust tower.

Tunnel speed is determined from total pressure measurements at the contraction inlet and static pressure measurements within the sealed anechoic chamber. Since losses are confined to the boundary layer, total pressure upstream and downstream of the contraction are predicted and have been verified, to be equal. The test section velocity has been shown to be temporally steady.

Experimental Arrangement

Refraction Angle Correction Experiment - Figures 2 and 4 show the anechoic chamber test arrangement employed for the angle correction measurements. The nozzle inlet and collector described earlier are evident in the photos.

An acoustic source, consisting of a speaker enclosed by an aerodynamic fairing (see fig. 4), was located in the open jet airstream. The fairing measurements were: 17 cm long (axial direction), 10 cm high, and 5 cm deep. Leading and trailing edges of the fairing were rounded. The wake shed by the body produced no significant discrete vortex shedding tones in the far-field acoustic spectrum. Broadband wake noise did not influence the present experiment which employed only pure tones.

The speaker fairing was held in place by a support arm which extended through the open jet to a rigid stand outside the flow. The support arm consisted of a short section of cylindrical tubing and an aerodynamically shaped fairing. Although the cylinder generated an aeolian tone, the dipole radiation pattern was in a vertical direction perpendicular to the horizontal plane containing the speaker and the far-field microphones. Therefore this extraneous noise mechanism was not sensed. Similarly, noise generated by impingement of the highly turbulent shear layer on the aerodynamic fairing radiated in a vertical direction and was not sensed by the far-field microphones. Acoustic insulation was applied to the support stand and the exterior of the inlet nozzle.

The speaker face, with its 2.5 cm diameter aperture, was covered with a plastic grid of the same aperture size. The grid prevented flow separation and distortion of the mean velocity field at the speaker-flow interface. The center of the grid aperture marked the acoustic source position. All far-field microphone locations were referenced to this station.

The acoustic wavefront angle outside the open jet was measured by a pair of far-field microphones. The microphones, designated as m_1, and m_2 in figures 4 and 5, were mounted at grazing incidence on a rotating boom. The boom pivot point, located beneath the open jet, was aligned with the acoustic source position. Although figure 5 shows the source situated on the tunnel centerline, off-centerline stations were also investigated. The microphones scanned a horizontal plane at the same height as the tunnel centerline and the acoustic source. Different microphone separation distances, ℓ, were used depending on the acoustic source frequency. The fixed microphone radius, r = 1.83 m, was measured to the midpoint of the microphone array. The radius was selected to permit scanning the boom close to the jet axis while still maintaining a large separation distance between the microphones and the downstream collector. This avoided potential near field reverberation problems when the acoustic source was situated at the furthest downstream location. The microphones were mounted rigidly using guy wires and braces to minimize any vibration or deflection when the open jet was operated.

The boom angular position was defined by the angle, θ_m, measured from the downstream jet axis. The angle was referenced to the midpoint between the two microphones. A line connecting the microphones formed approximately a 90^o angle with the radius, r. A potentiometer, attached to the boom pivot shaft, provided a voltage output corresponding to the boom angular position. The voltage was amplified and displayed on a digital voltage readout providing a resolution of 0.016 deg. The system was calibrated daily using the open jet centerline and a line perpendicular to the centerline as references. The accuracy of the calibration was approximately 0.3 degrees.

<u>Refraction Amplitude Correction Experiment</u> - To provide a dipole noise source, a segment of polished cylinder was mounted transverse to the open jet. The 1.27 cm diameter cylinder, shown schematically in figure 6, was centered vertically on the jet axis. The cylinder was held in place by a larger 2.54 cm diameter, cylinder which extended through the open jet shear layer to an external support stand. The lower end of the test cylinder was held rigid by several guy wires connected to points beneath the open jet. None of the wires crossed the flow field upstream of the cylinder.

A splitter plate was attached to the rear stagnation point of the support cylinder to suppress its vortex shedding mechanism. The guy wire vortex shedding frequency was approximately a factor of 10 higher than the test cylinder frequency. Consequently, the dominant tone in the acoustic spectrum was provided by the test cylinder.

The cylinder directivity pattern outside the flow was measured using the previously described boom arrangement shown in figure 5. The pivot point was aligned with the test cylinder centerline. Microphone m_2 was used to measure the sound pressure level as a function of measurement angle, θ_m. This angle was now referenced directly to m_2 instead of the midpoint between the microphones.

Sound generated at the cylinder ends propagated through the shear layer at almost the same angle as sound generated at the center of the cylinder. This is illustrated in figure 6 with microphone m_2 situated at 90^o to the jet axis. The acoustic ray reaching m_2 from the lower end of the cylinder propagates through the shear layer at 12.5 degrees relative to the local normal.

Discrete Tone Turbulence Scattering Experiment - An acoustic source, consisting of a speaker with a 9 cm diameter exponential horn, was located on one side of the open jet (fig. 7). Discrete tone sound waves were transmitted through both open jet turbulent shear layers to an array of five microphones orientated at grazing incidence on the opposite side of the airstream. The transmitted tone sound pressure level and spectrum shape were monitored as a function of increasing tunnel Mach number at various axial stations, X. The speaker and microphone array formed a horizontal plane which contained the open jet axis. The speaker centerline formed a 90^o angle with the jet axis. The microphone separation distance, ℓ, measured relative to m_o in figure 7, was determined by the jet Mach number. This will be discussed later.

Instrumentation

The various speakers were powered by a 150 watt single channel amplifier. A sine wave generator provided the amplifier input signal. The generator frequency was held to within 2 Hz of each source frequency evaluated in the test program.

Far field acoustic sound pressure levels were measured with commerically available 0.635 cm diameter condenser microphones at grazing incidence. Since microphone m_2 penetrated the shear layer in certain test configurations, protective grids were used at all times. Admittedly, the microphone frequency response was not flat due to the protective grid, but, comparisons of absolute sound pressure level measurements at different frequencies were not needed in the present investigation. For example, the angle correction experiment measured the acoustic wavefront propagation angle which is independent of the radiated sound pressure level. The amplitude correction experiment used only the normalized acoustic source directivity pattern at each frequency. Finally, the scattering experiment monitored the change in acoustic sound pressure level for a fixed discrete tone as the open jet Mach number increased. Absolute sound pressure level comparisons between different frequencies were, therefore, not needed. Based on the above arguments atmospheric attenuation was not relevant to the present study. All microphones were calibrated daily with a 250 Hz pistonphone.

Microphone signals and the sine wave generator signal were recorded on magnetic tape during certain portions of the test. The frequency response of the FM tape system was flat over the frequency range investigated here.

Spectrum analysis was conducted with a narrow bandwidth, 500 line, real time spectrum analyzer-ensemble averager. Each spectrum was generated from 256 ensemble averages. The effective noise bandwidth of the analyzer filter influenced the discrete tone scattering results, the consequences of which will be discussed later.

Cross-correlations were performed with a 400 line, real time correlation and probability analyzer. Input signals were not filtered.

Mean velocity measurements of the open jet shear layer were acquired with a 0.025 mm diameter hot film operating in conjunction with a constant temperature anemometer system. The probe was calibrated in the tunnel test section.

Test Program

Refraction Angle Correction Measurements - Measurements were performed at various acoustic source locations, open jet Mach numbers, and source frequencies to assess these parameters in the refraction angle correction theory. Two coordinates defined the source location: the axial station, X, and the source-to-open jet-lip line separation distance, h. Both coordinates are shown in figure 5. Table I lists the test conditions evaluated in the present study with the source position coordinate normalized by the open jet radius. Included in the table is the ratio, h/r, which defines the far-field microphone position relative to the source-to-lip line distance. This parameter is an input to the experimental and theoretical angle and amplitude correction calculations. The lip line also defines the location of the zero thickness shear layer used in the refraction theory described in the section titled "Theoretical Formulation of the Refraction Problem". Therefore, h is at times referred to as the source-to-shear layer separation distance. It should be noted that since the source-to-microphone distance, r, was fixed, changes in h resulted in both h/R_o and h/r changing.

With the acoustic source situated at $X/R_o = 1.33$ and $h/R_o = 1$, the measurement angle, θ_m, was varied from 22.5° to 105° in 7.5° increments. Angles less than 22.5° were not investigated since microphone m_2 in figure 5 would then penetrate the open jet shear layer. On the other hand, angles greater than 105° were not investigated since an adequate separation distance between m_1 and the upstream anechoic chamber wall must be maintained. Line-of-sight interference by the tunnel inlet between the source and microphone m does not occur until θ_m exceeds 136°. Moving the source to $X/R_o = 2.66$ and 4.0 permitted increasing the upstream measurement angle to 127.5°. However, downstream measurement angles less than 30° could not be attained due to shear layer spreading.

The same measurement angle range was used for the off-centerline source positions listed in Table I. For h/r = 0.36, measurement angles less than 30° could not be investigated since m_2 penetrated the flow. As in the on-centerline test geometries, line-of-sight interference was not a problem.

Refraction Amplitude Correction Measurements - The far-field directivity pattern of a dipole source was measured at two source locations and two open jet Mach numbers to assess these parameters in the refraction amplitude correction theory. Changing the Mach number also permitted evaluating the acoustic source frequency dependence. The test geometry, listed in Table II, coincided with two of the test configurations used in the angle correction experiments. Identical conditions were needed since the angle correction must be applied to the dipole directivity before the amplitude correction can be isolated. The dipole directivity was measured at a minimum of twelve angles over the range $\theta_m = 25^o$ to 110^o.

Note that the off-center source location corresponding to Test Configuration 7 in Table II represents a source displacement towards the observer. This displacement direction was selected based on the calculated amplitude corrections obtained from the theoretical analysis to be discussed later. It was determined that the amplitude correction is the largest as the source approaches the shear layer closest to the observer. This was expected to facilitate the experimental assessment of the amplitude correction.

Discrete Tone Turbulence Scattering Measurements - Discrete tone scattering effects due to shear layer turbulence were evaluated at the Mach numbers investigated in the angle correction experiment. The tone frequencies corresponded to f = 1, 2.5, 5, 10, 17.5, and 25 kHz. The importance of changes in turbulence length scale was also investigated by locating the source at three axial stations given by X/R_o = 1.33, 2.66 and 4.0

DEFINITION OF THE OPEN JET SHEAR LAYER

The objective of the mean velocity measurements described here was to document the shear layer characteristics of the UTRC Acoustic Tunnel as a function of axial position and Mach number. These measurements were obtained using hot wire anemometry. Radial distributions of the mean velocity will be presented first to illustrate how the shear layer features change with axial distance. Using these results, the shear layer growth rate will be presented as a function of axial location. Finally, to isolate changes in the velocity distribution with axial location, the velocity profiles are plotted in a dimensionless form using a similarity parameter based on the shear layer growth rate. The resulting curves from various axial stations collapse onto one curve indicating the profiles are similar. This similarity, which has been well substantiated by other investigators, permits comparisons of the UTRC open jet test facility with other facilities.

Mean Velocities

Mean velocity measurements were obtained at an azimuthal position corresponding to the position of one of the tabs on the tunnel inlet nozzle. Figure 8 shows the radial distribution of the mean axial velocity at various stations downstream of the nozzle exit. Here, the local velocity, U, is normalized by the open jet velocity, U_o, while the axial position, X, and radial position, R, are normalized by the jet radius, R_o. The four Mach numbers, M = 0.1, .2, .3 and .4, in each plot, correspond to the test conditions used in the refraction and scattering studies.

The potential core and mixing zone are clearly identified. The distributions exhibit a familiar behavior with the velocity profiles spreading radially with increasing axial distance. The bulge in the velocity profiles at $X/R_o = 0.66$ and 1.33 was due to the severe mixing forced by the tabs attached to the open jet nozzle. This feature is smoothed out with increasing distance from the nozzle exit disappearing altogether beyond $X/R_o = 1.33$. A comparison of the curves at a fixed value of X/R_o indicates that the normalized velocity profiles are independent of Mach number at each axial station.

Shear Layer Characteristics

Figure 9 shows a schematic representation of the coordinates needed to describe the shear layer characteristics. Since there is no universally accepted definition of shear layer boundaries, the inner and outer edges of the shear layer are defined here by the 90 percent ($U/U_o = 0.9$) and 10 percent ($U/U_o = 0.1$) velocity lines, respectively. The distance from the jet centerline to the half-velocity line (U/U_o = 0.5) is denoted by $R_{1/2}$. The local shear layer thickness, δ, is defined as the difference between the inner and outer edges of the open jet.

The average radial position of the inner and outer edge of the shear layer was determined from the velocity profiles in figure 8. The result is shown in figure 10 in addition to the average half-velocity position. The shear layer thickness was then calculated as a function of axial position using these average characteristics. This result is shown as open circles in figure 11 in addition to an empirical straight line fitted through the data points downstream of X/R_o = 1.33. The straight line could not be extended upstream since it would predict a shear layer thickness which exceeds the value measured at X/R_o = 0.66.

Also shown in figure 10 is the well-known analytical solution by Goertler (see page 96, ref. 18) describing the growth of the shear layer in a two-dimensional plane jet. The analytical solution was used to calculate the inner and outer edges of the shear layer based on the 90 percent and 10 percent velocity lines. The Goertler solution is adequate for determining the growth rate of axisymmetric jets. This is evident in the good agreement between theory and the measured open jet shear layer thickness (see figure 11) reported by Candel, et al. (ref. 19). Note that tabs were not necessary in the facility described in reference 19.

Several conclusions can now be drawn regarding the UTRC open jet. First, the shear layer thickness close to the nozzle exit is large when compared to other facilities. This is due to the early mixing forced by the tabs attached to the nozzle exit. Second, the shear layer thickness grows at a slower rate when compared to the standard jet without tabs. At large X/R_o, shear layer thickness approaches the Goertler solution. Despite the alteration of the UTRC shear layer by the tabs, the acoustic refraction and scattering measurements showed good agreement with studies conducted in other facilities. This will be discussed later.

Similarity of Velocity Profiles

To permit direct comparison of the open jet velocity profiles at various axial stations, the mean velocity distributions in figure 8 were plotted versus the similarity parameter, η. Here η is defined as, $\eta = (R - R_{1/2})/\delta$. A comparison of the normalized velocity profiles is given in figure 12 for three different axial stations at Mach number, M = 0.4. The various curves at the three stations collapse onto a single curve. Also shown is the standard hyperbolic tangent analytic curve used for two-dimensional plane-jet shear layers. The good agreement between experimental data and the hyperbolic tangent curve means this relationship adequately describes the UTRC shear layer characteristics. This relation can therefore be used by other investigators in comparing their shear layer properties with those of the UTRC Acoustic Tunnel.

THEORETICAL FORMULATION OF THE REFRACTION PROBLEM

Review

The basic approach for most of the present shear layer correction theories was initially given by Amiet (ref. 6). This analysis treated the case of a source beneath a plane zero-thickness shear layer. The observer was assumed to be in the geometric and acoustic far field of the source. However, the shear layer could be at any distance from the source, which needed be neither acoustically compact nor a point source. This analysis, based on the previous work of Ribner (ref. 1) and Miles (ref. 2), requires that the measurements made outside the shear layer be corrected in both angle and amplitude. The result is a correction method which is independent of frequency and source type (i.e., monopole, dipole, quadrupole).

The same techniques were applied by Jacques (ref. 7) to the case of a source on the centerline of a cylindrical shear layer. This case, although quite similar in principle, does require additional assumptions. In particular, it must be assumed that there are no multiple reflections within the shear layer; that is, the waves reflected from the shear layer are assumed to be completely damped before again reaching the shear layer. Also, the shear layer must be in the acoustic far field of the source; if the shear layer were not in the acoustic far field, then as shown by Amiet (ref. 9), the shear layer correction would depend on source type and frequency. That is, the solution of Amiet is not valid at low frequency where the wavelength of sound is comparable to the jet diameter. For open jet diameters encountered in practice, this is not usually a severe limitation. The cutoff frequency (frequency below which the surrounding chamber becomes non-anechoic) of open jet acoustic test facilities typically correspond to a wavelength to diameter ratio on the order of 1.

The high frequency case of a source on the centerline of a cylindrical shear layer with a thickness significantly greater than a wavelength was treated by Tester and Morfey (ref. 8). Although not explicitly derived as a correction for open-jet wind tunnel measurements, the results of the analysis can be applied toward this end.

It is interesting to note that the shear layer corrections for the two cases of zero thickness and infinite thickness shear layers differ by only a few hundredths of a decible over most of the angular range as shown in reference 9. This would be expected since the basic difference between the two corrections is that the zero thickness case assumes a reflected wave exists while the infinite thickness case assumes that all the energy is transmitted. Since the amplitude of the reflected wave is small over most of the angular range (see e.g., reference 6) and since the reflected energy is proportional to the square of the amplitude, one should expect little difference between the corrections. At the extreme angles where the reflected wave can have a significant magnitude, both the zero thickness and the infinite thickness corrections should be used with caution since neither correction accounts for multiple reflections within the shear layer. Thus, the correction procedure for an infinite thickness shear layer used by Ahuja et al (ref. 14) has the same angle correction as that of Amiet (ref. 6 and 9) and Jacques (ref. 7) and an amplitude correction differing by a few hundredths of a dB over most of the angular range. It is, for all practical purposes, equivalent to the correction procedure for a zero thickness shear layer. A more detailed comparison between the various zero thickness, infinite thickness, plane shear layer and cylindrical shear layer results is given in reference 9.

Shear Layer Correction for An Off-Axis Acoustic Source

For the case of a source on the centerline of a cylindrical shear layer, as was discussed in reference 9, the shear layer must be in the acoustic far field of the source for the shear layer correction to be independent of source type and frequency. Thus, ray acoustics principles are applicable and the shear layer correction can be derived by ray tracing arguments. For the case of a source off the centerline, the derivation will also be based on ray acoustics. The same far-field assumption required for the on-axis source solution applies here. The main difference between this case and the on-centerline case is that the algebra for the ray tracing of the off-center case becomes significantly more complex. The basic principles governing the crossing of the shear layer by a ray remain the same, however.

Figures 13 and 14 show the basic geometry and the coordinate system used in the derivation. The zero thickness cylindrical shear layer has a radius, a, and the source is located off the centerline by a distance a-h. A Cartesian coordinate system has the origin located at the source, S, the x axis parallel to the tunnel axis and the z axis along the normal from the tunnel centerline to the source. A ray travels from the source along the path labeled r_1 crossing the shear layer at point x_1, y_1', z_1', and continues along path r_2 to the observer O at x_2, y_2', z_2'. The plane tangent to the shear layer at point x_1, y_1', z_1' makes an angle α with the x-y' plane. Angles θ_c and ϕ_c describe the ray path beneath the shear layer, θ_t and ϕ_t describe the ray path above the shear layer and θ_m and ϕ_m describe the observer position relative to the source.

The angle θ is the angle between a given line and the x axis or a line parallel to the x axis. Thus θ_c is the angle between the ray beneath the shear layer and the x axis, θ_t is the angle between the transmitted ray and a line parallel to the x axis at the shear layer crossing point, and θ_m is the angle between the x axis and the line joining source and observer. The angle ϕ is the angle between the x-y plane and a plane containing a given line and parallel to the x axis. Thus, ϕ_c is the angle between the x-y plane and the plane defined by the x axis and the ray beneath the shear layer, ϕ_t is the angle between the x-y plane and the plane containing the transmitted ray and parallel to the x axis, and ϕ_m is the angle between the x-y plane and the plane containing the x axis and the observer point. The unprimed coordinate system is defined by rotating the x, y', z' coordinate system through an angle α about the x axis so that z is normal to the tangent plane.

The detailed derivation of the off-axis source correction is given in Appendix A. Results of this calculation can be summarized as follows: the amplitude correction is different from the on-axis case for all source-observer positions. In the special case of an observer located in the plane containing the source and open-jet centerline, the angle correction is identical to that obtained for an on-axis source or for the case of a plane shear layer.

EXPERIMENTAL ASSESSMENT OF REFRACTION THEORY

Angle Correction

Experimental Approach - The primary objective of the experimental program was to measure the angle change associated with acoustic wave-front propagation through an open jet shear layer. While various combinations of source-observer locations could be evaluated the present study was limited to acoustic source and far-field microphone positions situated in a plane which coincided with the jet axis. Under this conditions, angles $\phi_c = 90^o$ and $\alpha = 0^o$ in figures 13 and 14. The resulting propagation path, SBO in figure 14, was thus confined to a plane normal to the tangent plane at the shear layer crossing point.

The three-dimensional geometry in figures 13 and 14 can therefore be replaced by the two-dimensional geometry in figure 15. Here wave fronts propagating in the direction, θ_c, inside the airstream propagate in the direction, θ_t, outside the open jet. The actual path of an acoustic ray is described by the points SBO. The change from θ_c to θ_t is a result of refraction by the shear layer. Without flow the sound propagates at angle θ_m.

The experimental refraction angle correction for the geometry in figure 15 was obtained using the test set-up shown in figure 5. Acoustic ray angle changes were determined from measurements of the constant phase or wave-front surfaces outside the airstream. In this region, the acoustic ray is perpendicular to the wave-front. Once the wave-front angle at the observer location is known, the ray normal to the wave-front ray can be traced back to the point, X_o, at which the sound emerged from the shear layer. The original propagation angle inside the open jet is then obtained from the relationship $\theta_c = \arctan (h/X_o)$.

The wave-front angle was measured in the following manner. Sound was generated at discrete frequencies by an acoustic source inside the open jet. The phase difference, between the signals arriving at microphones m_1 and m_2 in figure 5, was then determined by cross-correlating the signals. From this, the wave-front angle relative to the microphone array was calculated permitting the wavenormal ray to be traced back to the shear layer crossing the point.

Measured Phase Difference and Calculated Angle Change - It now remains to derive the equations linking the measured phase difference and the original propagation angle, θ_c, inside the free jet. The modeling problem is shown in figure 16. For $M = 0$, the angle between the wave front arriving at m_2 and the line connecting the array is denoted by μ_o. This parameter accounts for small differences in the distance, Δr, between the source and the individual microphones. This difference is due to inaccuracies in placing the two microphones at exactly the same radial distance from the source. Typically, the difference was less than 0.25 cm. Assuming this value of Δr yields a maximum value of $\mu_o = 0.016$ radians for the smallest separation distance, ℓ, shown in figure 16.

If the microphone array skewness were neglected, errors would arise in the phase shift measurement. For example, if $\Delta r = 0.25$ cm, then at 10 kHz a 0.07 cycle phase shift occurs between m_1 and m_2. Since the present experiment required an accuracy of 0.02 cycles it was necessary to account for the skewed microphone alignment. That is, the measured phase shift at $M = 0$ was subtracted from the phase shift obtained at finite Mach number. This effectively calibrated the measurement of phase shift to account for microphone placement error. The mathematical details are presented below.

The phase difference (expressed in cycles) between constant phase points arriving at m_1 and m_2 is given by the relation

$$\Delta_T = \Delta + (\Delta_1 - \Delta_2) \tag{1}$$

$$\Delta = \frac{f\ell}{c_0} \sin \mu_0 \tag{2}$$

The parameters, Δ_1 and Δ_2, account for the phase lag between the acoustic input signal to each microphone diaphragm and the final voltage signal applied at the correlator. Nominally, this phase lag is less than 0.1 cycles for the frequency range employed in the present angle correction experiment. The microphone cartridge phase lag characteristics are included in this parameter.

The parameter, Δ_T, was measured directly by cross-correlating the periodic signals arriving at the adjacent microphones. Figure 17 illustrates the correlator time delay trace. Based on the phase shift of the first maximum, $\Delta_T = \tau \cdot f$. The magnitude of τ has been exaggerated to make it perceptible in the figure. Nominally, Δ_T is less than 0.1 cycles. The location of the first maximum in the correlation function was defined as the mid-point between the zero cross-over points. In figure 17 the mid-point of the second cycle and a knowledge of the period were used to locate the mid-point of the first cycle. By using two cross-over points irregularities in the correlation function were averaged. The term "irregularities" is used here to describe a deviation of the measured correlation functions from a smooth sinusoidal behavior. These deviations occurred because both microphones sensed open jet shear layer background noise as well as source noise. Such irregularities in the correlation function only occured, therefore, at non-zero Mach numbers.

For $M \neq 0$, the phase difference, therefore, is given by

$$\Delta'_T = \Delta' + (\Delta_1 - \Delta_2) \tag{3}$$

where

$$\Delta'_T = \frac{f\ell}{c_0} \sin(\mu_0 + \mu_1) \tag{4}$$

Here μ_1 describes the angle between the two wavenormal rays in figure 16. Solving for the difference $\Delta'_T - \Delta_T$ gives

$$\Delta'_T - \Delta_T = \Delta' - \Delta = \frac{f\ell}{c_0}\left[\sin(\mu_0 + \mu_1) - \sin\mu_0\right] \tag{5}$$

Appendix B shows how this expression may be simplified further if μ_o is small. Solving for μ_1 gives

$$\mu_1 = \sin^{-1}\left[\frac{c_0}{f\ell}\,(\Delta'_T - \Delta_T)\right] \tag{6}$$

From this θ_c can be determined using the relationship

$$\theta_c = \tan^{-1}(h/x_0) \tag{7}$$

where

$$x_0 = r\cos\theta_m - (r\sin\theta_m - h)\cot(\mu_1 + \theta_m) \tag{8}$$

The expression for X_o is derived in Appendix C.

The above approach was successful only at M = 0.1. For higher open jet Mach numbers, the facility random background noise dominated the cross-correlation function as is illustrated by the two-microphone correlation function in figure 18. Although a periodic waveform is present in the cross-correlation function, the measured result is not suitable for solving equation 6 for the wavefront propagation angle. To verify that the time delay trace is dominated by facility noise, a second trace is shown with the acoustic source turned off.

The background noise dominated the cross-correlation function despite the 12 dB signal to noise ratio shown in figure 19. This occurred because the microphone input signals to the correlator were not filtered permitting the complete background noise signal to contribute to the cross-correlation. It may appear that this problem can be circumvented by narrowband filtering the microphone spectrum shown in figure 19 to pass only the pure-tone component. However, this still retains in the correlation function a contribution from the cross-correlation of the filtered narrowband microphone signals. The periodicity of this contribution corresponds to the filter cutoff frequencies. Since these frequencies are close to the acoustic source frequency, a portion of the narrowband random contribution would remain in the cross-correlation.

An alternate cross-correlation technique developed by Schlinker (ref. 21) was therefore employed. The method involves cross-correlating the individual microphone signals with the periodic input signal to the acoustic driver system. The random signals due to facility noise are rejected leaving only the periodic component. The success of the method is illustrated by the correlation traces in figure 20. Here $S_{1,s}$ and $S_{2,s}$ represent the individual microphone-signal generator cross-correlation functions. To verify that the traces are independent of the facility noise, one trace is shown with the source turned off.

The mathematical details linking the correlations in figure 20 with the microphone orientation angle $\mu_1 + \mu_o$ are presented in Appendix D. The final result for the phase difference at non-zero Mach number is

$$\Delta'_T = \eta'_1 - \eta'_2 \tag{9}$$

where η' represents the phase difference between the acoustic driver signal and the microphones. Equation (9), when used in conjunction with equation (6), gives

$$\mu_1 = \sin^{-1}\left[\frac{c_o}{f\ell}\left(\eta'_1 - \eta'_2 - \Delta_T\right)\right] \tag{10}$$

A brief discussion of the measured phase difference is now warranted since the angle correction is derived from this parameter. Figure 21 shows the experimentally determined phase difference, $\Delta_T' - \Delta_T$, for a 2.5 kHz acoustic source frequency with the open jet operating at $M = 0.3$. The source position corresponded to Test Configuration 1 in Table I. Two different microphone spacings were used in the measurement. For angles near 90°, where refraction is minimal, a large separation ($\ell = 0.48$ m) was used to obtain a measurable phase shift. In contrast, at angles close to the jet axis where the phase shift is large a smaller separation ($\ell = 0.3$ m) was used.

The measured data in figure 21 are compared to the phase difference calculated from the refraction theory developed in the previous section. The figure shows excellent agreement between the theory and experiment over the complete range of measurement angle. The measured phase was then used to calculate the angle correction associated with the transmission of sound through the shear layer.

Plane Wave Propagation Assumptions - The above experimental approach assumes that the wave front arriving at the far-field microphone array is plane. The possible error in this assumption was evaluated by calculating the time for the sound to travel from the source to the individual far-field microphones. The difference between these times was then compared to the time calculated using the plane wave assumption.

For a point source in a flow, the phase, Θ, of the waves is

$$\Theta = \left\{ t + \frac{1}{c_0 \beta^2} \left[Mx - \sqrt{x^2 + \beta^2 (y^2 + z^2)} \right] \right\} \omega \tag{11}$$

If $\Theta = 0$ at $t = 0$, then the same wave front will reach the point $(X_o, 0, h)$ at time t_o where

$$c_0 \beta^2 t_0 + M X_0 = \sqrt{X_0^2 + \beta^2 h^2} \tag{12}$$

Here X_o is the shear layer crossover in figure 15. Using $\tan \theta_c = h/X_o$ along with equation A.18 relating θ_c and θ_c gives

$$t_0 = \frac{h(1 - M \cos \theta_t)}{c_0 \zeta_t} \tag{13}$$

The time for the wave to travel from X_0 to the observer at 0 (see figure 15) is

$$t_1 = \frac{r \sin \theta_m - h}{c_0 \sin \theta_t} \tag{14}$$

The total time for a sound wave to travel from the source to a far-field microphone is then $t_2 = t_o + t_1$. The exact time difference, Δt_e, for the sound to reach the two separate microphones is obtained from the difference between the value of t_2 calculated for each microphone.

On the other hand, the approximate calculation treating the wave front as plane gives for the time difference (see figure 16).

$$\Delta t_a = \frac{\ell}{c_0} \sin(\theta_t - \theta_m) = \frac{\ell}{c_0} \sin \mu_1 \tag{15}$$

This expression is easily derived from equation (B.5). Note that for this calculation the angles θ_t and θ_m are averages calculated for an observer midway between the two microphones.

Figure 22 shows the percent error between the exact (Δt_e) and approximate (Δt_a) solutions defined as

$$\text{PERCENT ERROR} = 100\,\frac{\Delta t_e - \Delta t_a}{\Delta t_e} \tag{16}$$

The calculations are for the maximum microphone separation used which was $\ell = 0.48$ m. The error goes as the square of the microphone separation so that the next smaller separation value listed in figure 16 would give an error approximately 1/4 as large. Even at the large separation, however, the error was very small, on the order of a few percent. This justifies the experimental approach described earlier.

Comparison of Measured and Theoretical Refraction Angle Correction - Comparison of theory and experiment is given first for the case of an on-axis source location. Shown in figure 23 is a comparison between the measured and theoretical angle correction as a function of open jet Mach number and acoustic source frequency. The source and far field microphone positions correspond to Test Configuration 1. Specific coordinates for this geometry are given in figure 23(a). Only two curves are shown in each plot to avoid crowding the experimental data points.

The agreement between theory and experiment is considered good particularly at frequencies above 1 kHz where the phase differences are large and measurement accuracy is correspondingly good. At 1 kHz, the small measured phase difference introduced some scatter into the experimental data points. To obtain a quantitative assessment of the refraction correction theory, the absolute difference between the theoretical curves and the data can be calculated. Considering the measurement angle, $\theta_m = 37.5^\circ$, where the correction is significant, the average difference was 1.25° at $M = 0.1$, 0.25° at $M = 0.2$, 0.4° at $M = 0.3$, and 0.6° at $M = 0.4$. The largest deviations occurred at low Mach number due to the small measured phase difference.

Figures 24 and 25 show comparisons between the measured and theoretical angle correction at two additional downstream locations. The frequency dependence at $M = 0.4$ is shown in part (a) and (b) of each figure while the Mach number dependence at a fixed frequency of 5 kHz is shown in part (c) of each figure. This limited frequency and Mach number study was conducted to verify the trends obtained in figure 23. In all cases, the agreement between theory and experiment is good. The absolute difference between theory and data points was, in all cases, less than 2° at $\theta_m = 37.5^\circ$.

Considering now off-axis source locations, figure 26 is a comparison between the measured and theoretical angle correction as a function of open-jet Mach number and acoustic source frequency. The test conditions are identical to those evaluated in the on-axis geometry presented in figure 23. This approach permitted assessing the capability of the theory to predict changes in source-to-shear layer separation distances. The results for f = 1 kHz are not included due to the large scatter in the data.

The comparisons in figure 26 indicate good agreement at angles close to the jet axis. However, a consistent discrepancy occurred at large measurement angles for all frequencies and Mach numbers above M = 0.1. At M = 0.1, the discrepancy was not perceptible since the angle correction is smaller.

The origin of the discrepancies was traced to the selection of the source-to-shear layer separation distance, h, which is an input to both the experimental data reduction (see equation 7) and the theoretical analysis. The results in figure 26 (as well as the on-axis comparisons in figures 23, 24, and 25) were obtained using a vortex sheet located at the nozzle lip-line to represent the shear layer. From the mean velocity calibrations shown in figure 10 this vortex sheet was also located close to the half velocity point in the shear layer. The value of h/R_o corresponding to a shear layer located at the nozzle lip-line was 0.55. If, however, the zero thickness shear layer is arbitrarily assumed to be located such that $h/R_o = 0.76$, agreement between theory and experiment improves significantly as shown in figure 27. In figure 27, the theoretical prediction was recalculated using $h'/R_o = 0.76$, in place of $h/R_o = 0.55$. Similarly, the experimental angle corrections were recalculated using $h'/R_o = 0.76$ and equation (7). As shown in figure 27 the agreement between theory and experiment is good at all angles with the difference not exceeding 2° at $\theta_m = 37.5°$ over the complete operating range. Based on the measured mean velocity profiles, the assumption of $h/R_o = 0.76$ implies the zero thickness shear layer is being placed at approximately the quarter velocity point in the shear layer; that is, $U = 1/4\ U_o$ at the assumed vortex sheet location.

This result warrants further discussion since a forced agreement between theory and experiment does not provide assessment of theory. By comparing figure 26 for $h/R_o = 0.55$ and figure 27 for $h/R_o = 0.76$ it can be seen that there is a negligible change in the theoretical angle correction. That is, the theory is not particularly sensitive to small changes in h/R_o. The procedure to reduce experimental data, however, is sensitive to the assumed shear layer location since the ray outside the open-jet is traced back to the shear layer crossover point. As the assumed shear layer location is changed, the crossover point shifts and the experimental result is altered. The better agreement in figure 27, therefore, is due to a change in the experimental result. This indicates that the present experiment and data reduction procedure are poorly designed for assessing theory at small h/R_o.

To support this conclusion, the sensitivity of experimental results to a small change in h (Δh) was calculated and found to be significantly greater at small h/R_o (0.55) than large h/R_o (1.44). As discussed subsequently, good agreement between theory and experiment was obtained at the larger value of h/R_o.

Locating a zero thickness shear layer on an extension of the nozzle lip-line for the purpose of reducing experimental data involves two assumptions. First, shear layer thickness is not important and second, the nozzle lip-line represents the appropriate location to place the vortex sheet. If a zero thickness layer is not assumed, however, refraction theory must be applied to trace the ray back through the shear layer as part of the data reduction procedure. This then introduces the problem of employing theory, to some extent, to reduce data which in turn is intended to assess theory. Such a calculation would be of value, however, in establishing a consistency check (closure of the problem). In addition, a detailed error analysis of the experimental procedure to determine its sensitivity to changes in assumed values of h would further clarify the problem.

To further investigate the observed disagreement between theory and experiment for the off-axis case, additional measurements were performed with the source at the same axial location ($X/R_o = 1.33$) but displaced in the opposite direction from the jet centerline ($h/R_o = 1.44$). Here the source and far-field microphone positions correspond to Test Configuration 5. Shown in figure 28 is a comparison between the measured and theoretical angle correction at selected Mach numbers and acoustic source frequencies. The agreement between theory and experiment is observed to be good at all operating conditions.

In summary, data obtained at three on-axis, axial source positions, four source frequencies and several Mach nubmers between 0.1 and 0.4 suggest that the refraction angle correction is independent of shear layer thickness and frequency as predicted previously. Off-axis theory was validated for source position having a large value of h/R_o. Failure to obtain agreement at an off-axis position having a small value of h/R_o is believed associated with assumptions employed in the reduction of experimental data. Based on work obtained to date, therefore, the refraction angle change correction procedure should be applied as in the present study, that is, the zero thickness shear layer should be located on the nozzle lip-line for all source positions.

Amplitude Correction

Experimental Approach - The primary objective of the present research was to experimentally assess the refraction angle correction theory. A lesser effort was devoted to experimentally evaluating the amplitude correction theory. Tests were conducted using the same two dimensional geometry (fig. 15) employed in the angle correction study. A dipole source consisting of a cylinder undergoing vortex shedding was placed in the open jet airstream. The resulting far field tone directivity was measured at various Mach numbers. Each directivity curve, represented by the function SPL (θ_m, M), was normalized relative to the sound pressure level at $\theta_m = 85^\circ$. Theoretical curves for the dipole directivity inside the open jet were also generated for each test condition. These curves were identified as SPL $(\theta_c(\theta_m),M)$. Here, the angle θ_c inside the airstream was linked to θ_m by the angle correction theory.

Finally, the experimental amplitude correction function, AMP, was determined from the expression

$$\mathrm{AMP}(\theta_m,M)=\mathrm{SPL}(\theta_c(\theta_m),M)-\mathrm{SPL}(\theta_m,M)+C_1(M) \tag{17}$$

The parameter, C_1 was needed to adjust the right side of equation (17) to agree with the absolute value of the amplitude correction.

Ideally C_1 would be determined from a direct measurement of the dipole sound pressure level at one specific angle, θ_m, outside the airstream and the corresponding angle, $\theta_c(\theta_m)$, inside the open jet. However, such measurements exceeded the exploratory nature of the present study. Instead, the experimental amplitude correction function was equated to the theoretical amplitude correction at the 85^o reference angle.

The experimentally determined amplitude correction function was then compared to the theoretical prediction over a range of measurement angles. It should be noted that this approach is only capable of verifying the shape of the amplitude correction theory at each Mach number. Absolute sound pressure levels cannot be ascertained since C_1 was not evaluated by direct measurement.

Comparison of Measured and Theoretical Amplitude Correction Results - The solid curve in figure 29 shows the predicted amplitude correction based on the theoretical formulation of the refraction problem presented earlier. The result applies for an acoustic source situated at the coordinates defined by Test Configuration 6. Satisfactory agreement between theory and experiment exists at measurement angles greater than 55 degrees. The poor agreement at angles close to the jet axis was typical of the results obtained during the present study.

The discrepancy was attributed to the dipole sound source employed in the experiment rather than the theoretical analysis. It is believed that the three-dimensional flow near the ends of the 20 cm long test cylinder (fig. 6) resulted in a spanwise varying vortex shedding process. This condition would not simulate the two-dimensional vortex shedding process for which the dipole directivity was calculated in equation 17.

The above experimental approach was unable to verify directly the theoretical amplitude correction. The theory can, however, be verified indirectly using the theoretical and experimental amplitude correction study recently reported by Ahuja et al. (ref. 14). The theory in reference 14 was assessed for $M \leq 0.26$ with the results confirming the validity of the amplitude correction factor for a source situated on the jet axis. Since the analysis developed in the present study is almost identical (to be discussed below) to the theory in reference 14, the present analysis was indirectly confirmed for a source on the centerline. It still remains to verify the present theory at higher Mach numbers and off-axis acoustic source positions.

Comparisons With Other Investigators

It is worthwhile to clarify the relationship between the present refraction theory and that described in the publication of Ahuja (ref. 14). The angle correction for an on-axis acoustic source reported by Ahuja is exactly that given earlier by Amiet (ref. 6) and Jacques (ref. 7) for a zero thickness shear layer. The general analysis in the section titled Theoretical Formulation of the Refraction Problem reduces to that given in reference 9 for the special case of an on-axis acoustic source.

The general amplitude correction theory in the present study also assumes a zero thickness shear layer. In contrast the on-axis analysis used by Ahuja assumes a shear layer thickness which is infinite compared to the acoustic wavelength. The difference between these two approaches for an on-axis source was given earlier by Amiet (eq. (14) of ref. 9) and is quite small over most of the angular range, as shown in figure 30. At the extreme measurement angles (near the zone of silence and near the upstream axis) where the difference between the two approaches becomes significant, it would be expected that neither result would be accurate since neither approach properly accounts for the multiple reflections which occur in these regions. Thus, in the range of practical use, the approach of Ahuja gives results which differ little from those of Amiet (ref. 6) or the present analysis. Consequently, the experimental confirmation of the theory in reference 14 also confirmed indirectly the present analysis. The advantage of the present analysis is that it can treat the case of an off-axis source.

Evaluation and Summary

Refraction of sound waves passing through an open jet circular shear layer results in significant wave front angle changes at Mach numbers greater than 0.1. Acoustic source directivity patterns are thereby changed and, hence, may alter the conclusions drawn from an experiment. The refraction angle change is independent of the acoustic source frequency and the axial source location.

A theory capable of predicting the circular open jet refraction angle changes for an arbitrary acoustic source type, source position, and far-field observer position was validated experimentally. The lip-line vortex sheet model employed in the theory is, therefore, an adequate representation of the finite thickness shear layer. Axial variations in the mean shear layer properties and divergence of the flow field are not needed in the theoretical formulation. The frequency independence of the analysis was verified. Failure to obtain agreement between theory and experiment for an off-axis source at small source-to-shear layer separation distance is believed to be associated with assumptions in the data reduction procedure.

The theory for the refraction amplitude changes associated with sound transmission through the shear layer could not be verified experimentally. The three-dimensional unstable vortex shedding process from the circular cylinder noise source failed to generate the necessary dipole acoustic source directivity pattern.

TURBULENCE SCATTERING EXPERIMENT

Formulation of the Problem

The objective of the experiment described in this section was to assess the importance of discrete tone frequency scattering and spatial scattering as sound propagates through the open jet turbulent shear layer. The first mechanism extracts energy from the tone and redistributes it in adjacent frequency bands resulting in a broadened spectrum while the second mechanism redirects sound to new angles. Both mechanisms result in a change of the discrete tone directivity pattern.

Measurements obtained during the angle correction experiments indicated that frequency scattering occurred in the UTRC open jet. For example, spectrum broadening was found for the source and microphone location defined by Test Configuration 1 in Table I. Figure 31 shows the result with f = 10 kHz, M = 0.4 and $\theta_m = 90^o$. Here the sound was transmitted through the single shear layer between the source and the far field microphone.

Unfortunately, the experimental configuration used in the angle correction measurements in figure 5 cannot be used to directly assess discrete tone scattering phenomena. Both refraction angle and amplitude changes occur across the shear layer making it difficult to isolate the tone amplitude changes due to scattering. Also, varying the open jet Mach number can change the speaker source strength and directivity pattern inside the airstream. Thus, changes in tone amplitude with Mach number cannot be attributed, necessarily, to turbulence scattering phenomena.

To circumvent these problems an alternative test configuration was chosen. An acoustic source was located on one side of the open jet (figure 7) transmitting a pure tone through both shear layers to an array of microphones on the opposite side of the airstream. In this case, the speaker source strength could be assumed constant with changes in tunnel Mach number. The tests were limited to assessing scattering effects at 90° to the open jet. This technique had previously been employed by Paterson (ref. 20) to investigate turbulence scattering in a small, turbulent round jet.

The first microphone, m_o, was situated on the acoustic source centerline and measured the zero Mach number sound pressure level. The remaining microphones were displaced downstream at a distance ℓ, to account for convection through the open jet. Analytically, the displacement relative to the m_o microphone was given by the simple Mach number dependent expression $\ell = 2R_oM$. Based on the above test configuration, microphone m_o measured the M = 0 acoustic spectrum while m_4 measured the M = 0.4 spectrum. The experimental approach in figure 7 assumes that microphone m_o is situated on the speaker centerline. If this condition is not satisfied, the measured sound pressure level will correspond to the intensity on a side of the lobe of the speaker directivity pattern.

The relative importance of any microphone misalignment with the speaker centerline is determined by the shape of the speaker directivity pattern. This was evaluated by a separate test in which a microphone was traversed on a line parallel to the array in figure 7. The speaker centerline was then identified as the station at which the intensity was a maximum. The changes at locations off the speaker axis were then tabulated after correcting for the increased distance to each microphone location. At 5^o from the speaker centerline, the following changes in the directivity pattern were observed:

Frequency	Change in SPL
5 kHz	1 dB decrease
10 kHz	2 dB decrease
20 kHz	1 dB increase
25 kHz	2 dB increase

The sound pressure level increased or decreased monotonically between the speaker centerline and the 5^o off axis position.

The geometrical technique used to locate m_o in figure 7 was capable of aligning the microphone within 5^o of the acoustic source centerline. Considering the small change in the speaker directivity pattern over this range, it can be concluded that microphone m_o measured the approximate intensity emitted on the speaker centerline.

Placement of the downstream microphones in figure 7 assumes that the open jet can be modeled as a uniform velocity profile bounded by a vortex sheet. In reality, this approach fails to account precisely for the streamwise convection of acoutic wavefronts as they propagate through the finite thickness open jet shear layer. Consequently, the downstream microphones would not be aligned with the acoustic ray emitted on the speaker centerline and emerging at 90^o to the open jet. Instead these microphones would measure the intensity on the side of the lobe of the speaker directivity pattern.

The relative importance of propagation through the shear layer can be estimated by modeling the open jet as a uniform velocity profile bounded by a vortex sheet at the 10 percent velocity line in figure 10. At $X/R_o = 4$ and $M = 0.4$, microphone m_4 in figure 7 would be 7^o off-axis relative to the acoustic ray emitted on the speaker centerline. On the other hand, if the open jet diameter corresponds to the 90 percent velocity line, then m_4 would be 4^o off-axis. In either case the spear directivity pattern is sufficiently broad to ensure that microphone m_4 measures approximately the intensity of sound emitted on the speaker centerline. Thus, modeling the open jet as a uniform velocity profile bounded by the lip line vortex sheet is adequate for locating the downstream microphone positions in figure 7.

Admittedly, the dual shear layer transmission in figure 7 creates more severe frequency and direction scattering than the single shear layer transmission in figure 5. This is verified by the spectrum comparison in figure 31. Consequently the results presented in the following section represent trends rather than direct calibrations for turbulence scattering through a single shear layer in an open jet.

Experimental Results

Figure 32 shows the measured discrete tone spectra as the open jet Mach number and source frequency changed. All spectra (with the exception of those in figure 32(d)) are plotted relative to the tone sound pressure level measured at $M = 0$. This permits monitoring changes in tone amplitude due to both frequency and direction scattering. Normalized sound pressure levels were used in figure 32(d) since the speaker output amplitude drifted with time. The analyzer bandwidth, BW, increased as the acoustic source frequency increased. This was a limitation of the analyzer employed in the study. Standard correction for analyzer bandwidth could not be made since each spectrum contained both pure tone and narrowband random noise. Methods exist for estimating the correction, but such detailed information exceeded the exploratory nature of the present experiment.

Several conclusions can now be arrived at based on figure 32. First, tone broadening, at frequencies above 5 kHz, increases as the open jet Mach number increases. Second, tone broadening is accentuated as the source frequency increases. Finally, the tone amplitude decreases as both frequency and Mach number increase.

Few open jet experimental studies of acoustic source scattering effects are available for comparison. Ahuja et al. (ref. 14) have shown that for $\theta_m = 90^o$ and frequencies below 10 kHz, no broadening occurs about the discrete tone peak value. This result, which is limited to $M \leq 0.18$, agrees qualitatively with the observations in the present study for similar test conditions. Ahuja also found that the discrete tone amplitude remained almost constant if $f \leq 10$ kHz and $M \leq 0.18$. Again this agrees qualitatively with the results in figure 32. Although a 2.5 dB decrease occurred in the present investigation at $f = 10$ kHz and $M = 0.2$ this may be due to the dual shear layer transmission approach employed here.

The importance of changes in turbulence length scale was also investigated in the present experiment. This was accomplished by locating the source at three axial stations given by $X/R_o = 1.33$, 2.66 and 4.00. Turbulence length scales are known to scale with the local shear layer thickness. Based on the shear layer growth rate in figure 11 the eddy length scales increased by a factor of 1.7 as the acoustic source moved downstream. Figure 33 shows the resulting increase in frequency scattering and a decrease in absolute tone sound pressure level at $f = 5$ kHz, $M = 0.4$. Similar results were observed at higher frequencies. The measurements demonstrate that turbulence scattering effects are more pronounced at downstream stations.

Based on the above trend, shear layer scattering at stations far downstream must be assessed accurately if source directivity patterns are required for discrete tones. This follows since sound radiating to the far field at angles close to the jet axis is originally transmitted through the shear layer at large X/R_o. Consider, for example, an acoustic source situated on the open jet axis in Test Configuration 1. If $M = 0.4$ and $\theta_m = 22.5^o$ then, based on the angle correction, the shear layer crossing point is given as $X/R_o = 3.2$. Consequently, sound radiating at angles close to the jet axis encounters more severe turbulence scattering than sound radiated at 90° to the open jet.

Ahuja observed that the ratio of shear layer thickness (or eddy size) to acoustic wavelength was not large enough for significant scattering to occur. This statement must be considered in light of the low Mach number ($M \leq 0.18$) and the axial acoustic source location employed in Ahuja's study. The latter parameter was limited to one location given by $X/R_o = 0.44$. Based on the Goertler shear layer thickness theory (fig. 11), which would be expected to describe the open jet shear layer thickness used in reference 14, the eddy length scales at $X/R_o = 0.44$ would be small compared to the present experiment. Consequently, scattering effects would be weaker. However, scattering effects would be more pronounced with changes in axial location in the Ahuja study since the shear layer growth rate is larger. At $X/R_o = 4.0$, both facilities would be expected to demonstrate similar scattering effects.

Although scattering was observed at high frequencies and high Mach numbers in the present study, it was not considered an important phenomenon for the angle correction experiment. This is because the wave front tracking technique employed in the present study is independent of absolute sound pressure level. Admittedly, spatial scattering from points adjacent to the shear layer crossing point, X_o, in figure 15, would contribute to the cross-correlation function. However, the contribution would be random since the eddy size and instantaneous velocity is random. Long time averages would tend to smooth out these contributions leaving only the refraction effects due to the mean flow. Similar arguments can be made for the frequency scattering effects. The refraction amplitude correction experiment was not susceptible to scattering effects since the dipole source frequencies were below 5 kHz.

Summary

Discrete tone broadening and absolute sound pressure level changes are significant at frequencies above 10 kHz and open jet Mach numbers greater than 0.2. These observations apply if the source is within one diameter of the open jet exit. Scattering effects are more pronounced at stations further downstream with scattering phenomena appearing at frequencies below 10 kHz.

The above observations demonstrate that turbulence scattering can be significant in open jet test facilities at Mach numbers approaching M = 0.4. If accurate source directivity patterns are required for discrete tone sources, the scattering mechanism must be considered. Model propeller and rotor noise studies as well as supersonic jet screech noise investigations, therefore, can be adversely affected by turbulence scattering phenomena.

CONCLUSIONS

1. Far-field noise directivity patterns measured in open-jet acoustic test facilities are significantly altered at test Mach numbers of 0.1 and greater due to sound wave refraction by the open-jet shear layer. This is evident from measurements of the wavefront angle change associated with sound propagation through the shear layer.

2. For on-axis source locations, the refraction angle change for a circular cross-section open jet was well predicted by the zero thickness shear layer theory of Amiet over the Mach number range of 0.1 to 0.4 employed in the present experiment.

3. For the range of shear layer thicknesses considered in the present experiment, the refraction angle change was independent of shear layer thickness. This is evident from wavefront angle change measurements conducted at axial source positions between 0.3 and 2 diameters downstream of the nozzle exit. This independence of thickness and shear layer divergence confirms a previous theoretical prediction.

4. The refraction angle change was independent of frequency over the 1 kHz to 10 kHz range considered in the present experiment. This independence confirms a previous theoretical prediction.

5. The off-axis source, refraction angle theory developed in the present program was confirmed experimentally for the case in which observer and source were located in a plane passing through the open-jet axis and the source-to-shear layer distance was greater than one open jet radius.

6. Measurable differences between theory and experiment for the refraction angle change occurred with an off-axis source at a source-to-shear layer separation distance less than one jet radius. This disagreement, at present, is not viewed as a failure of the theoretical angle correction. Rather, it is believed due to the sensitivity of the experimental method to small changes in the assumed zero thickness shear layer position at small source-to-shear layer separation distance.

7. Theory for the refraction amplitude change associated with sound transmission through a shear layer could not be verified due to limitations of the experimental technique. Comparison of predicted refraction amplitude changes with previously published measurements provides a partial validation of theory for small Mach number and on-axis source locations.

8. Scattering of sound by shear layer turbulence is significant at Mach numbers greater than 0.2 and frequencies greater than 5 kHz. Scattering effects increase as the source position is moved downstream.

United Technologies Research Center
East Hartford, Connecticut 06108

April 15, 1978

APPENDIX A

Derivation of Shear Layer Correction For An Off-Axis Acoustic Source

Figures 13 and 14 show the basic geometry and the coordinate system used in the following derivation. These figures were previously described in the section entitled "Theoretical Formulation of the Refraction Problem."

Refraction Angle Change - The angular change of a ray on passing through the shear layer is determined by treating the waves on either side of the shear layer as plane waves and matching phase across the shear layer. This planar assumption should be valid as long as the wavelength is smaller than the open jet radius.

The small disturbance pressure field produced by an arbitrary source can be written as a Fourier composition of plane waves of the form

$$P_i = e^{-i(\Theta - k_{z1} z)} \tag{A.1}$$

where

$$\Theta \equiv -\omega t + k_x x + k_y y \tag{A.2}$$

and k_y and k_z represent wavevectors in the x, y, z coordinate system. Substitution of equation (A.1) in the wave equation

$$\left(\frac{D^2}{Dt^2} - C_o^2 \nabla^2\right) P = 0 \tag{A.3}$$

$$\frac{D}{Dt} \equiv \frac{\partial}{\partial t} + U \frac{\partial}{\partial x}$$

gives

$$\bar{k}_{z1} = (1 - M\bar{k}_x)^2 - \bar{k}_x^{\,2} - \bar{k}_y^{\,2} \tag{A.4}$$

where the overbar on k indicates normalization by ω/C_o; i.e., $\bar{k} = k\,C_o/\omega$.

The normal to a wavefront is found by taking the gradient of the phase of equation (A.1) giving

$$\hat{n}_e = \frac{\bar{k}_x \hat{i} + \bar{k}_y \hat{j} + \bar{k}_{z1} \hat{k}}{1 - M\bar{k}_x} \tag{A.5}$$

Since the wavefronts produced by a source in a stream are spheres with their center at the retarded source position, this normal vector points from the retarded source position to x_1, y_1', z_1'. The direction of energy propagation (the line connecting the present source position to x_1, y_1', z_1') can be found by adding $\hat{i}$ M to equation (A.5). Thus,

$$\hat{n}_1 = \frac{\hat{n}_e + \hat{i} M}{|\hat{n}_e + \hat{i} M|} = \frac{\hat{i}(M + \beta^2 \bar{k}_x) + \hat{j}\, k_y + \hat{k} \bar{k}_{z1}}{\sqrt{1 + M^2 \left[(1 - M\bar{k}_x)^2 - \bar{k}_x{}^2\right]}} \tag{A.6}$$

The transmitted wave at point x_1, y_1', z_1' can be written

$$P_t = T\, e^{-i(\Theta + k_{z2} z)} \tag{A.7}$$

Substitution in equation (A.3) but with M = 0 gives

$$\bar{k}_{z2}^2 = 1 - \bar{k}_x^2 - \bar{k}_y^2 \tag{A.8}$$

Taking the gradient of the phase of equation (A.7) gives for both the normal to a wavefront above the shear layer and the direction along which energy is propagated

$$\hat{n}_2 = \bar{k}_x \hat{i} + \bar{k}_y \hat{j} + \bar{k}_{z2} \hat{k} \tag{A.9}$$

Equations (A.6) and (A.9) give the relation between the ray paths for the incident and transmitted rays. Rather than have this relation in terms of the parameters k_x and k_y (which must be equal in equations (A.6) and (A.9) in order for the phase of the incident and transmitted waves to be equal across the shear layer) it is more useful to put the relation in terms of the angles θ and ϕ. Then, x_1, y_1 and z_1 can be written as

$$\begin{aligned} x_1 &= r_1 \cos \theta_c \\ y_1 &= r_1 \sin \theta_c \cos \gamma_c \\ z_1 &= r_1 \sin \theta_c \sin \gamma_c \end{aligned} \tag{A.10}$$

with

$$r_1 = \frac{a \sin \alpha}{\cos \phi_c \sin \theta_c} = \frac{a(\sin \gamma_c - g \sin \phi_c)}{\sin \theta_c} \tag{A.11}$$

and

$$\gamma \equiv \phi + \alpha$$

$$g \equiv 1 - h/a$$

The first equality in equation (A.11) can be verified from figure 14, and the second equality is found from equation (A.20), to be derived later. The normal $\hat{n}_1$ along r_1 is then

$$\hat{n}_1 = \hat{i}\cos\theta_c + \hat{j}\sin\theta_c\cos\gamma_c + \hat{k}\sin\theta_c\sin\gamma_c \tag{A.12}$$

Comparisons of equations (A.6) and (A.12) show that

$$\cos\theta_c = \frac{M + \beta^2\bar{k}_x}{\sqrt{1 + M^2\left[(1 - M\bar{k}_x)^2 - \bar{k}_x{}^2\right]}} \tag{A.13a}$$

or

$$\bar{k}_x = \frac{1}{\beta^2}\left[\frac{\cos\theta_c}{\sqrt{1 - M^2\sin^2\theta_c}} - M\right]$$

Also

$$\bar{k}_y = \frac{\sin\theta_c\cos\gamma_c}{\sqrt{1 - M^2\sin^2\theta_c}} \tag{A.13b}$$

$$\bar{k}_{z1} = \frac{\sin\theta_c\sin\gamma_c}{\sqrt{1 - M^2\sin^2\theta_c}} \tag{A.13c}$$

For the transmitted wave the normal $\hat{n}_2$ along r_2 can be written

$$\hat{n}_2 = \hat{i}\cos\theta_t + \hat{j}\sin\theta_t\cos\gamma_t + \hat{k}\sin\theta_t\sin\gamma_t \tag{A.14}$$

Comparison with equation (A.9) gives

$$\bar{k}_x = \cos\theta_t \tag{A.15a}$$

$$\bar{k}_y = \sin\theta_t \cos\gamma_t \tag{A.15b}$$

$$\bar{k}_{z2} = \sin\theta_t \sin\gamma_t \tag{A.15c}$$

By equating the values of $\bar{k}_x$ and $\bar{k}_y$ given by equations (A.13) and (A.15), the incident and transmitted angles are found to be

$$\beta^2 \cos\theta_t = \frac{\cos\theta_c}{\sqrt{1 - M^2 \sin^2\theta_c}} - M \tag{A.16}$$

$$\sin\theta_t \cos\gamma_t = \frac{\sin\theta_c \cos\gamma_c}{\sqrt{1 - M^2 \sin^2\theta_c}} \tag{A.17}$$

Equation (A.16) can also be written

$$\tan\theta_c = \frac{\zeta_t}{\beta^2 \cos\theta_t + M} \tag{A.18}$$

where

$$\zeta_t^2 = (1 - M\cos\theta_t)^2 - \cos^2\theta_t$$

which agrees with equation 1 of reference 6. Other useful relations are

$$\sin\theta_c = \frac{\zeta_t}{\sqrt{1 + M^2 \zeta_t^2}}$$

$$\zeta_t = \frac{\sin\theta_c}{\sqrt{1 - M^2 \sin^2\theta_c}} \tag{A.19}$$

The angle α can be related to ϕ_c by applying the sine rule to triangle SAB in figure 14. Thus,

$$\cos \gamma_c = g \cos \phi_c \tag{A.20}$$

Using equation (A.19), equation (A.17) can be rewritten

$$\frac{1}{\zeta_t} \sin \theta_t \cos \gamma_t = \cos \gamma_c \tag{A.21}$$

The above relations determine completely the angle change needed in the shear layer correction.

Refraction Amplitude Correction - The amplitude correction will now be determined by calculating the ray tube divergence. Consider a ray tube beneath the shear layer formed by varying θ_c and ϕ_c by amounts $d\theta_c$ and $d\phi_c$, respectively. This produces a ray tube with cross-sectional-area at the shear layer

$$dA_1 = r_1^2 \sin \theta_c \, d\theta_c \, d\phi_c \tag{A.22}$$

Above the shear layer the angle variations are

$$d\theta_t = \frac{\partial \theta_t}{\partial \theta_c} d\theta_c \tag{A.23a}$$

$$d\phi_t = \frac{\partial \phi_t}{\partial \theta_c} d\theta_c + \frac{\partial \phi_t}{\partial \phi_c} d\phi_c \tag{A.23b}$$

Note from equation (A.16) that $\partial\theta_t/\partial\phi_c = 0$ since θ_c and ϕ_c are independent variables. Therefore, this term does not appear in equation (A.23a). The partial derivatives can be found from equations (A.16) and (A.21) to be

$$\frac{\partial \theta_t}{\partial \theta_c} = \frac{\zeta_t^3}{\sin \theta_t \sin^2 \theta_c} \tag{A.24}$$

$$\frac{\partial \phi_t}{\partial \phi_c} = \frac{g \zeta_t \sin \phi_c}{\sin \gamma_t \sin \theta_t} - \frac{\partial \alpha}{\partial \phi_c} \tag{A.25a}$$

$$\frac{\partial \alpha}{\partial \phi_c} = g \frac{\sin \phi_c}{\sin \gamma_c} - 1 \tag{A.25b}$$

$$\frac{\partial \phi_t}{\partial \theta_c} = \frac{\cos \gamma_t \cot \theta_t \sin \theta_c - \cos \gamma_c \cos \theta_c}{\sin \gamma_t \sin \theta_t (1 - M^2 \sin^2 \theta_c)^{3/2}} \tag{A.26}$$

In order to find the area which the ray tube intercepts on the tangent plane, note that z_1 will remain constant in equation (A.10) as θ_c and ϕ_c are varied. From equation (A.10)

$$\frac{x_1}{z_1} = \frac{\cot \theta_c}{\sin \gamma_c}$$

$$\frac{y_1}{z_1} = \cot \gamma_c \tag{A.27}$$

Thus,

$$dx_1 = -r_1 \left[\frac{d\theta_c}{\sin \theta_c} + \cos \theta_c \cot \gamma_c \, d\phi_c \right]$$

$$dy_1 = -r_1 \frac{\sin \theta_c}{\sin \gamma_c} d\phi_c \tag{A.28}$$

A variation $d\theta_c$ gives a contribution to dx_1, while a subsequent variation $d\phi_c$ gives both a dx_1 and dy_1 contribution. This indicates that the ray tube area intercepted by the tangent plane is a parallelogram; its area dA_2 is the $d\theta_c$ contribution to dx_1 times the $d\phi_c$ contribution to dy_1, or

$$dA_2 = \frac{r_1^2 d\phi_c d\theta_c}{\sin \gamma_c} = \frac{dA_1}{\sin \gamma_c \sin \theta_c} \tag{A.29}$$

The cross-sectional area dA_3 just above the shear layer is then, by a similar argument

$$dA_3 = dA_2 \sin \gamma_t \sin \theta_t \tag{A.30}$$

Equation (A.30) can also be derived by setting $r_2 = 0$ in equations (A.34) to be derived later.

The rate of ray tube divergence changes on passing through the shear layer, and the ray tube cross-sectional area must now be calculated for a point at an arbitrary distance above the shear layer. The equations for a point x_2, y_2, z_2 are

$$\begin{aligned} x_2 &= x_1 + r_2 \cos \theta_t = r \cos \theta_m \\ y_2 &= y_1 + r_2 \sin \theta_t \cos \gamma_t \\ z_2 &= z_1 + r_2 \sin \theta_t \sin \gamma_t \end{aligned} \tag{A.31}$$

with $r^2 = x_2^2 + y_2^2 + z_2^2$.

By varying first θ_c and then ϕ_c, the point x_2, y_2, z_2 will trace out two sides of an area. By taking the cross product of the vectors defining these two sides and then taking the dot product with the unit vector $\hat{n}_2$ given by equation (A.14), the ray tube cross-sectional area will be determined. In taking the derivatives of equation (A.31), r_2 will be taken as constant, as the variation of r_2 with θ_c and ϕ_c is irrelevant in the final area result. Thus,

$$\begin{aligned} \frac{\partial x_2}{\partial \theta_c} &= \frac{-r_1}{\sin \theta_c} - r_2 \sin \theta_t \frac{\partial \theta_t}{\partial \theta_c} \\ \frac{\partial y_2}{\partial \theta_c} &= r_2 \left(\cos \theta_t \cos \gamma_t \frac{\partial \theta_t}{\partial \theta_c} - \sin \theta_t \sin \gamma_t \frac{\partial \phi_t}{\partial \theta_c} \right) \\ \frac{\partial z_2}{\partial \theta_c} &= r_2 \left(\cos \theta_t \sin \gamma_t \frac{\partial \theta_t}{\partial \theta_c} + \sin \theta_t \cos \gamma_t \frac{\partial \phi_t}{\partial \theta_c} \right) \end{aligned} \tag{A.32}$$

where z_1 is constant and the variation of x_1 and y_1 with θ_c was found using equation (A.28). Also,

$$\frac{\partial x_2}{\partial \phi_c} = -r_1 \cos\theta_c \cot\gamma_c$$

$$\frac{\partial y_2}{\partial \phi_c} = -r_1 \frac{\sin\theta_c}{\sin\gamma_c} - r_2 \sin\theta_t \sin\gamma_t \frac{\partial \phi_t}{\partial \phi_c} \tag{A.33}$$

$$\frac{\partial z_2}{\partial \phi_c} = r_2 \sin\theta_t \cos\gamma_t \frac{\partial \phi_t}{\partial \phi_c}$$

The cross-sectional area dA_4 is then

$$\underline{d\ell_1} = \left(\hat{i}\frac{\partial x_2}{\partial \theta_c} + \hat{j}\frac{\partial y_2}{\partial \theta_c} + \hat{k}\frac{\partial z_2}{\partial \theta_c}\right) d\theta_c \tag{A.34a}$$

$$\underline{d\ell_2} = \left(\hat{i}\frac{\partial x_2}{\partial \phi_c} + \hat{j}\frac{\partial y_2}{\partial \phi_c} + \hat{k}\frac{\partial z_2}{\partial \phi_c}\right) d\phi_c \tag{A.34b}$$

$$dA_4 = \hat{n}_2 \cdot \left(\underline{d\ell_1} \times \underline{d\ell_2}\right) \tag{A.34c}$$

Thus,

$$\frac{dA_4}{dA_3} = \left(1 + \frac{r_2}{r_1}\frac{\sin\theta_c}{\sin\theta_t}\frac{\partial\theta_t}{\partial\theta_c}\right)\left(1 + \frac{r_2}{r_1}\frac{\sin\gamma_c}{\sin\gamma_t}\frac{\sin\theta_t}{\sin\theta_c}\frac{\partial\phi_t}{\partial\phi_c}\right) + \frac{r_2}{r_1}\left(\frac{\sin\theta_c}{\zeta_t}\right)^3\left(\sin\theta_t\frac{\partial\phi_t}{\partial\theta_c}\right)^2 \tag{A.35}$$

Equation (A.35) gives the ray tube divergence behavior above the shear layer. This equation allows one to calculate the sound level just outside the shear layer in terms of the far-field sound.

The incident pressure just inside the shear layer is now needed, and will be calculated from the shear layer transmission coefficient. In crossing the shear layer, the wavefront can be treated locally as being plane. Then the velocity potentials for the incident, reflected and transmitted waves can be written

$$\Phi_i = e^{-i(\Theta + k_{z1} z)}$$

$$\Phi_r = R\, e^{-i(\Theta - k_{z1} z)} \tag{A.36}$$

$$\Phi_t = T_\Phi\, e^{-i(\Theta + k_{z2} z)}$$

where Θ is given by equation (A.2), k_{z_1} by equation (A.4) and k_{z_2} by equation (A.8).

The pressure and fluid displacement will be matched across the shear layer. The pressure is related to the velocity potential by

$$P = -\rho_0 \frac{D\Phi}{Dt} \tag{A.37}$$

Matching the pressure across the shear layer at z_1 gives

$$(1 - M\bar{k}_x)\left[e^{-iz_1 k_{z1}} + Re^{i z_1 k_{z1}}\right] = T_\Phi\, e^{-iz_1 k_{z2}} \tag{A.38}$$

To match the fluid displacement across the shear layer, the interface can be considered to be rippled by the acoustic waves, the ripple moving in the x direction with velocity k_x/U_o. If the observer moves in the x direction with the ripple, the mean flow velocity outside the shear layer will be $-\omega/k_x$ while that inside will be $U_o - \omega/k_x$. Denoting the perturbation z velocity by w and equating flow slopes gives

$$w_t = \frac{w_i + w_r}{1 - M\bar{k}_x} \tag{A.39}$$

Then, using the fact that w = $\partial\Phi/\partial z$ and using equations (A.36), equation (A.38) becomes

$$T_\Phi\, k_{z2}\,(1-M\bar{k}_x)\, e^{-iz_1 k_{z2}} = k_{z1}\left(e^{-iz_1 k_{z1}} - Re^{iz_1 k_{z1}}\right) \qquad \text{(A.40)}$$

Combining equations (A.38) and (A.40),

$$T_\Phi\left[1 + (1-M\bar{k}_x)^2\, k_{z2}/k_{z1}\right] = 2\,(1-M\bar{k}_x)\, e^{iz_1(k_{z2}-k_{z1})} \qquad \text{(A.41)}$$

T_Φ is the transmission coefficient for the potential. The transmission coefficient for pressure is found by noting from equation (A.37) that

$$|T_p| = \left|\frac{P_t}{P_i}\right| = \left|\frac{\Phi_t}{(1-M\bar{k}_x)\Phi_i}\right| = \frac{|T_\Phi|}{1-M\bar{k}_x} \qquad \text{(A.42)}$$

Thus,

$$|T_p| = \frac{2}{1+(1-M\bar{k}_x)^2\, k_{z2}/k_{z1}} \qquad \text{(A.43)}$$

From equations (A.13c), (A.15c), and (A.19)

$$\frac{k_{z2}}{k_{z1}} = \frac{\sin\theta_t \sin\gamma_t}{\zeta_t \sin\gamma_c} \qquad \text{(A.44)}$$

The final result for the amplitude correction can now be given. Equation (A.35) gives the ratio of the square of the pressure just outside the shear layer to that at the observer. Equations (A.43) and (A.44) give the ratio of pressure just outside to the incident pressure just inside the shear layer. Thus, the incident pressure just inside the shear layer can be calculated from that measured at the observer position. By extrapolating this calculated pressure by the factor r_1/r, the corrected pressure at a distance r from the source can be calculated. The final result for the correction factor is then

$$
\begin{aligned}
\left|\frac{P_c}{P_m}\right| = &\left\{\left[\left(\frac{r_1}{r} + \frac{r_2}{r}\,\frac{\zeta_t^3}{\sin^2\theta_t \sin\theta_c}\right)\left(\frac{r_1}{r} + \frac{r_2}{r}\,\frac{\sin\gamma_c}{\sin\gamma_t}\,\frac{\sin\theta_t}{\sin\theta_c}\,\frac{\partial\phi_t}{\partial\phi_c}\right)\right.\right. \\
&\left.\left. + \frac{r_1 r_2}{r^2}\left(\frac{\sin\theta_c}{\zeta_t}\right)^3\left(\sin\theta_t\,\frac{\partial\phi_t}{\partial\theta_c}\right)^2\right]^{1/2} \frac{\sin\theta_c}{\zeta_t^{3/2}}\sqrt{\frac{\sin\theta_t \sin\gamma_t}{\sin\gamma_c\,\partial\phi_t/\partial\theta_c}}\right\} \qquad (A.45) \\
&\left\{\frac{\zeta_t^{3/2}}{2\sin\theta_c}\sqrt{\frac{\sin\gamma_c\,\partial\phi_t/\partial\theta_c}{\sin\theta_t \sin\gamma_t}}\left[1 + (1 - M\cos\theta_t)^2\,\frac{\sin\theta_t \sin\gamma_t}{\zeta_t \sin\gamma_c}\right]\right\}
\end{aligned}
$$

where $\frac{\partial\phi_t}{\partial\phi_c}$ and $\frac{\partial\phi_t}{\partial\theta_c}$ are given by equations (A.25a) and (A.26), respectively.

APPENDIX B

Wavefront Angle Change Calculation

According to equation (5) derived earlier

$$\Delta'_T - \Delta_T = \Delta' - \Delta = \frac{f\ell}{C_0}\left[\sin(\mu_0 + \mu_1) - \sin\mu_0\right] \tag{5}$$

Using the trigonometric identity for the sum of two angles and expanding in a Fourier series gives

$$\Delta'_T - \Delta_T = \frac{f\ell}{C_0}\Big[\left(\mu_0 + \frac{\mu_0^3}{3} + \cdots\right)\cos\mu_1 + \left(1 - \frac{\mu_0^2}{2} + \cdots\right)\sin\mu_1 - \left(\mu_0 + \frac{\mu_0^3}{3} + \cdots\right)\Big] \tag{B.1}$$

Since μ_o was shown to be small ($\mu_o \simeq .016$ radians), higher order terms may be neglected leaving

$$\Delta'_T - \Delta_T = \frac{f\ell}{C_0}\sin\mu_1\left[1 + \frac{\mu_0(\cos\mu_1 - 1)}{\sin\mu_1}\right] \tag{B.2}$$

or

$$\Delta'_T - \Delta_T = \frac{f\ell}{C_0}\sin\mu_1\left[1 - \frac{2\mu_0\sin(\mu_1/2)}{\sin\mu_1}\right] \tag{B.3}$$

The maximum contribution from the second term in equation (B.3) occurs when $\mu_1 = \pi/2$. Then

$$\Delta'_T - \Delta_T = \frac{f\ell}{C_0}\left[1 - \mu_0\right] \tag{B.4}$$

Here μ_o provides a negligible contribution to the phase difference. Hence, an adequate approximation for the phase difference is

$$\Delta'_T - \Delta_T = \frac{f\ell}{C_0}\sin\mu_1 \tag{B.5}$$

This expression is valid to within .016 cycles. Finally,

$$\mu_1 = \sin^{-1}\left[\frac{C_0(\Delta'_T - \Delta_T)}{f\ell}\right] \tag{B.6}$$

APPENDIX C

Shear Layer Angle Correction Calculation

Figure 35 depicts the ray path as the acoustic wave is transmitted through the shear layer. The point, X_o, at which the sound emerges from the airstream is given by

$$X_0 = X_2 - X_3 \qquad (C.1)$$

But

$$X_2 = r \sin(90 - \theta_m) \qquad (C.2)$$

and

$$X_3 = (Y - h) \tan(90 - \theta_m - \mu_l) \qquad (C.3)$$

Thus

$$X_0 = r \sin(90 - \theta_m) + (Y - h) \tan(\mu_l - 90 + \theta_m) \qquad (C.4)$$

or

$$X_0 = r \cos \theta_m - (r \sin \theta_m - h) \cot(\mu_l + \theta_m) \qquad (C.5)$$

Finally the original propagation angle inside the flow is given by the expression

$$\theta_c = \tan^{-1}\left(\frac{h}{X_0}\right) \qquad (C.6)$$

APPENDIX D

Microphone - Acoustic Driver Cross-Correlation Technique

Facility background noise contributed significantly to the two microphone cross-correlation function at Mach numbers greater than 0.1. This effect can be demonstrated analytically. The net pressure, P, sensed by microphone m_2 in figure 35 is

$$P_2(t) = B_2 \cos\left[\omega t - 2\pi(\Lambda + \Delta_2)\right] + P_2'(t) \tag{D.1}$$

Here B_2 represents the frequency dependent discrete tone amplitude while P_2' denotes the facility random background noise. The time dependence is expressed relative to the signal generator which drives the acoustic source in figure 36 The parameter Λ represents the total phase lag between the signal generator output and the microphone input. Here

$$\Lambda = \Delta_a + \Delta_s + \Delta_p \tag{D.2}$$

where Δ_p is the propagation phase delay between the speaker and the microphone. A similar expression exists for the signal at m_1 except that the pure tone is out of phase by Δ' relative to m_2:

$$P_1(t) = B_1 \cos\left[\omega t - 2\pi(\Lambda + \Delta' + \Delta_1)\right] + P_1'(t) \tag{D.3}$$

The resulting cross-correlation function S, is then

$$S_{1,2}(\tau) = \langle P_1(t) P_2(t) \rangle \tag{D.4}$$

or

$$S_{1,2}(\tau) = B_1 B_2 \left\langle \cos\left[\omega t - 2\pi(\Lambda + \Delta' + \Delta_1)\right] \cdot \cos\left[\omega t - 2\pi(\Lambda + \Delta_2)\right] \right\rangle \tag{D.5}$$

The second term in equation (D.5) corresponds to the random noise contribution which dominates the correlation trace in figure 18.

An alternate approach for extracting only the periodic component is to separately cross-correlate each microphone signal with the acoustic driver signal. This technique, described by Schlinker in reference 21, was applied to the measurement of standing waves in a duct using flush mounted wall microphones. The microphones sensed both the acoustic pressure fluctuations and the random turbulent boundary layer pressure fluctuations.

The method is illustrated schematically in figure 35. The output voltage, V_2, from m_2 is cross-correlated with the signal generator voltage, $V_s(t) = V_o \cos\omega t$, resulting in

$$S_{2,s}(\tau) = G_2 V_0 B_2 \left\langle \cos\left[\omega t - 2\pi(\Lambda + \Delta_2)\right] \cos\left[\omega t + \tau\right] \right\rangle \tag{D.6}$$

Note that the microphone system sensitivity, G_2, has been used to link the acoustic pressure and the voltage output. Replacing the trigonometric terms by the complex notation for the cosine function and noting that the time average of the periodic terms is zero gives

$$S_{2,s}(\tau) = \frac{1}{2} G_2 B_2 V_0 \cos\left[\omega t - 2\pi(\Lambda + \Delta_2)\right] \tag{D.7}$$

The measured cross-correlation shown in figure 20 can be represented by a peak voltage amplitude H_2 and a phase between V_s and P_2

$$S_{2,s}(\tau) = H_2 \cos\left[\omega\tau - 2\pi(n_2 + \eta_2)\right] \tag{D.8}$$

where n is an integer.

Comparing like terms in equations (D.7) and (D.8) provides

$$\eta_2 = \Lambda + \Delta_2 - n_2 \qquad 0 \leq \eta_2 \leq 1 \tag{D.9}$$

The value for η_2 is obtained from the microphone - signal generator cross-correlation curve in figure 20. The time delay, τ_2, to the first maximum is used to solve for η_2. Notice that the location of the first maximum was defined as the midpoint between two cross-over points in the correlation function. By using two cross-over points, irregularities in the correlation function trace were averaged.

Figure 20 represents the same operating condition as in figure 18. The background noise which dominated in the first figure has been eliminated from the second figure. To verify that the background noise did not influence the results, the cross-correlation function for microphone m_2 was measured at each test condition with the acoustic source turned off.

Cross-correlating P_1 and V_S, it can be shown that

$$\Delta' = (\eta_1 + n_2) - \Lambda - \Delta_1 , \; 0 \leq \eta_1 \leq \infty \tag{D.10}$$

Here the number of integer cycles phase delay is referenced to m_2. Hence, $\eta_2 - \eta_1$ can exceed one cycle.

Finally,

$$\Delta'_T - \Delta_T = \left[\Delta' + (\Delta_1 - \Delta_2)\right] - \Delta_T \tag{D.11}$$

Substituting equation (D.10) and (D.9) for Δ' and n_2 gives

$$\Delta'_T - \Delta_T = (\eta_1 - \eta_2) - \Delta_T \tag{D.12}$$

REFERENCES

1. Ribner, H. S.: Reflection Transmission and Amplification of Sound by a Moving Medium. J. Acoust. Soc. Amer., vol. 29, 1957, pp. 435-441.

2. Miles, J. W.: On the Reflection of Sound at an Interface of Relative Motion. J. Acoust. Soc. Amer., vol. 29, 1957, pp. 226-228.

3. Gottlieb, P.: Sound Source Near a Velocity Discontinuity. J. Acoust. Soc. Amer., vol. 32, 1960, pp. 1117-1122.

4. Graham, E. W. and Graham, B. B.: Effect of a Shear Layer on Plane Waves of Sound in a Fluid. J. Acoust. Soc. Amer., vol. 46, 1969, pp. 169-175.

5. Amiet, R. K.: Propagation of Sound Through a Two-Dimensional Shear Layer with Application to Measurements in the Acoustic Research Tunnel. United Technologies Research Center Report UAR-L40, 1972.

6. Amiet, R. K.: Correction of Open Jet Wind Tunnel Measurements for Shear Layer Refraction. Progress in Astronautics and Aeronautics, Ed. Martin Summerfield, 1976, pp. 259-280. Also AIAA Paper 75-532, 1975, and UTRC Report N111208-1, 1974.

7. Jacques, J. R.: Noise from Moving Aircraft: Some Relevant Models. Ph.D. Thesis, Cambridge University, 1975.

8. Tester, B. J. and Morfey, C. L.: Developments in Jet Noise Modeling - Theoretical Predictions and Comparisons with Measured Data. J. Sound and Vib., vol. 46, 1976, pp. 79-103.

9. Amiet, R. K.: Refraction of Sound by Shear Layer. AIAA Paper 77-54. Also, to be published in J. Sound and Vib., vol. 58, No. 3., 1978.

10. Candel, S. M.: Application to Geometrical Techniques to Aeroacoustic Problems. AIAA Paper 76-546, 1976.

11. Tester, B. J. and Burrin, R. H.: On Sound Radiation From Sources in Parallel Sheared Jet Flows. AIAA Paper 75-57, 1975.

12. Mani, R., Clapper, W. S., Stringas, E. J. and Banarian, G: Development of a Technique for Inflight Jet Noise Simulation - Part II. AIAA Paper 76-532, 1976.

13. Candell, S. M., Guedel, A, and Julienne, A.: Refraction and Scattering in an Open Wind Tunnel Flow. Proceedings of the 6th International Congress on Instrumentation in Aerospace Simulation Facilities, IEEE, September 1975, pp. 288-299.

REFERENCES (Cont'd)

14. Ahuja, K. K., Tester, B. J., Tanna, H. K., and Searle, N.: Experimental Study of Transmission, Reflection and Scattering of Sound in a Free-Jet Flight Simulation Facility and Comparison with Theory. AIAA Paper 77-1266, 1977.

15. Paterson, R. W., Vogt, P. G., and Foley, W. M.: Design and Development of the United Aircraft Research Laboratories Acoustic Research Tunnel. J. Aircraft, vol. 10, No. 7, 1973, pp. 427-433.

16. Schlinker, R. H., Fink, M. R., and Amiet, R. K.: Vortex Noise from Nonrotating Cylinders and Airfoils. AIAA Paper 76-81, 1976.

17. Paterson, R. W., and Amiet, R. K.: Acoustic Radiation and Surface Pressure Characteristics of an Airfoil Due to Incident Turbulence. AIAA Paper 76-571, 1976.

18. Rajaratnam, N.: Turbulent Jets. American Elsever Publishing Co., 1976.

19. Candel, S. M., Guedel, A., and Julienne, A.: Radiation, Refraction and Scattering of Acoustic Waves in a Free Shear Flow. AIAA Paper 76-544, 1976.

20. Paterson, R. W.: Acoustic Research Tunnel Test Summary #29; Passage of High Frequency Pure Tones Through a Turbulent Round Jet. Report UAR-M112, United Aircraft Research Laboratories, August 1973.

21. Schlinker, R. H.: Transmission of Acoustic Plane-Waves at a Jet Exhaust. AIAA Paper 77-22, 1977.

TABLE I - REFRACTION ANGLE CORRECTION TEST CONDITIONS

Test Geometry Number	Axial Source $\frac{X}{R_o}$	Radial Source $\frac{h}{R_o}$	Microphone Position $\frac{h}{r}$	Open Jet Mach Number M	Source Frequency f, kHz
1	1.33	1	0.25	0.1, 0.2, 0.3, 0.4	1, 2.5, 5, 10
2	2.66	1	.25	.2	5
				.4	1, 2.5, 5, 10
3	4.0	1	.25	.2	5
				.4	1, 2.5, 5, 10
4	1.33	.55	.14	.1, .2, .3, .4	1, 2.5, 5, 10
5	1.33	1.44	.36	.4	5, 10

TABLE II - REFRACTION AMPLITUDE CORRECTION TEST CONDITIONS

Test Geometry Number	Axial Source $\frac{X}{R_o}$	Radial Source $\frac{h}{R_o}$	Microphone Position $\frac{h}{r}$	Open Jet Mach Number M	Vortex Shedding f, kHz
6	1.33	1	0.25	0.22, 0.42	1.1, 2.1
7	1.33	.55	.14	.22, .42	1.1, 2.1

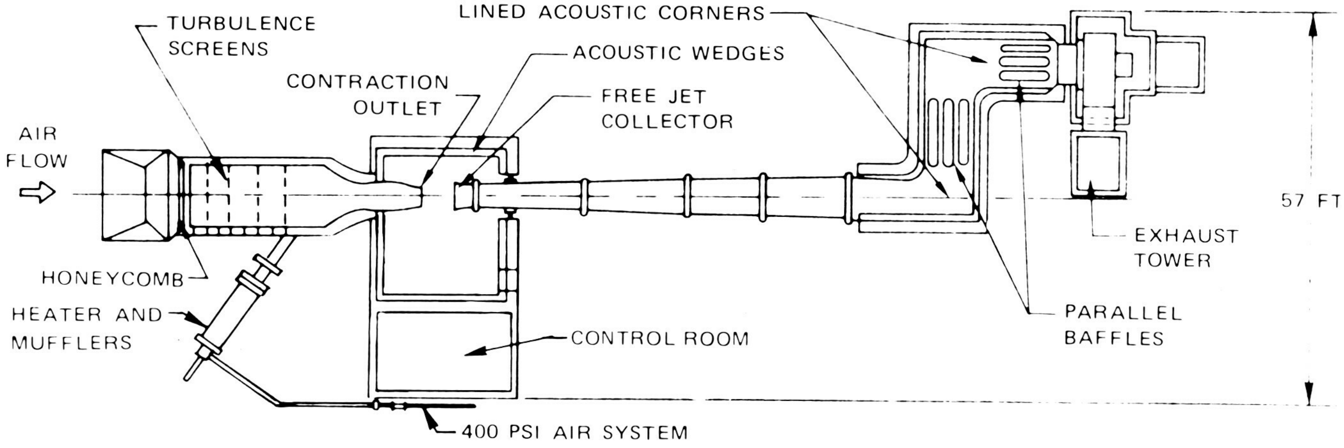

TOP VIEW

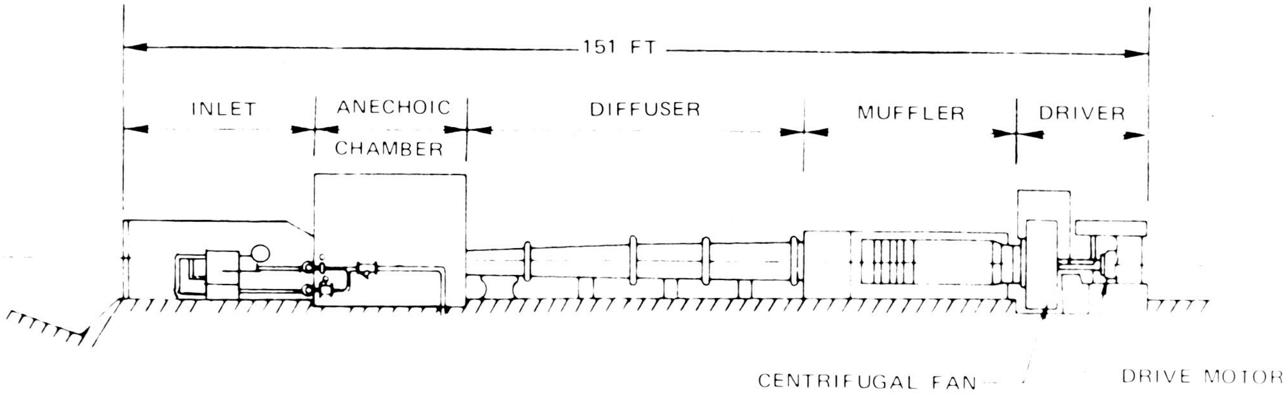

SIDE VIEW

Figure 1 – UTRC Accoustic Research Tunnel

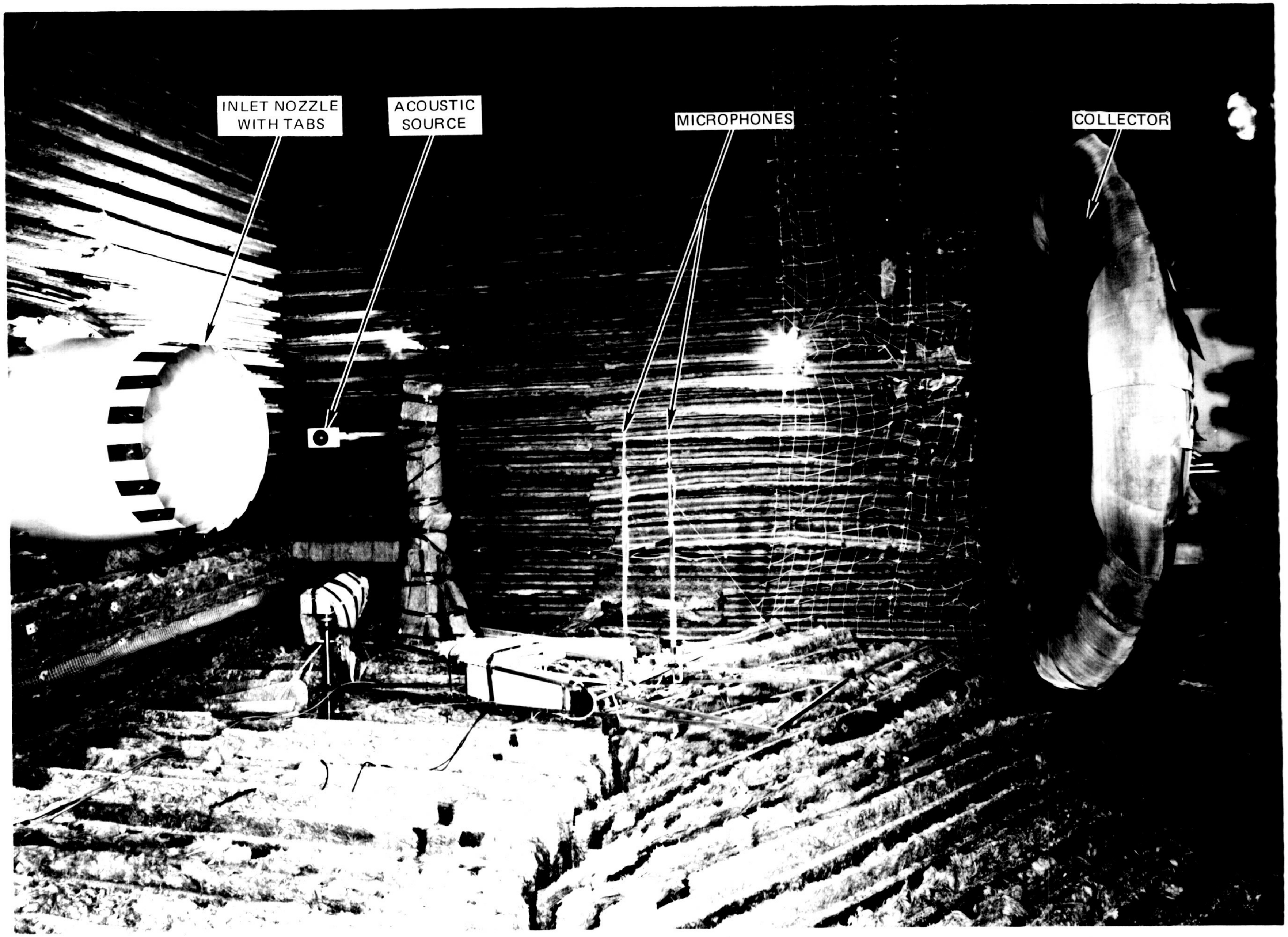

Figure 2 — Anechoic Chamber Test Arrangement for Refraction Angle Correction Experiment

78–04–32 2

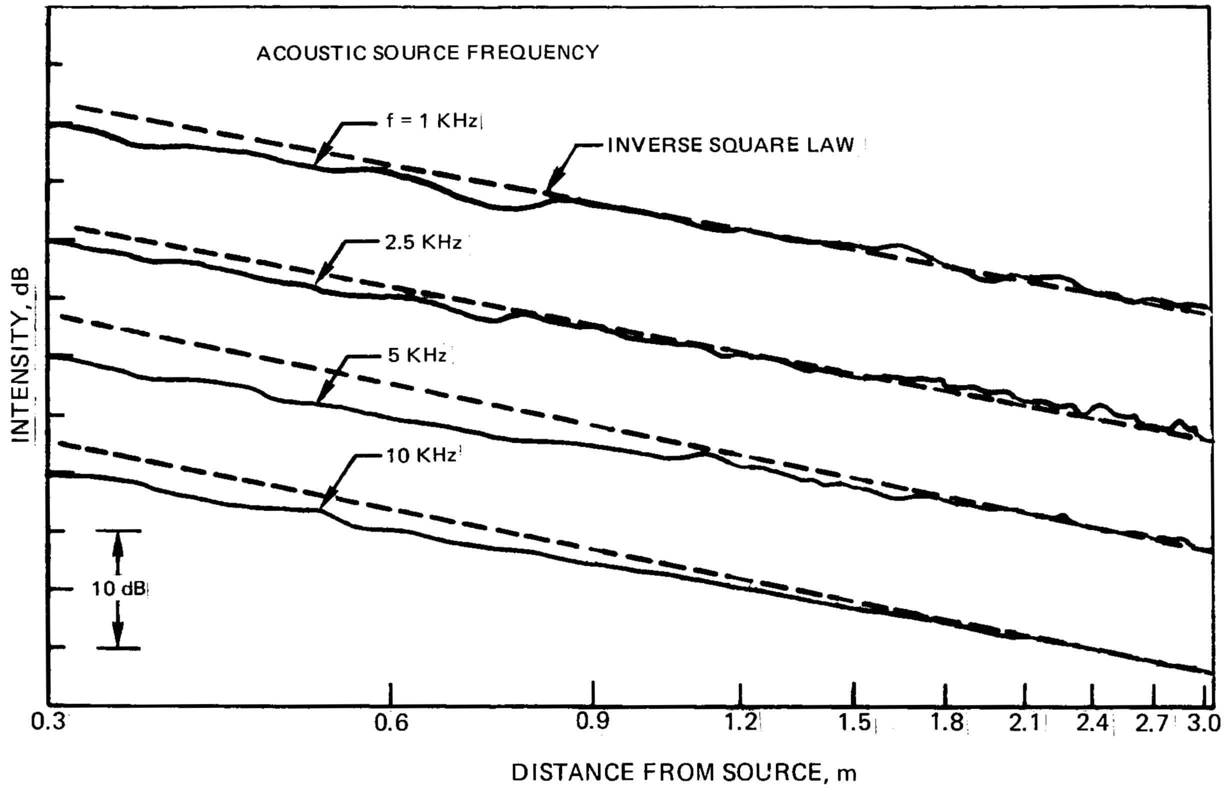

Figure 3—Intensity—Distance Variation for Acoustic Source with Discrete Frequency Excitation

78–04–32–6

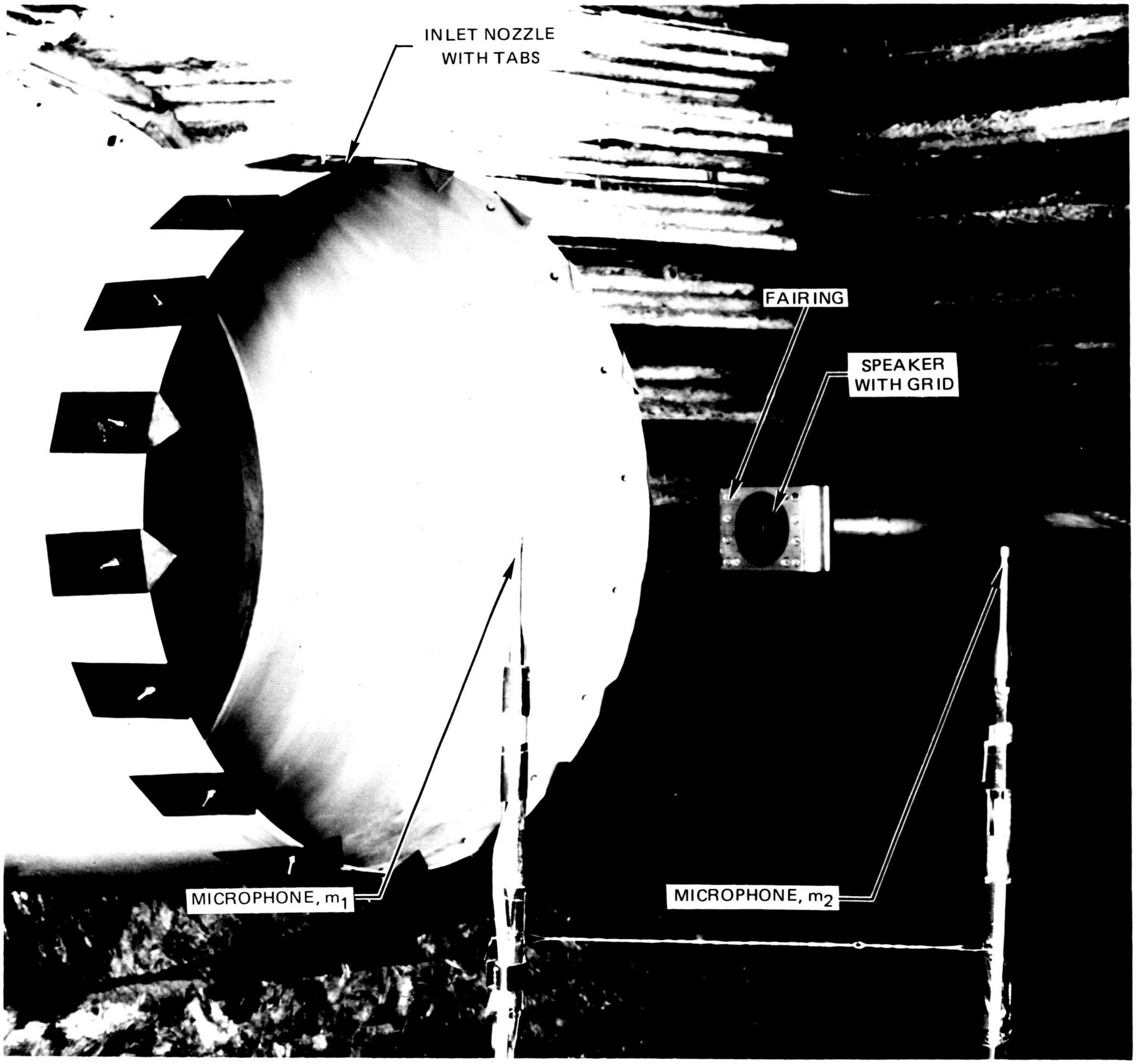

Figure 4—Acoustic Source and Far Field Microphone Arrangement for Refraction Angle Correction Experiment

78–04–32–1

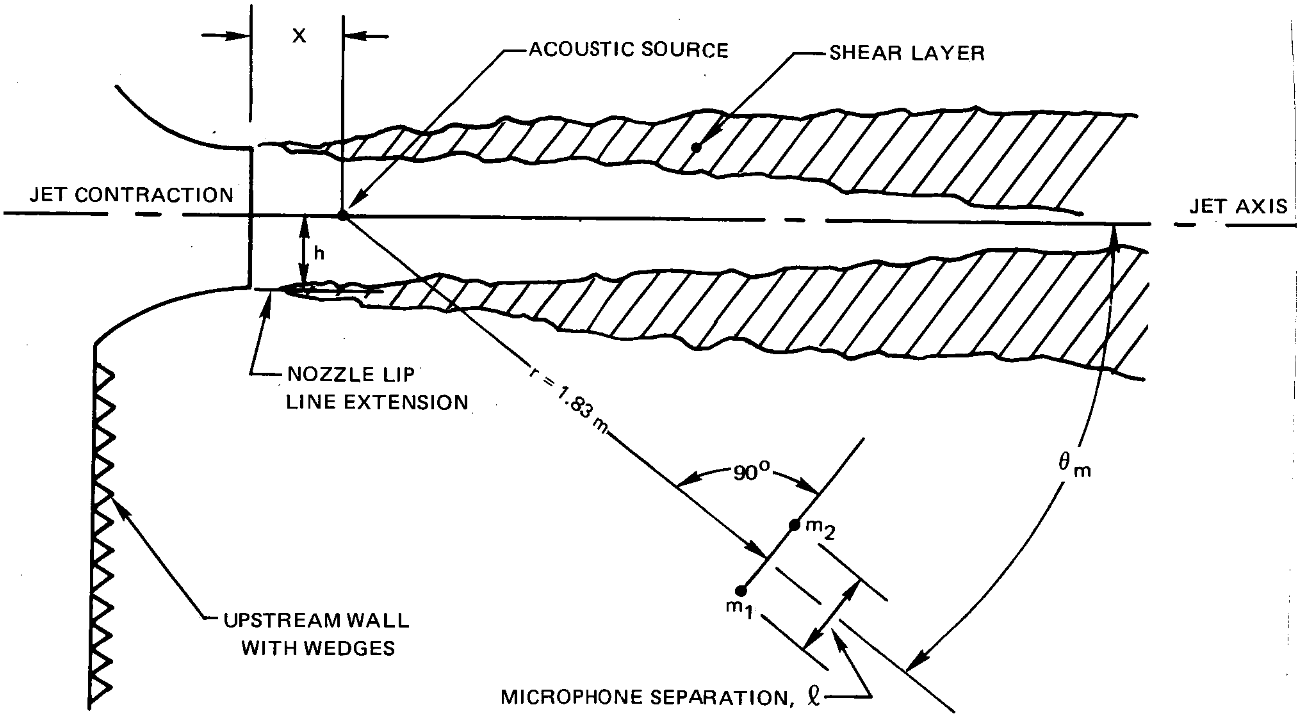

Figure 5—Plan View of Open Jet, Acoustic Source and Far-Field Microphone Arrangement for Refraction Angle Correction Experiment

78—04—32—4

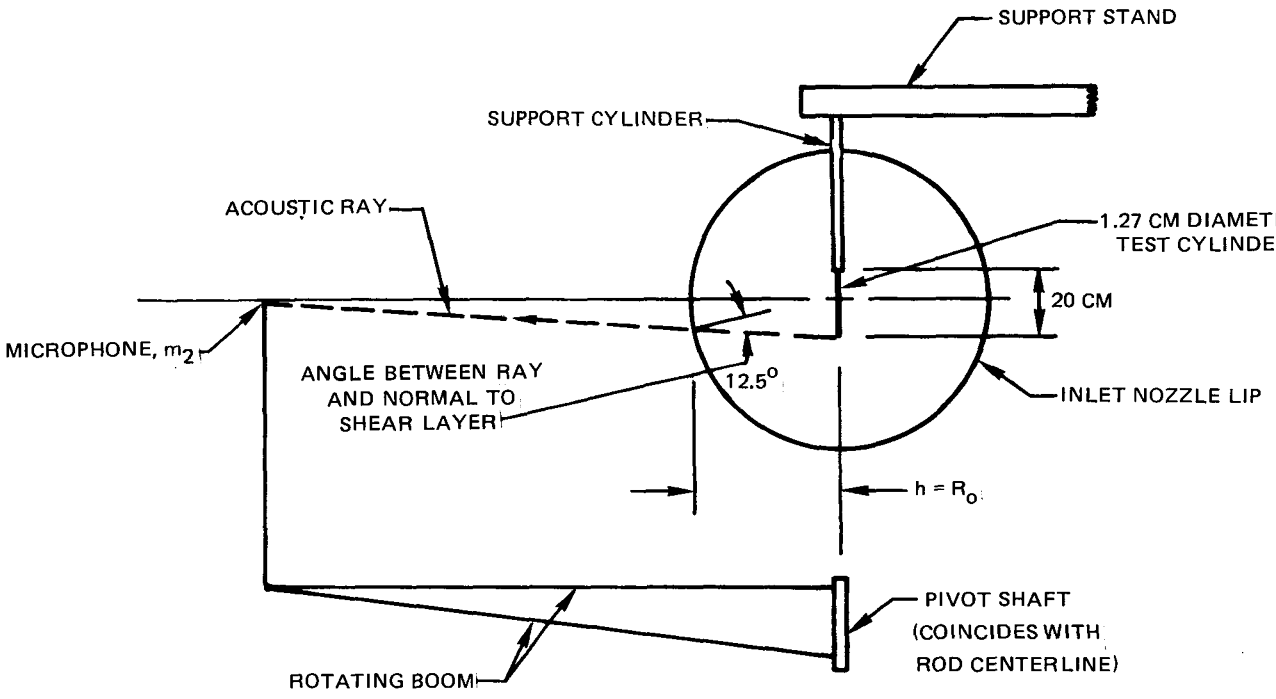

VIEW LOOKING UPSTREAM

Figure 6—Schematic of Dipole Source and Microphone Arrangement for Refraction Amplitude Correction Experiment

78–04–32–5

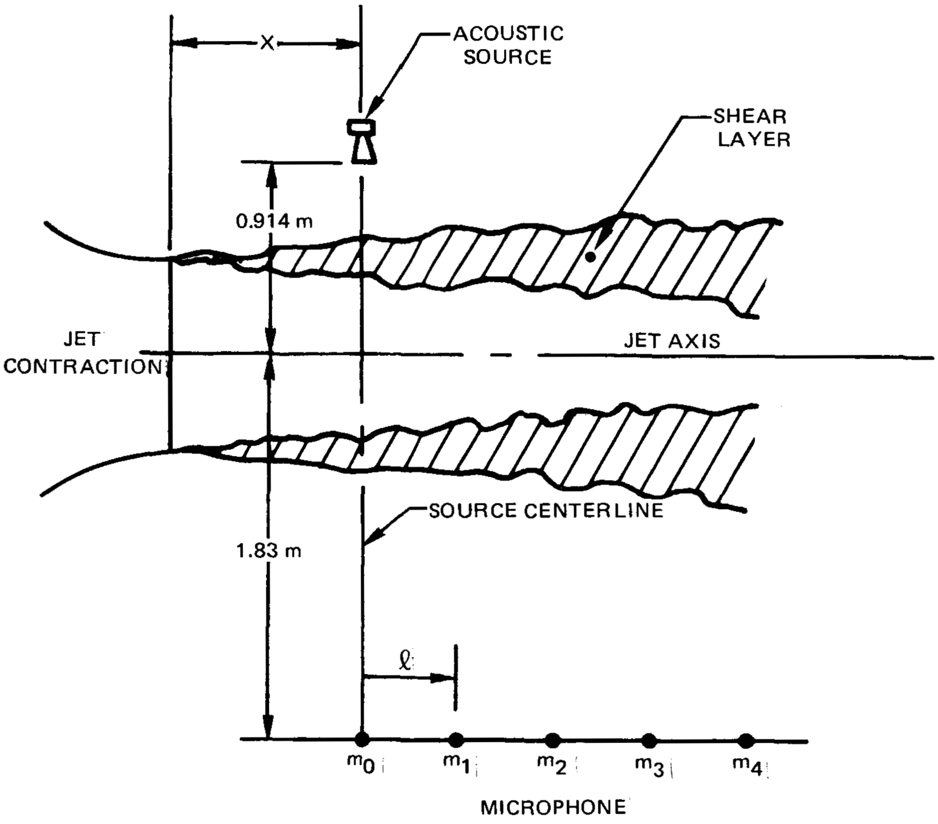

Figure 7—Plan View of Open Jet, Acoustic Source and Far-Field Microphone Arrangement for Discrete Tone Scattering Experiment

78–04–32–3

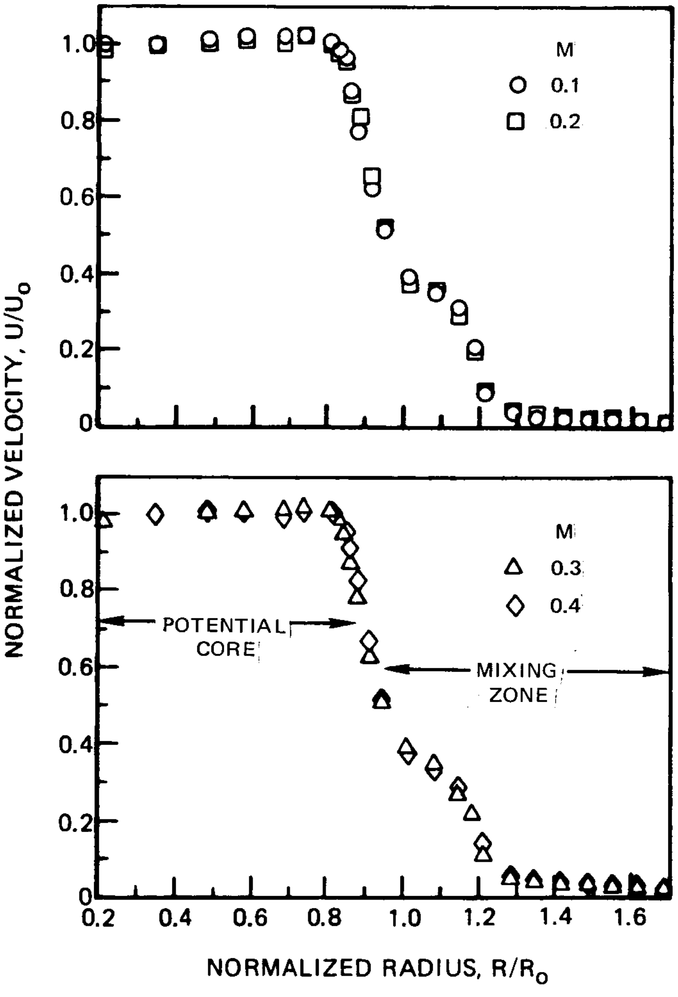

(a) $X/R_0 = 0.66$

Figure 8 — Variation of Normalized Axial Mean Velocity Profiles with Axial Location

78–04–88–1

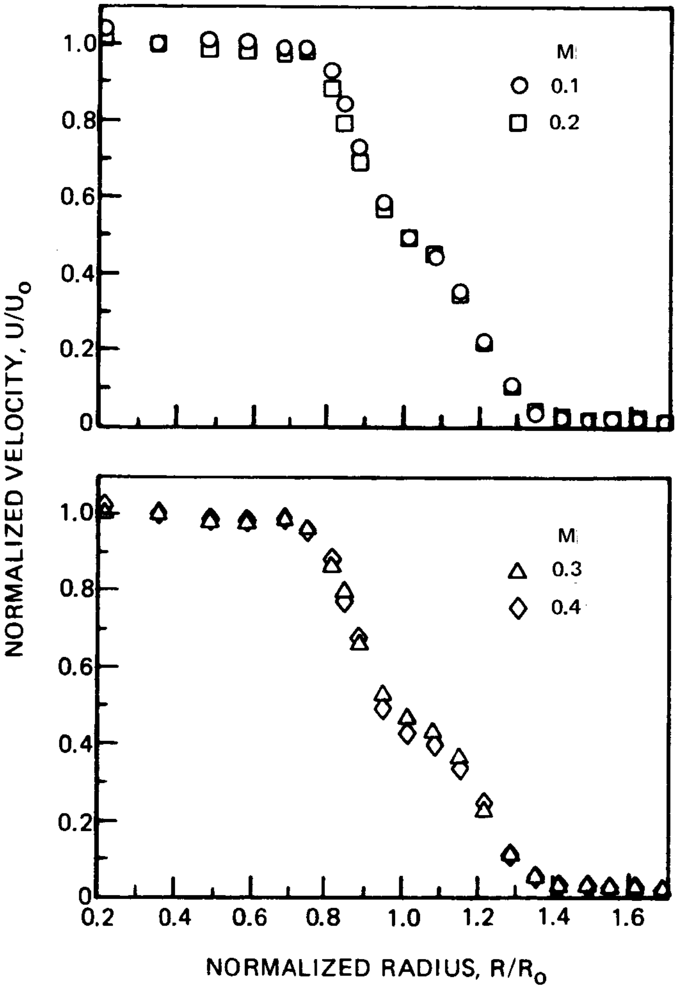

(b) $X/R_o = 1.33$

Figure 8— Continued

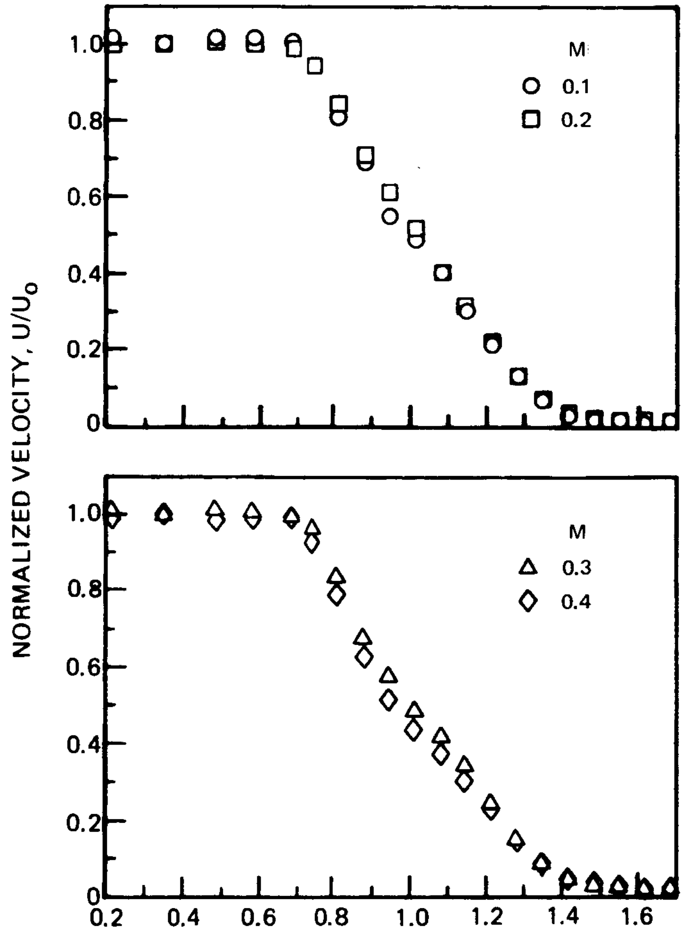

(c) $X/R_0 = 2.0$

Figure 8 — Continued

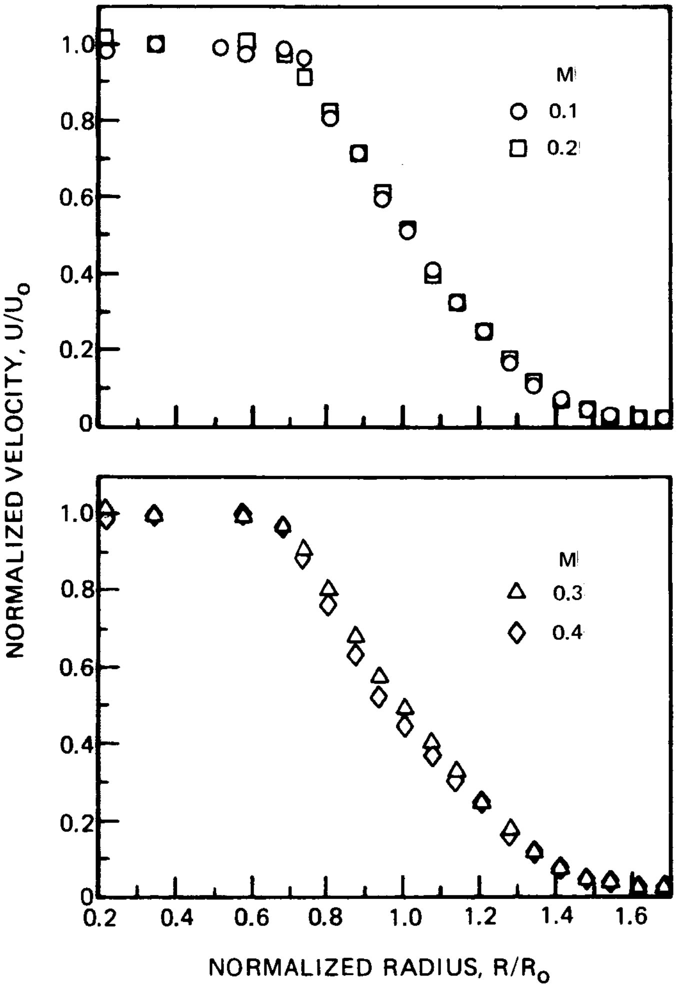

(d) X/R$_0$ = 2.66

Figure 8 — Continued

78–04–88–4

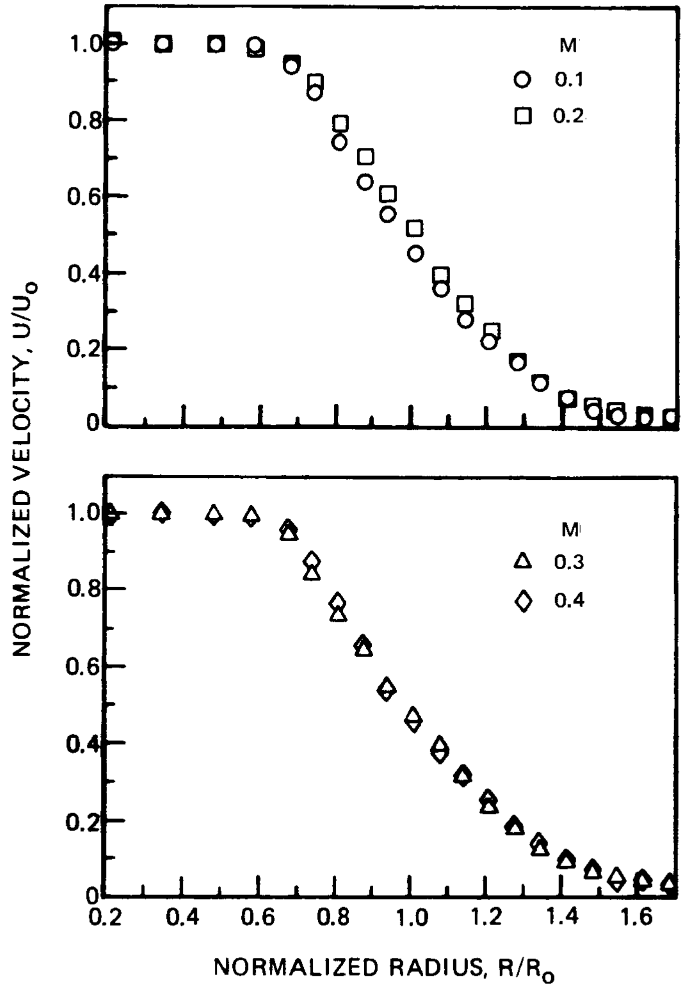

(e) $X/R_0 = 3.33$

Figure 8 – Continued

78–04–88–5

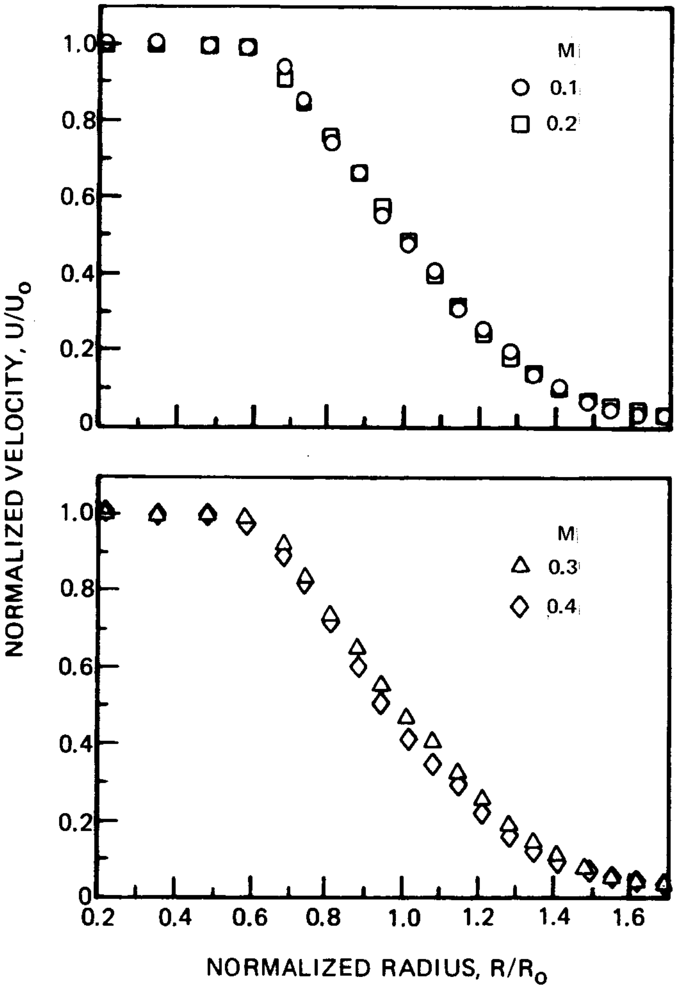

(f) $X/R_0 = 4.0$

Figure 8 — Concluded

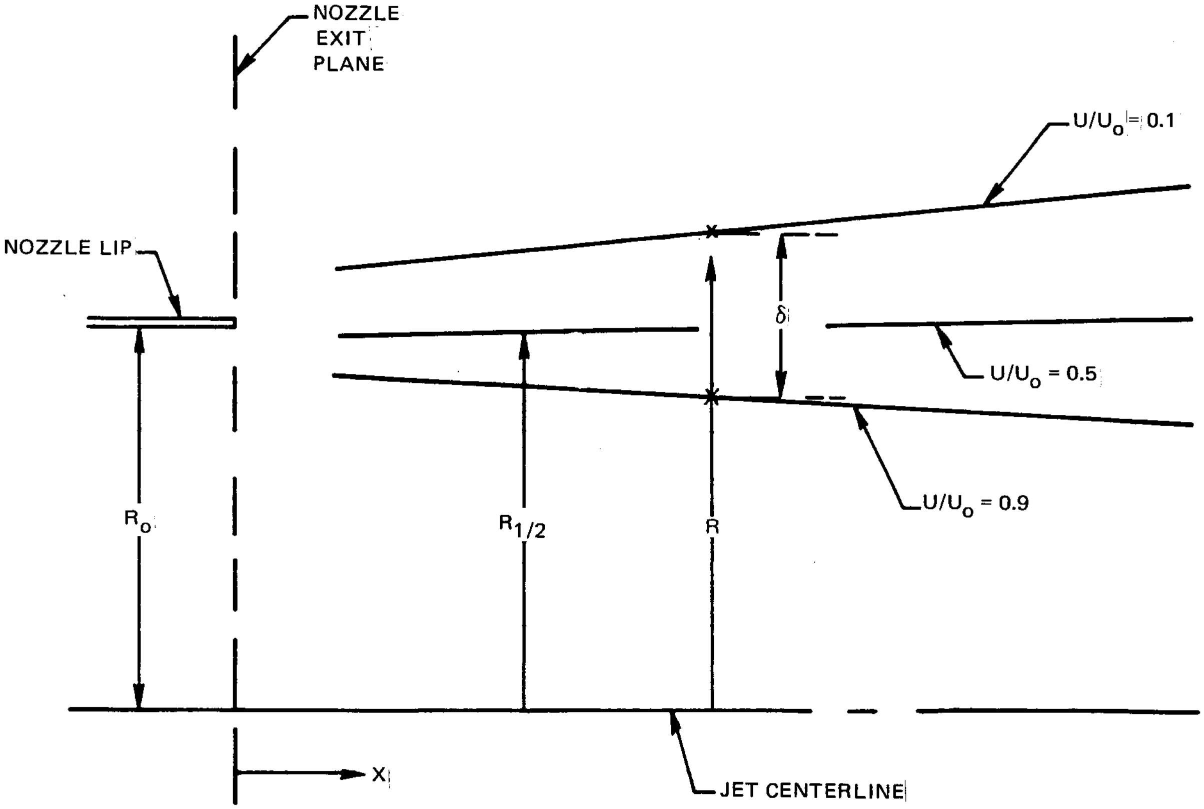

Figure 9 –Shear Layer Coordinates

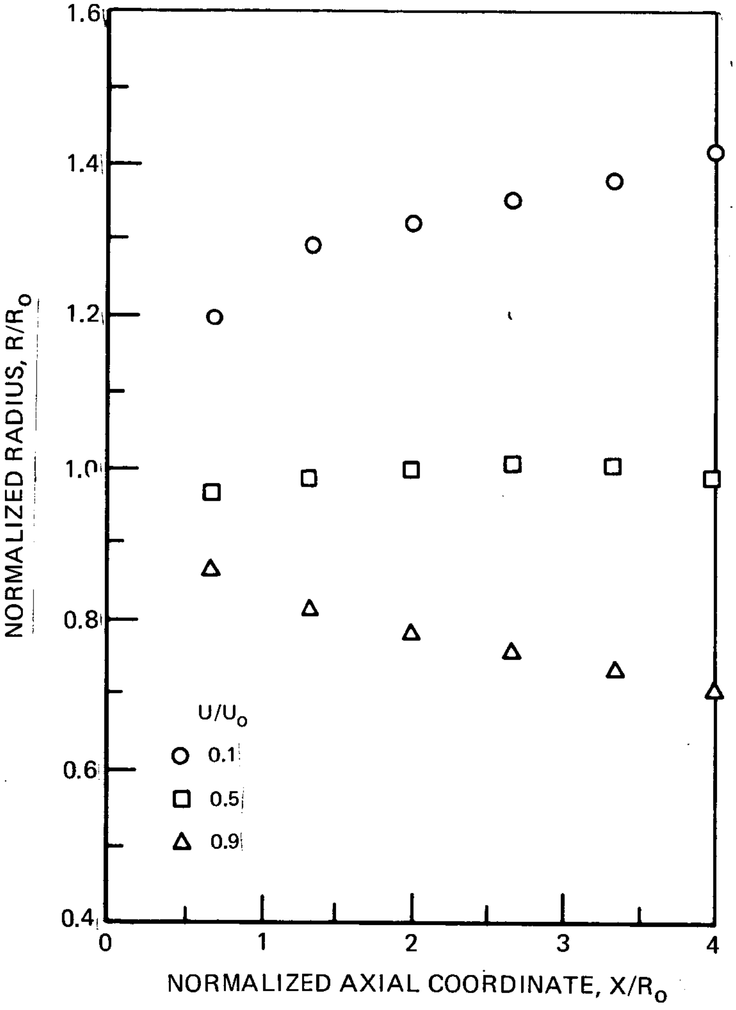

Figure 10 – Axial Variation of Average Shear Layer Characteristics

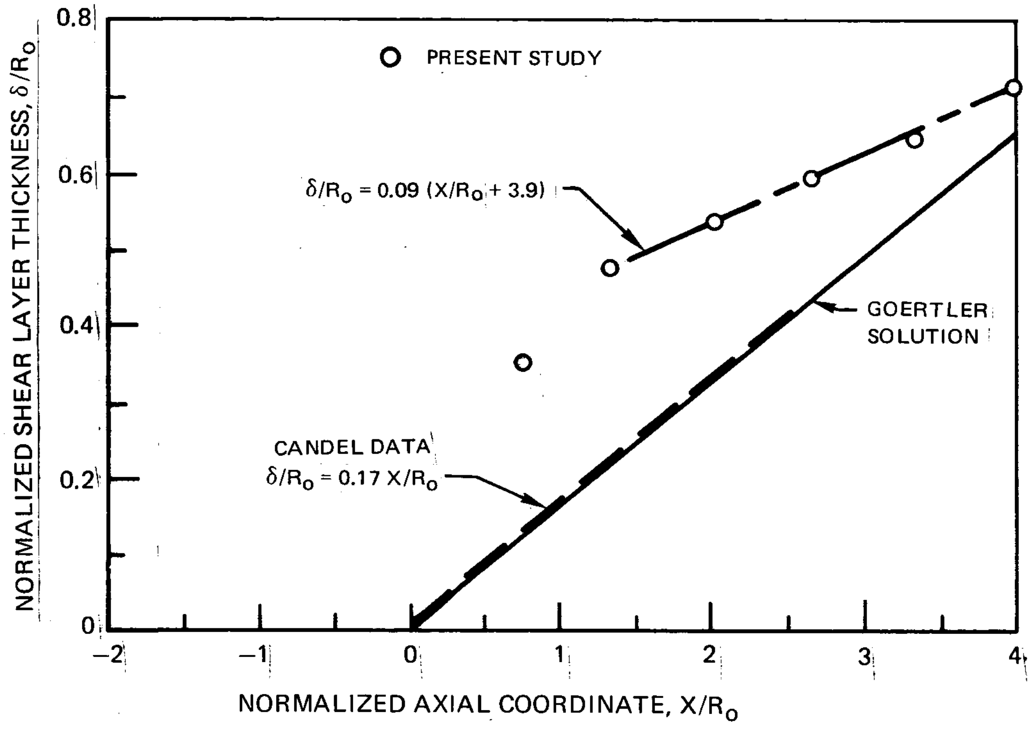

Figure 11 – Axial Variation of Shear Layer Thickness

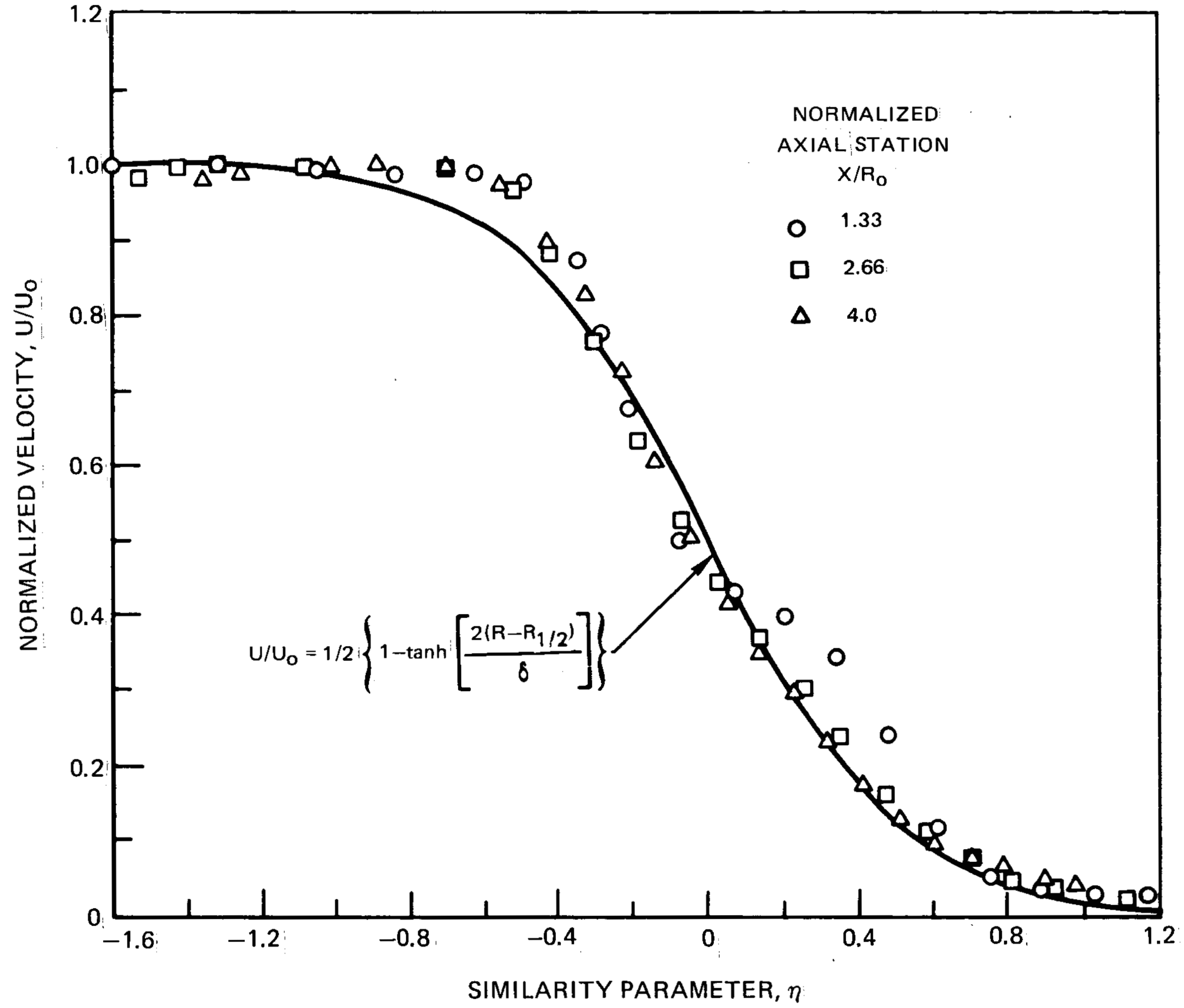

Figure 12 —Similarity of Velocity Profiles at Various Axial Locations for Mach Number, M = 0.4

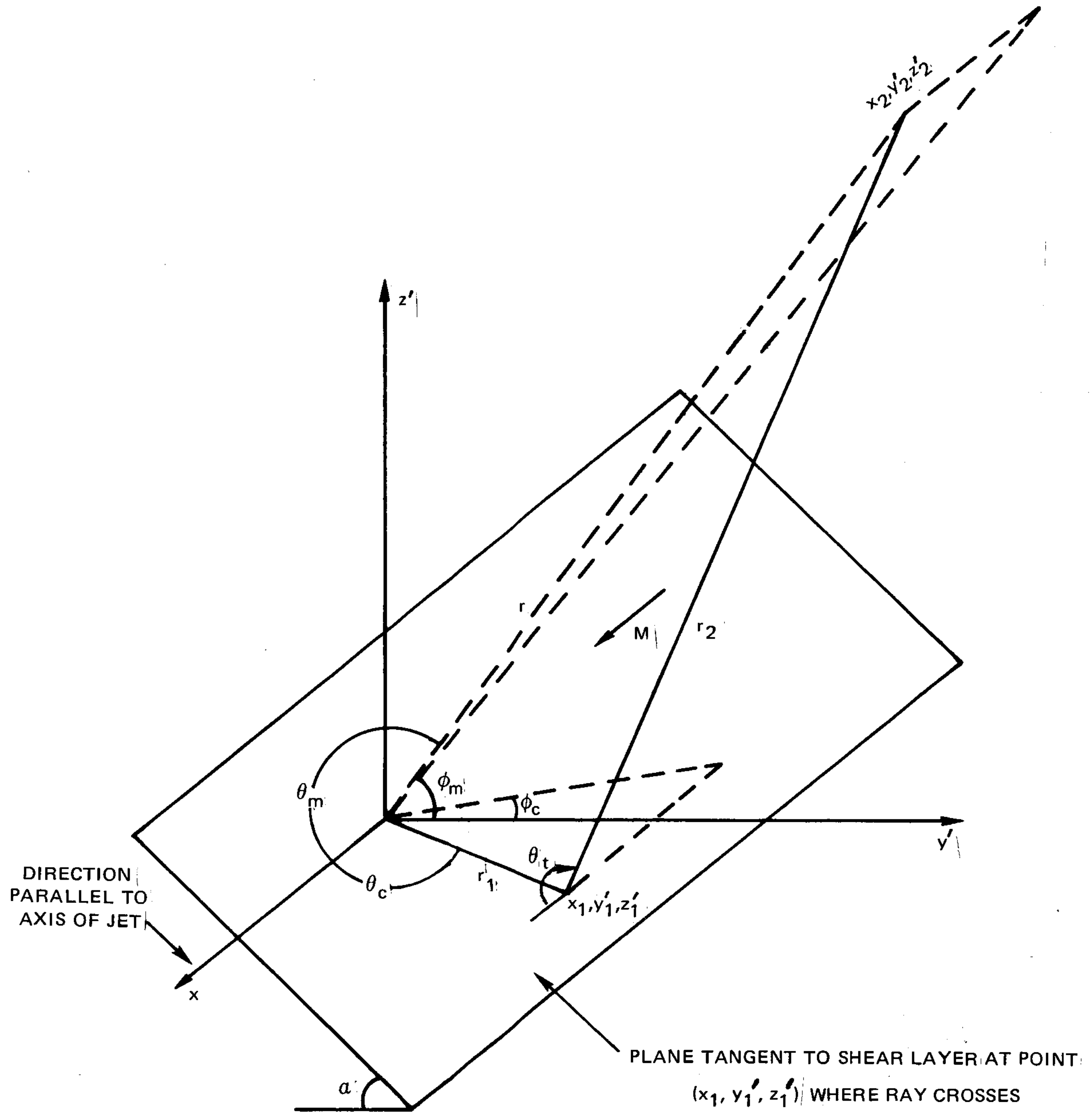

Figure 13 —Geometry for Theoretical Model

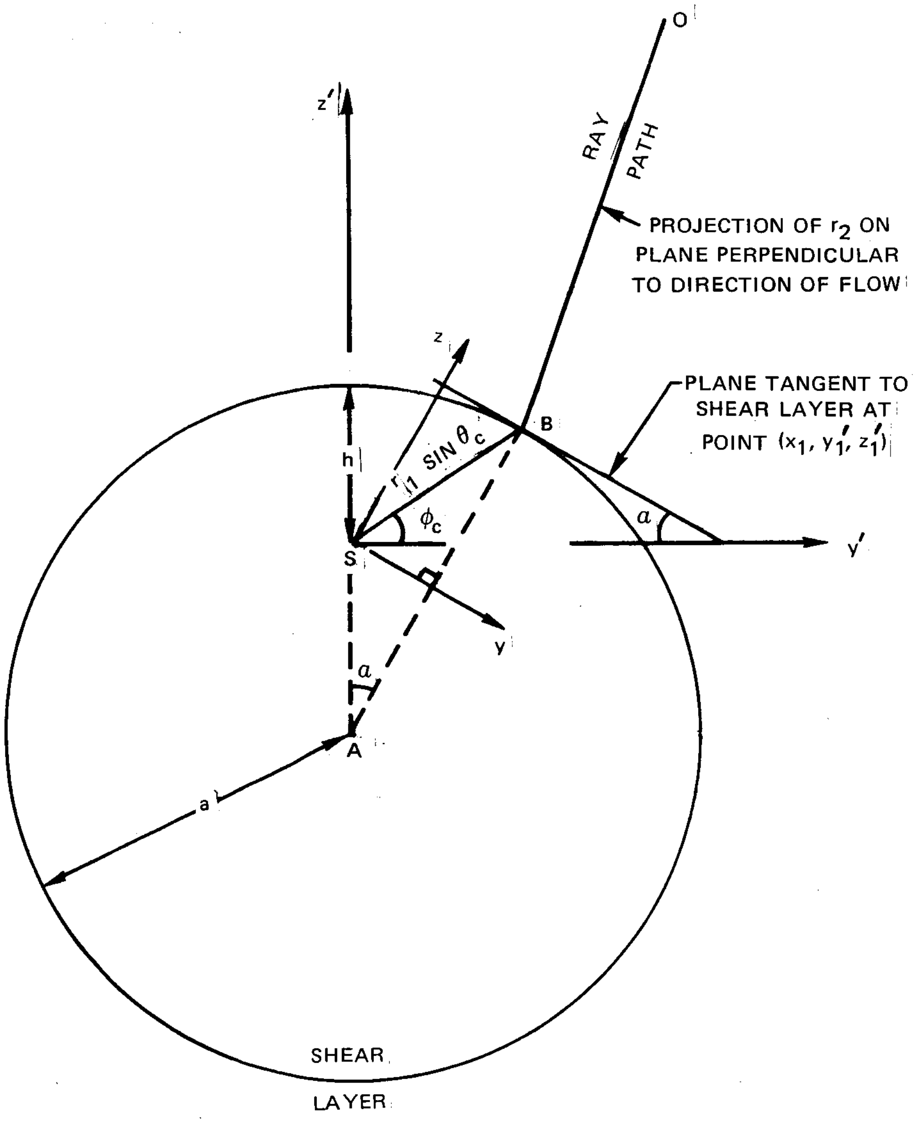

Figure 14 —Cross—Sectional Geometry for Theoretical Model

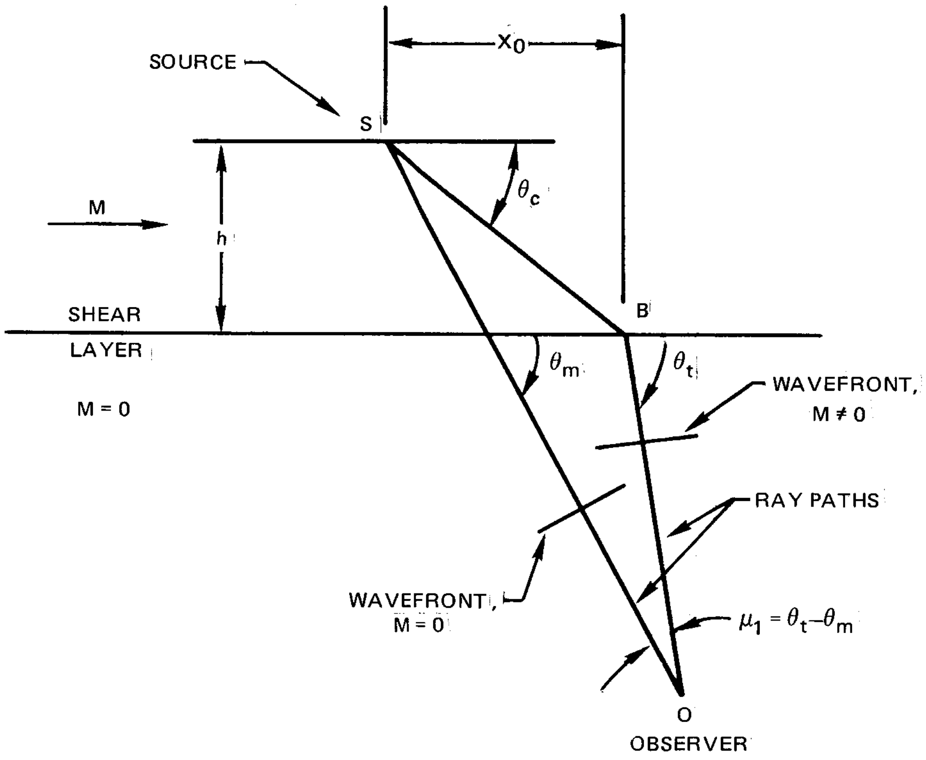

Figure 15 — Geometry for Transmission of Sound Through a Shear Layer

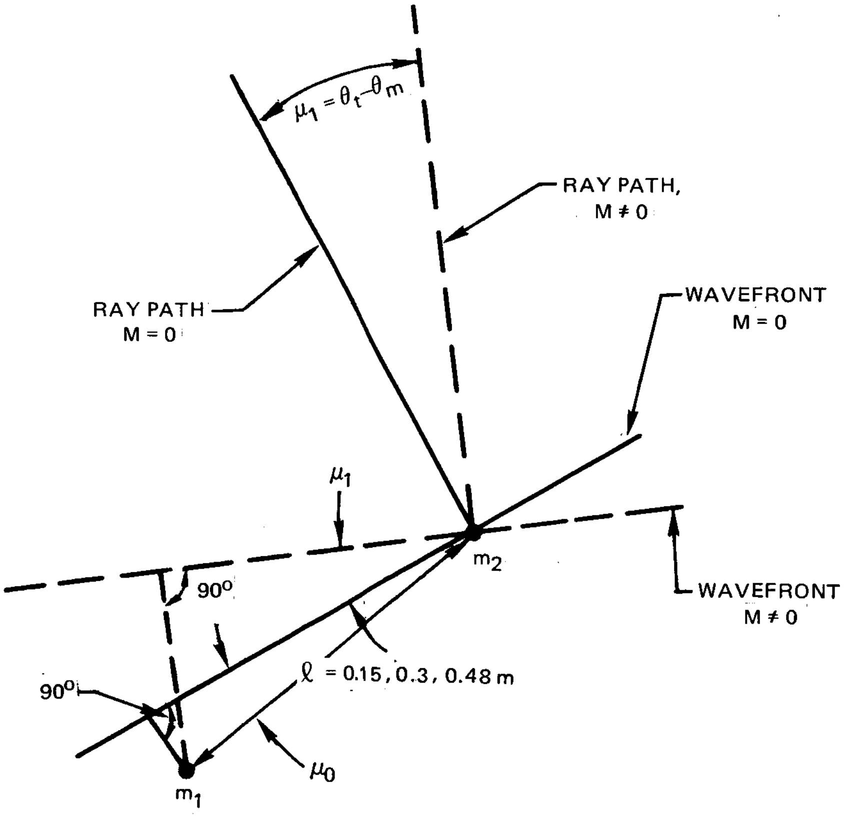

Figure 16— Model of Wavefront Angle Changes at Far–Field Microphone Location

78–04–55–6

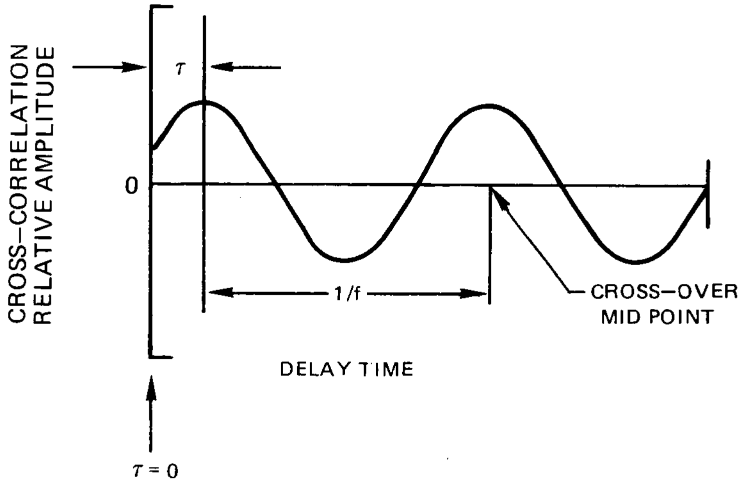

Figure 17 – Two Microphone Cross – Correlation Function at M = 0

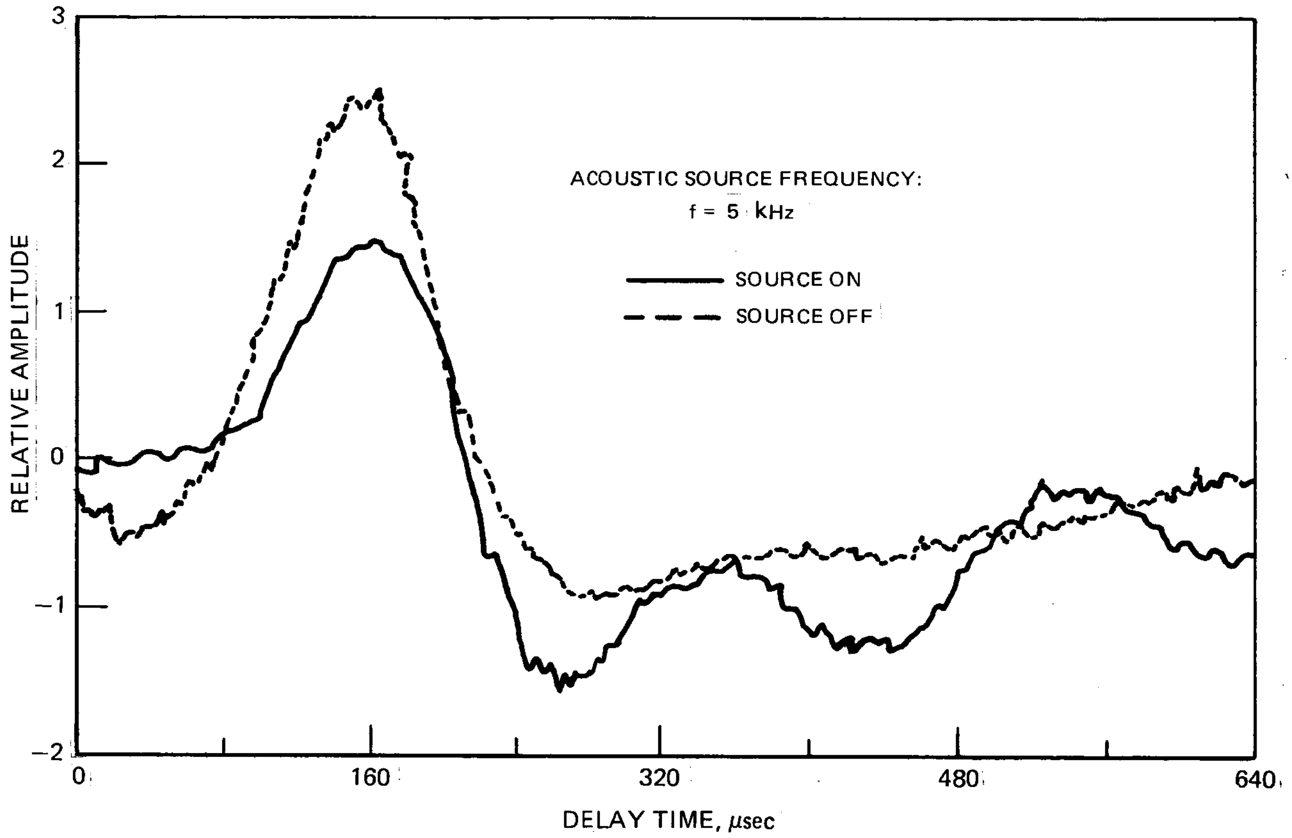

Figure 18 – Two Microphone Cross–Correlation Function at Mach Number, M = 0.4, Measurement Angle, $\theta_m = 37.5^o$, Test Configuration 1.

78–04–55–4

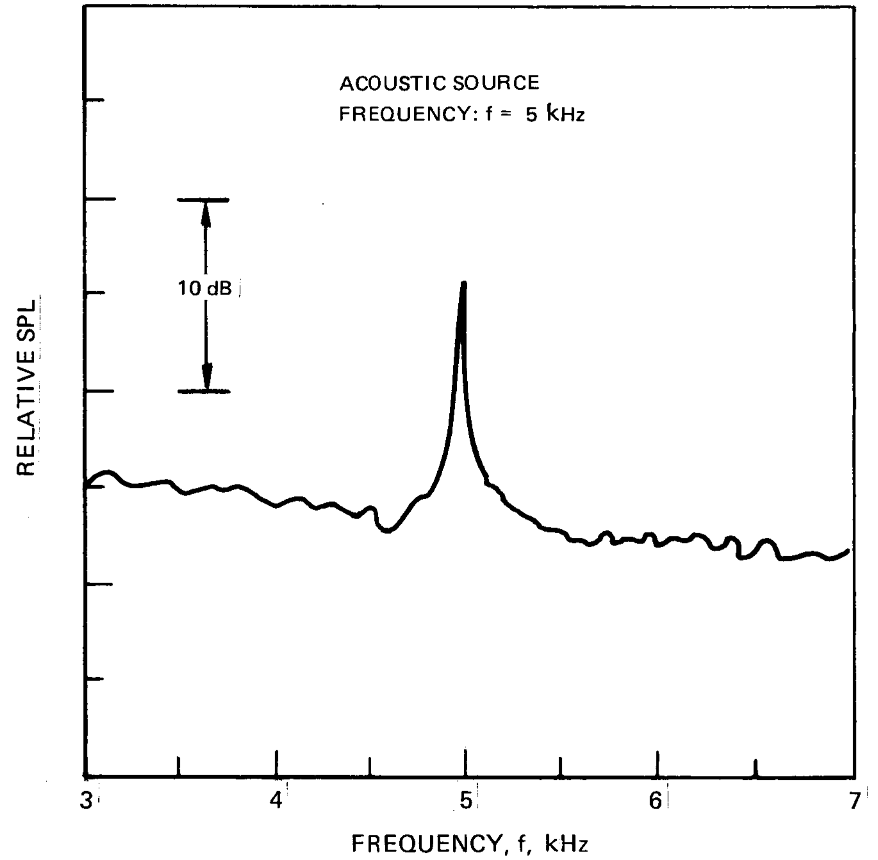

Figure 19 — Typical Far–Field Microphone Spectrum at Mach Number, M = 0.4, Measurement Angle, $\theta_m = 37.5^{\circ}$, Test Configuration 1.

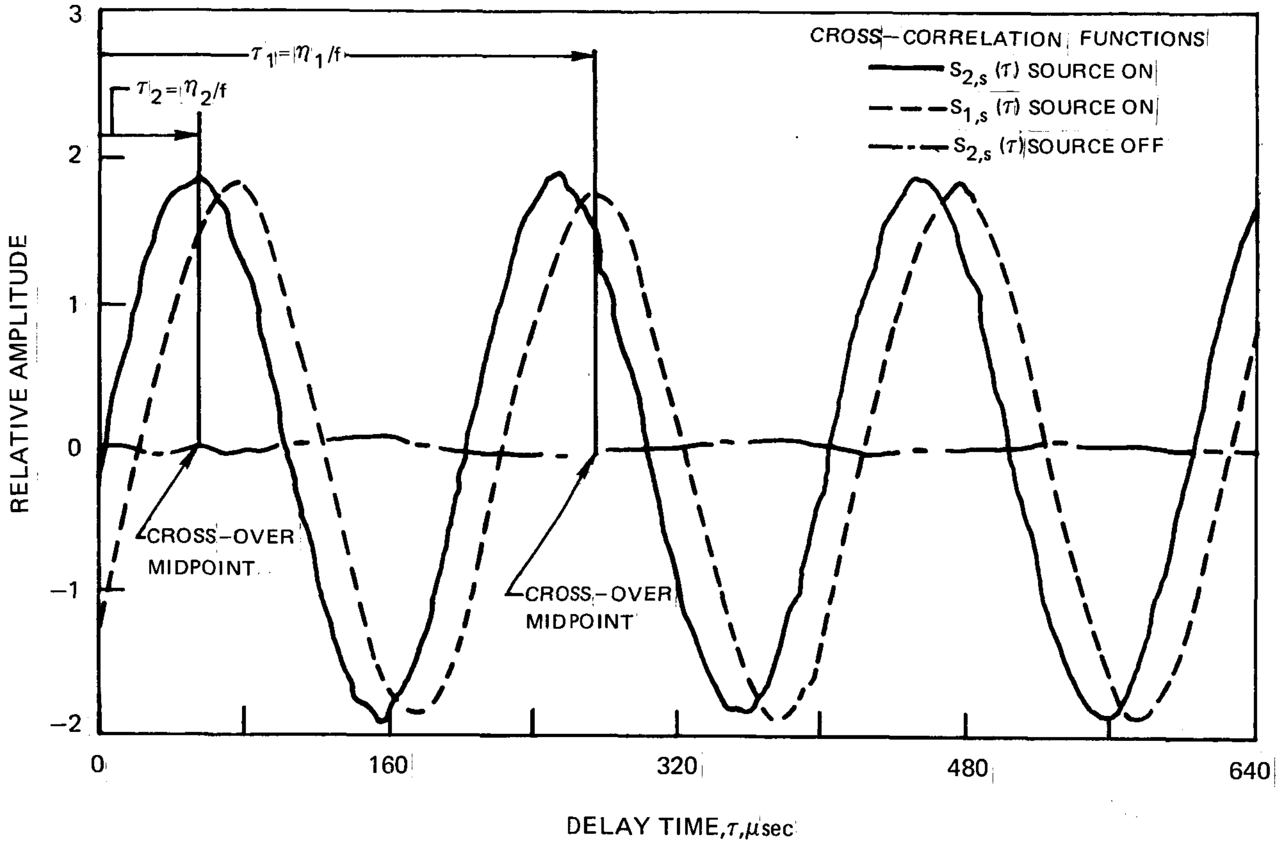

Figure 20–Microphone–Signal Generator Cross–Correlation at Mach Number, M = 0.4, Frequency, f = 10 kHz Measurement Angle, $\theta_m = 37.5^{\circ}$, Test Configuration 1.

78–04–96–2

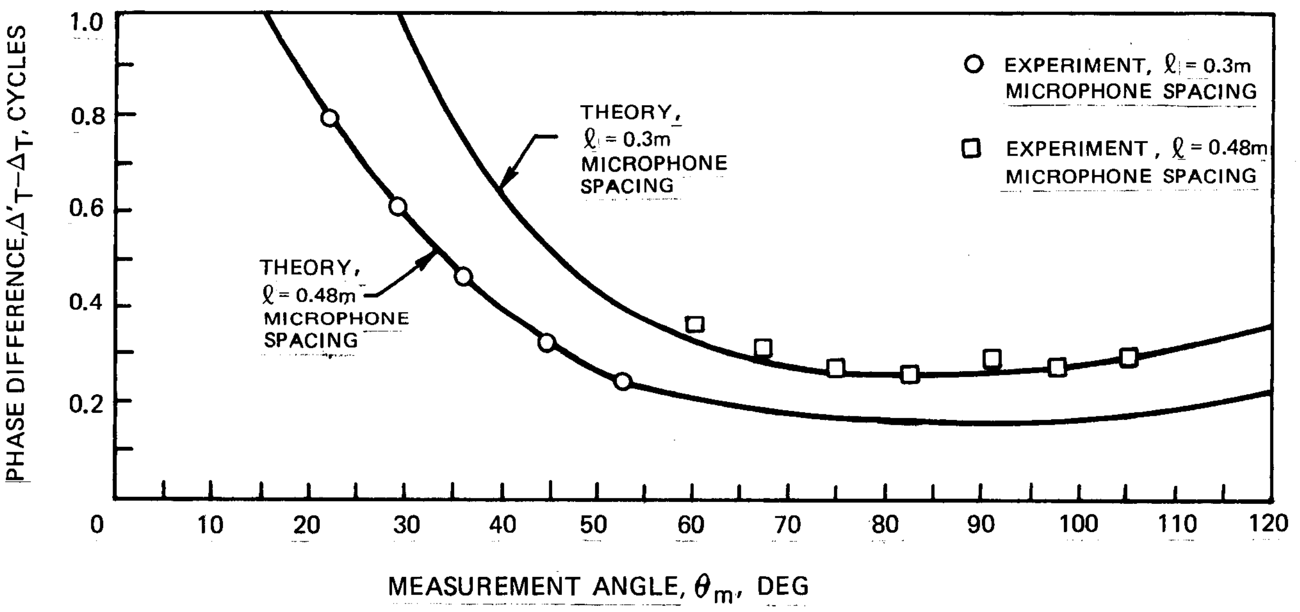

Figure 21—Comparison of Measured and Theoretical Phase Difference at Mach Number, M = 0.3, Frequency, f = 2.5 kHz, Test Configuration 1.

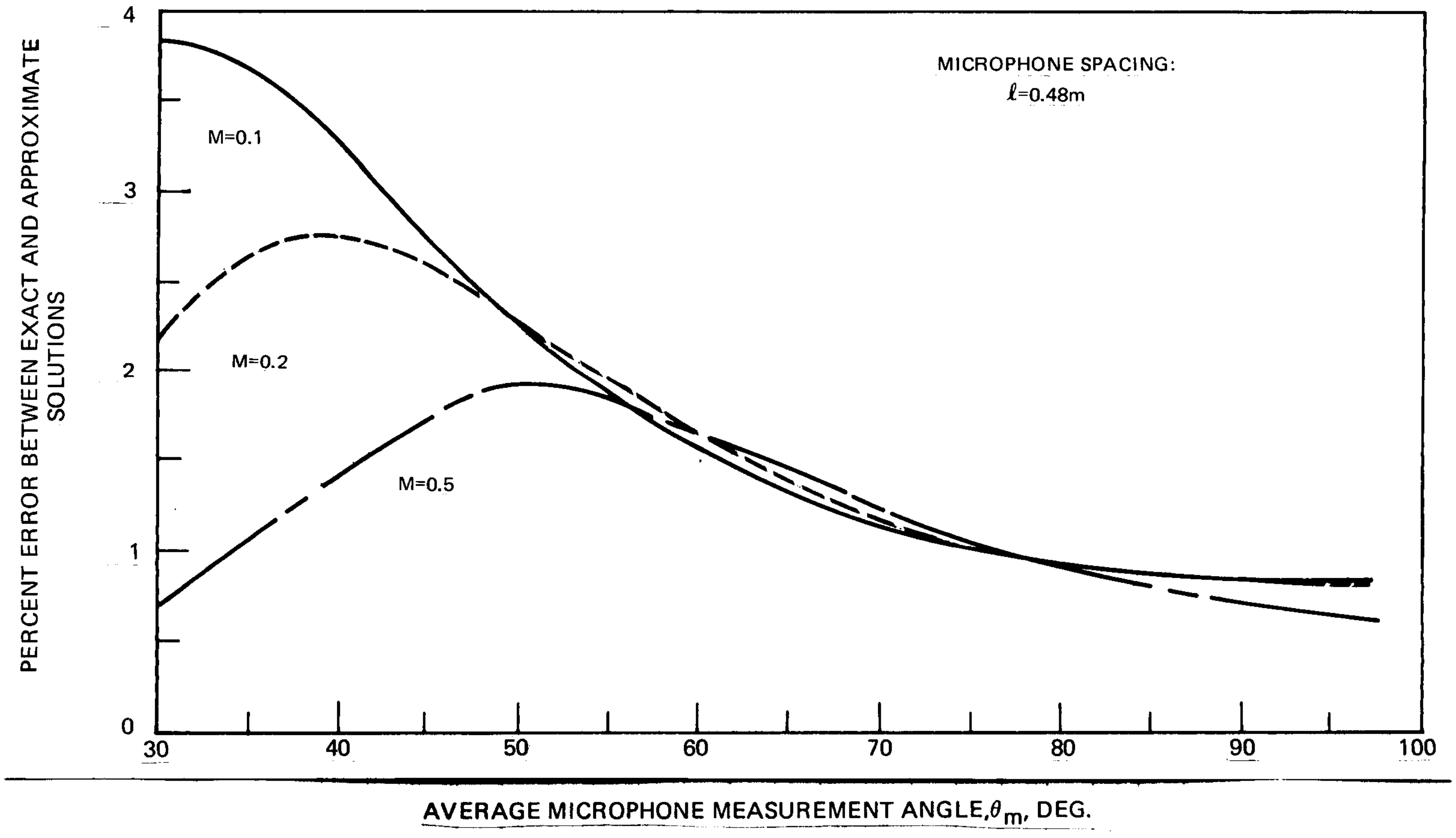

Figure 22 — Assessment of Error Due to Plane–Wave Propagation Assumption

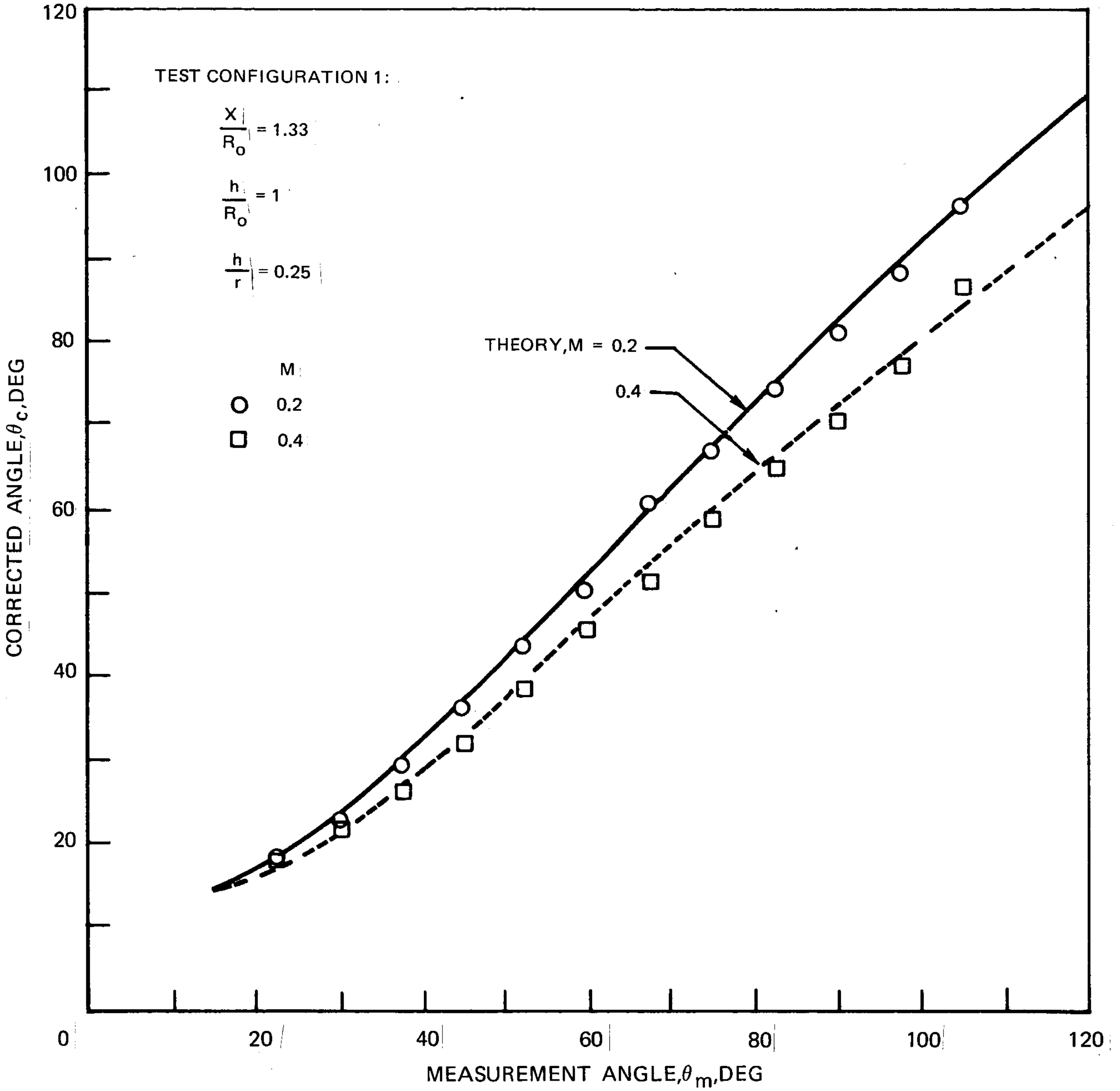

(a) f = 10 kHz

Figure 23— Comparison of Measured and Theoretical Refraction Angle Correction as a Function of Mach Number and Frequency. Test Configuration 1.

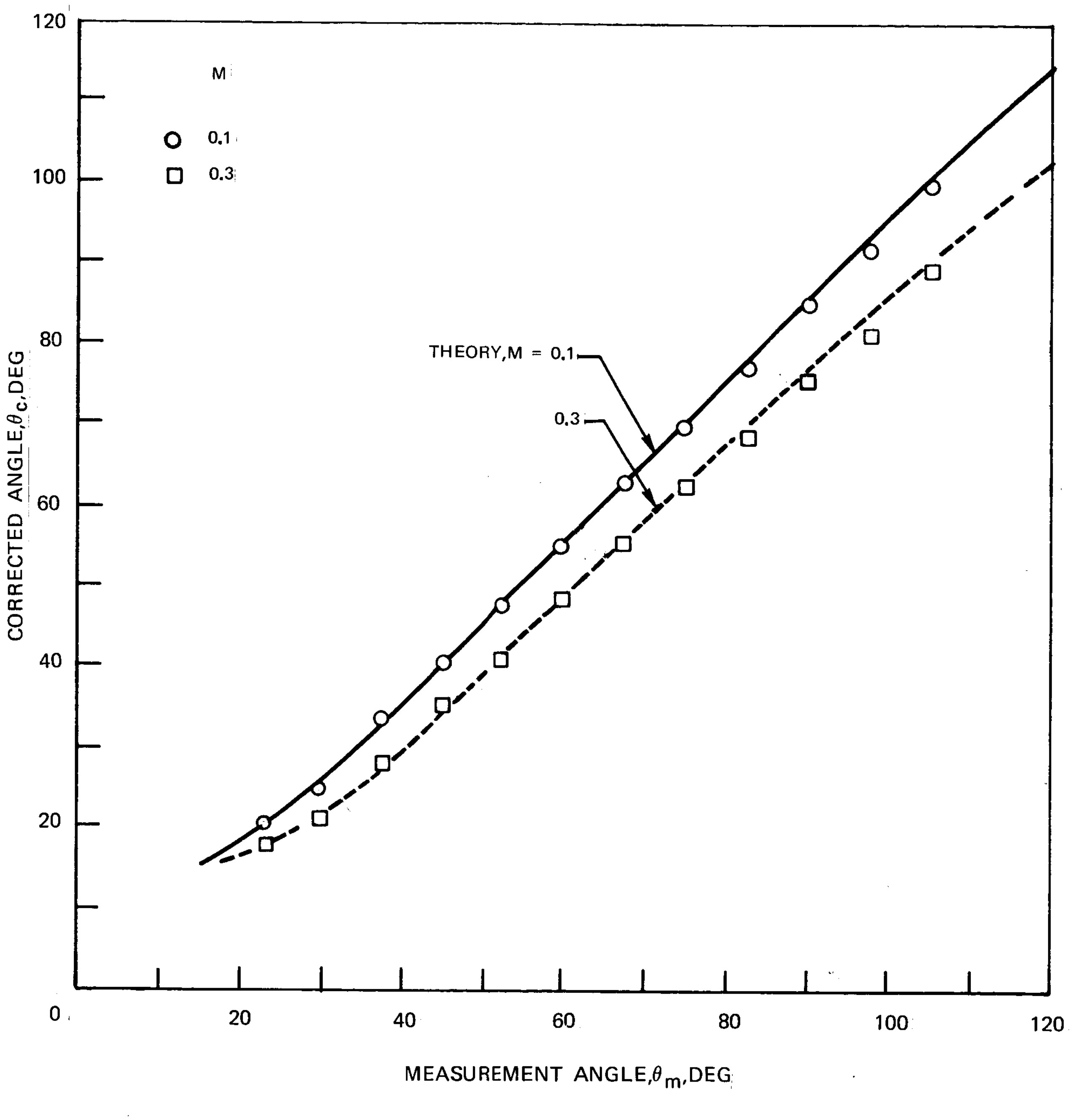

(b) f = 10 kHz

Figure 23 — Continued

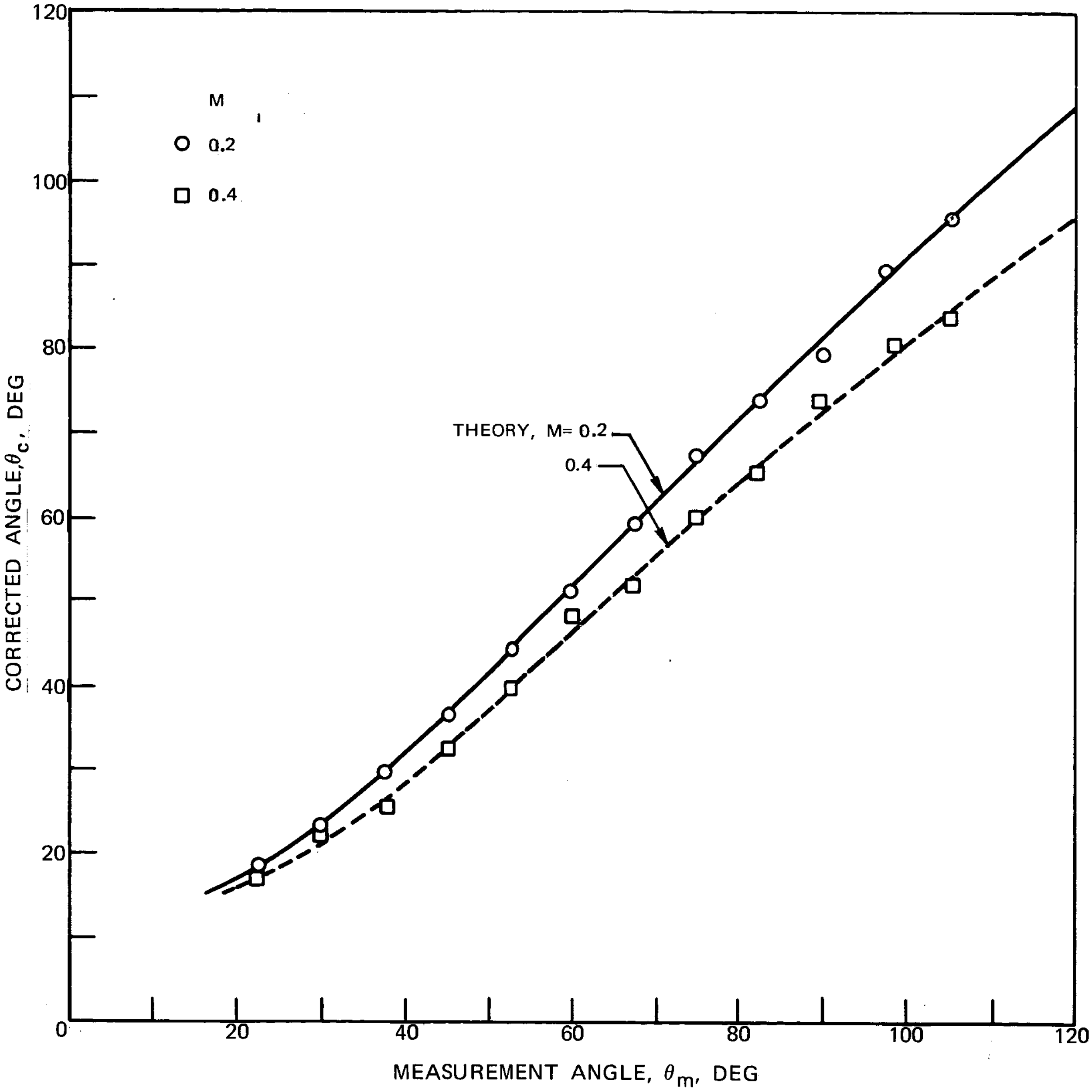

(c) f = 5 kHz

Figure 23 — Continued

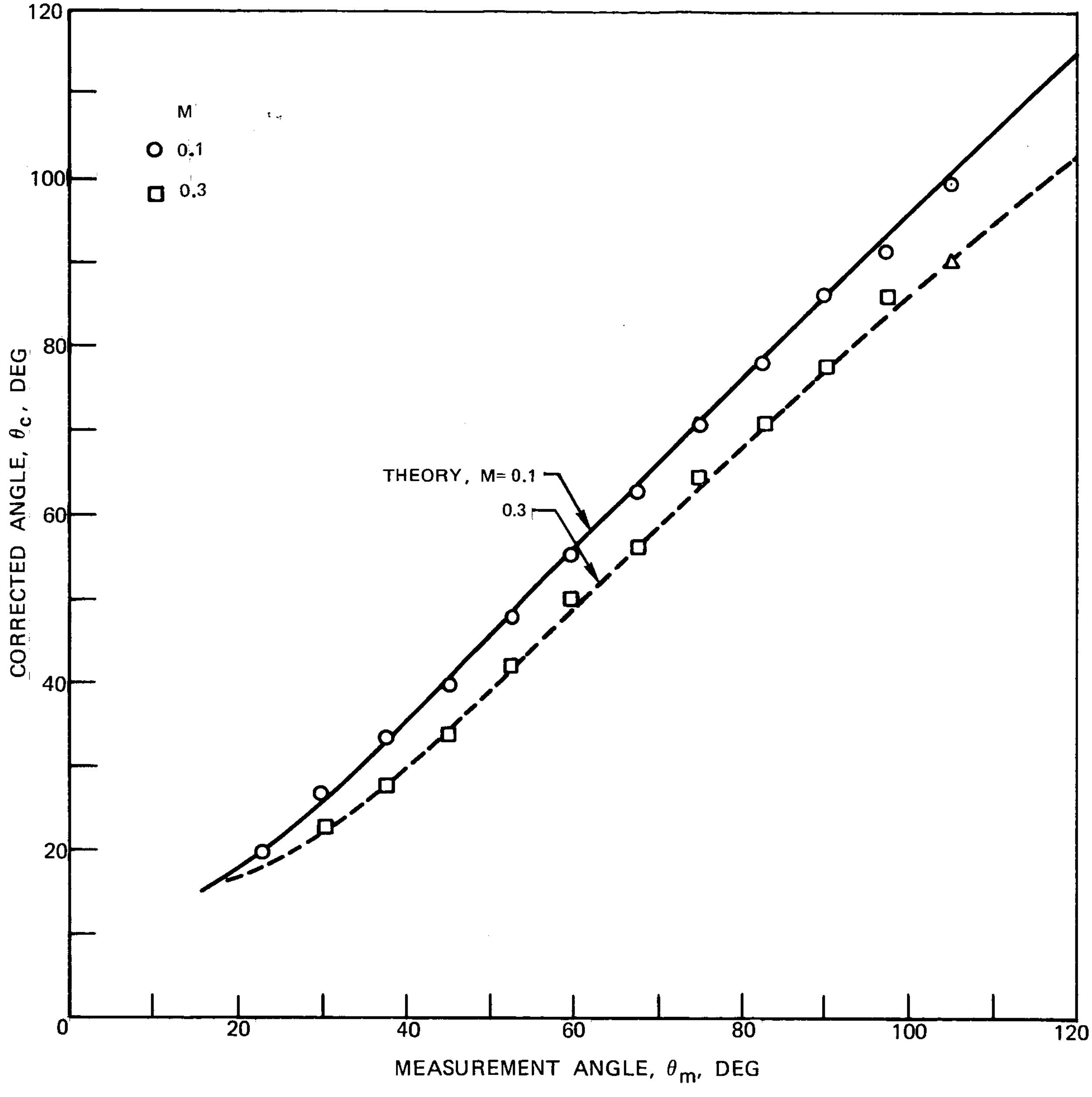

(d) f = 5 kHz

Figure 23 — Continued

77–12–69–3

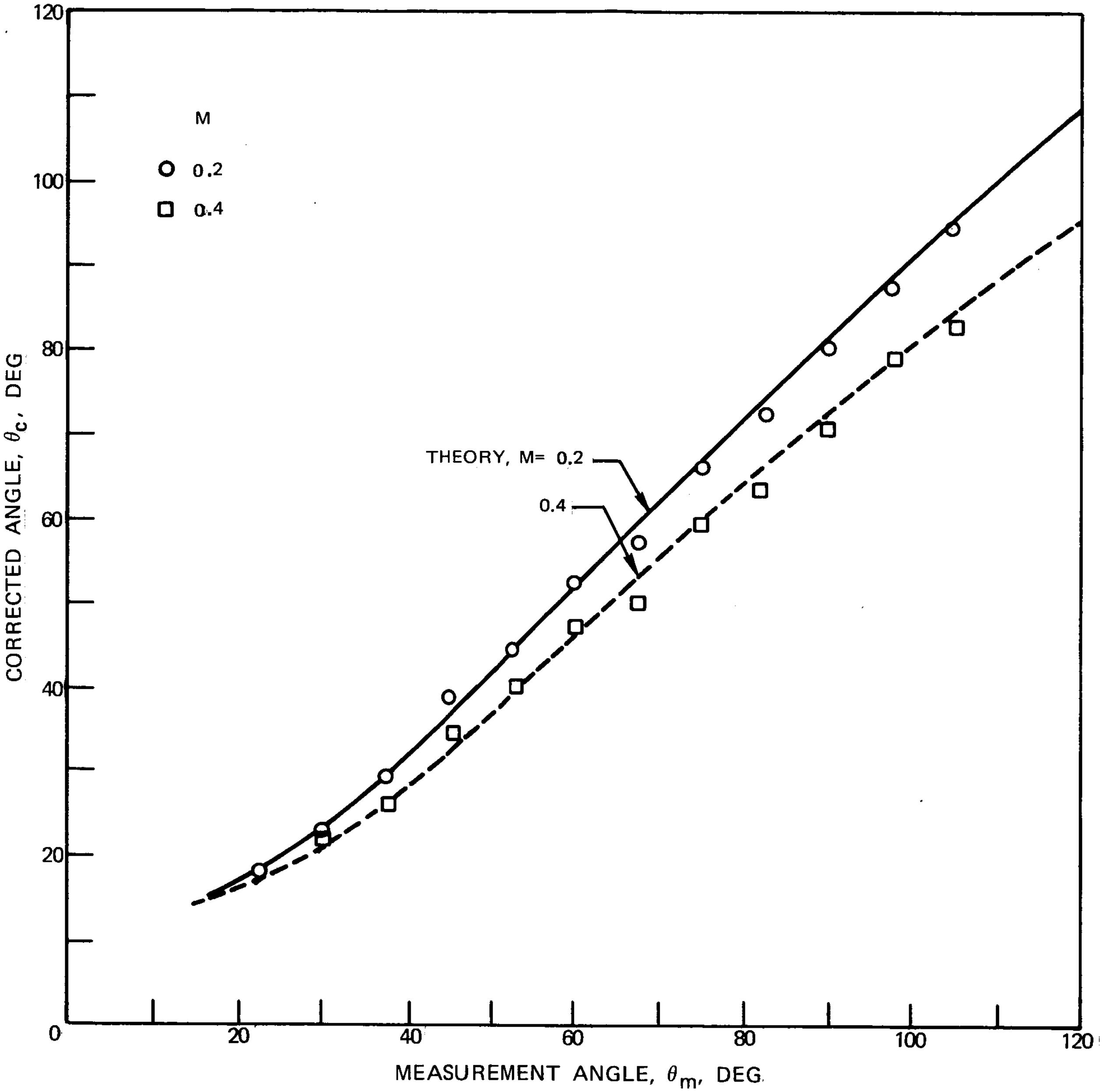

(e) f = 2.5 kHz

Figure 23 – Continued

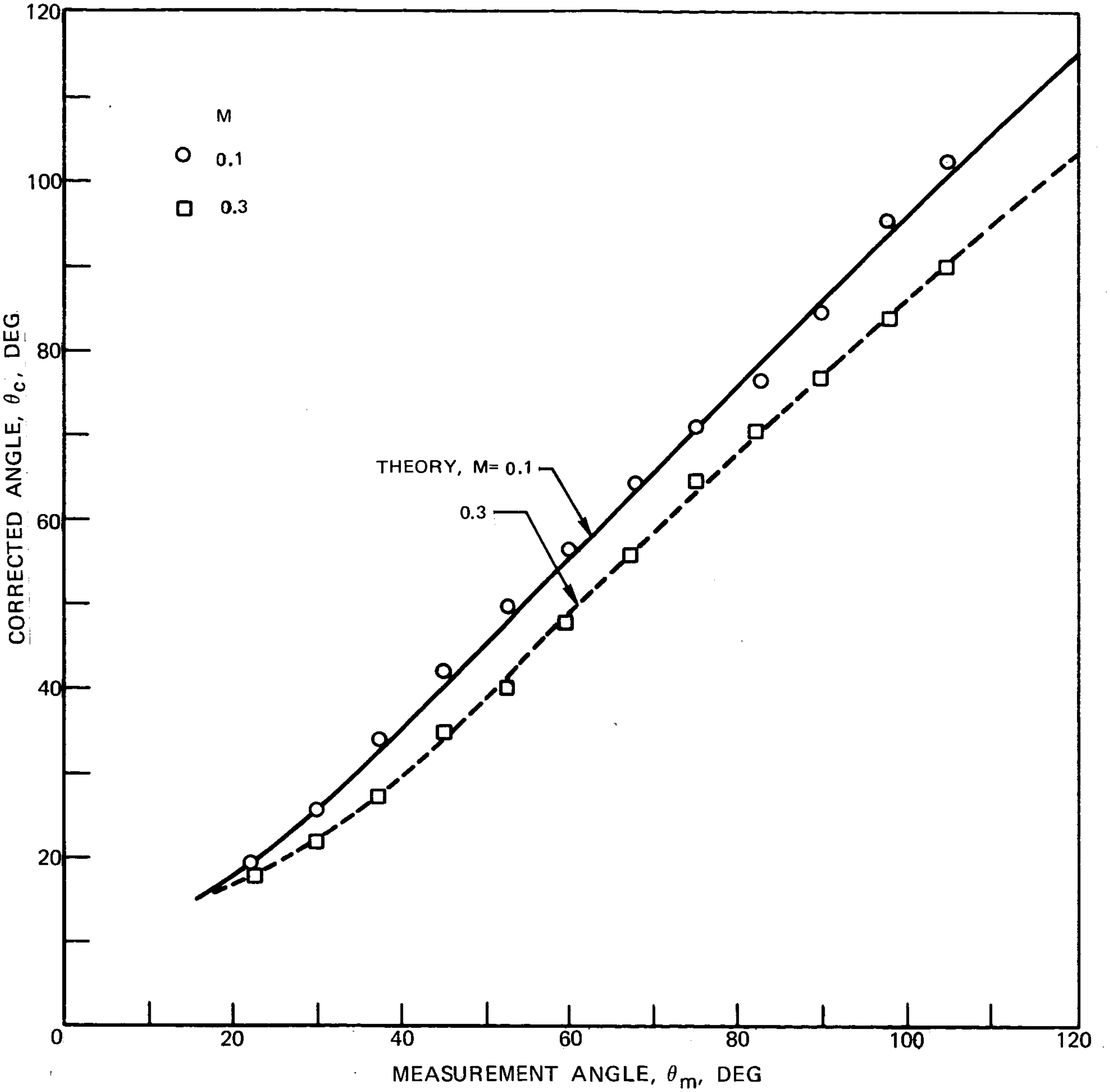

(f) f = 2.5 kHz

Figure 23 — Continued

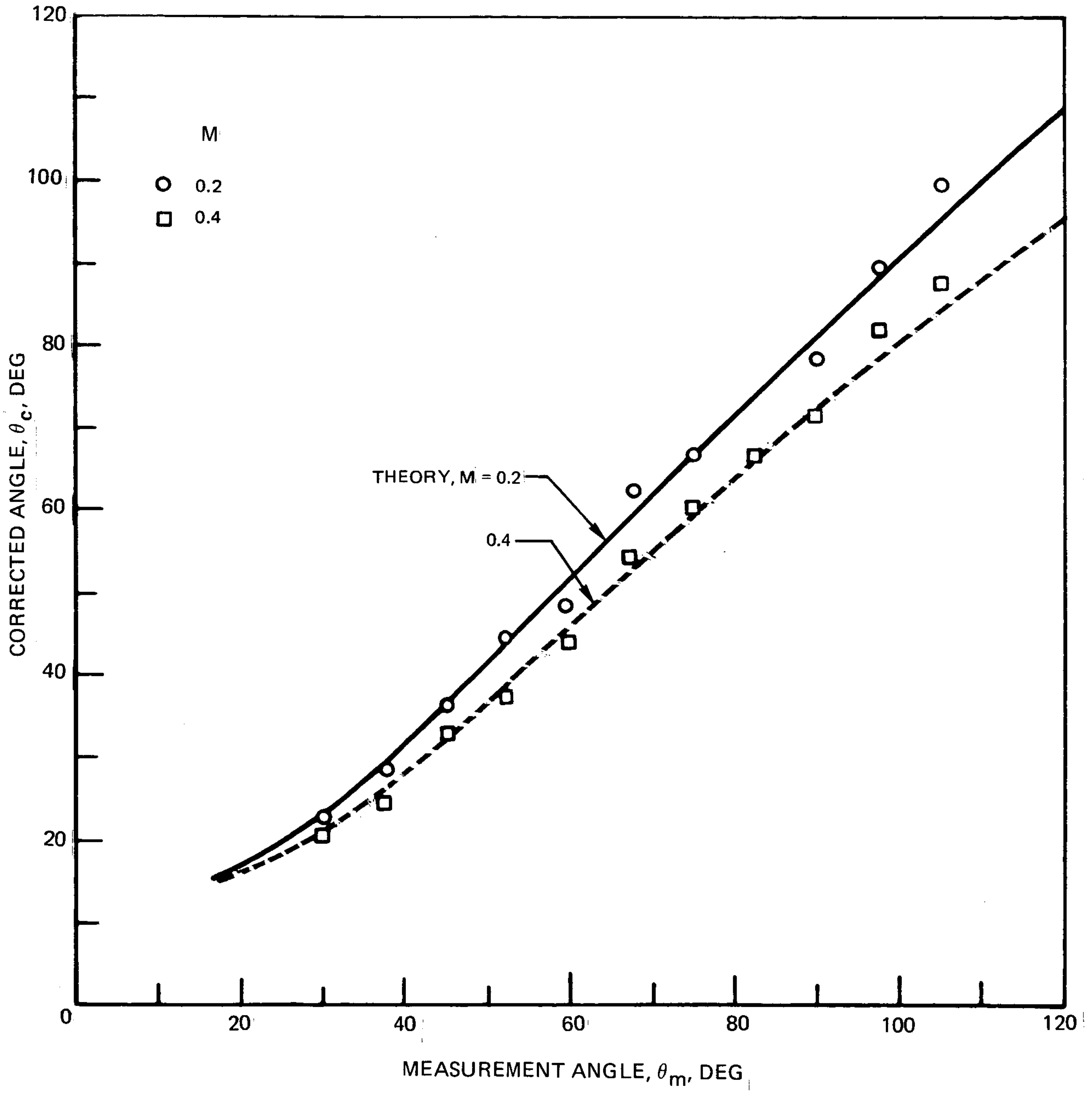

(g) f = 1 kHz

Figure 23– Continued

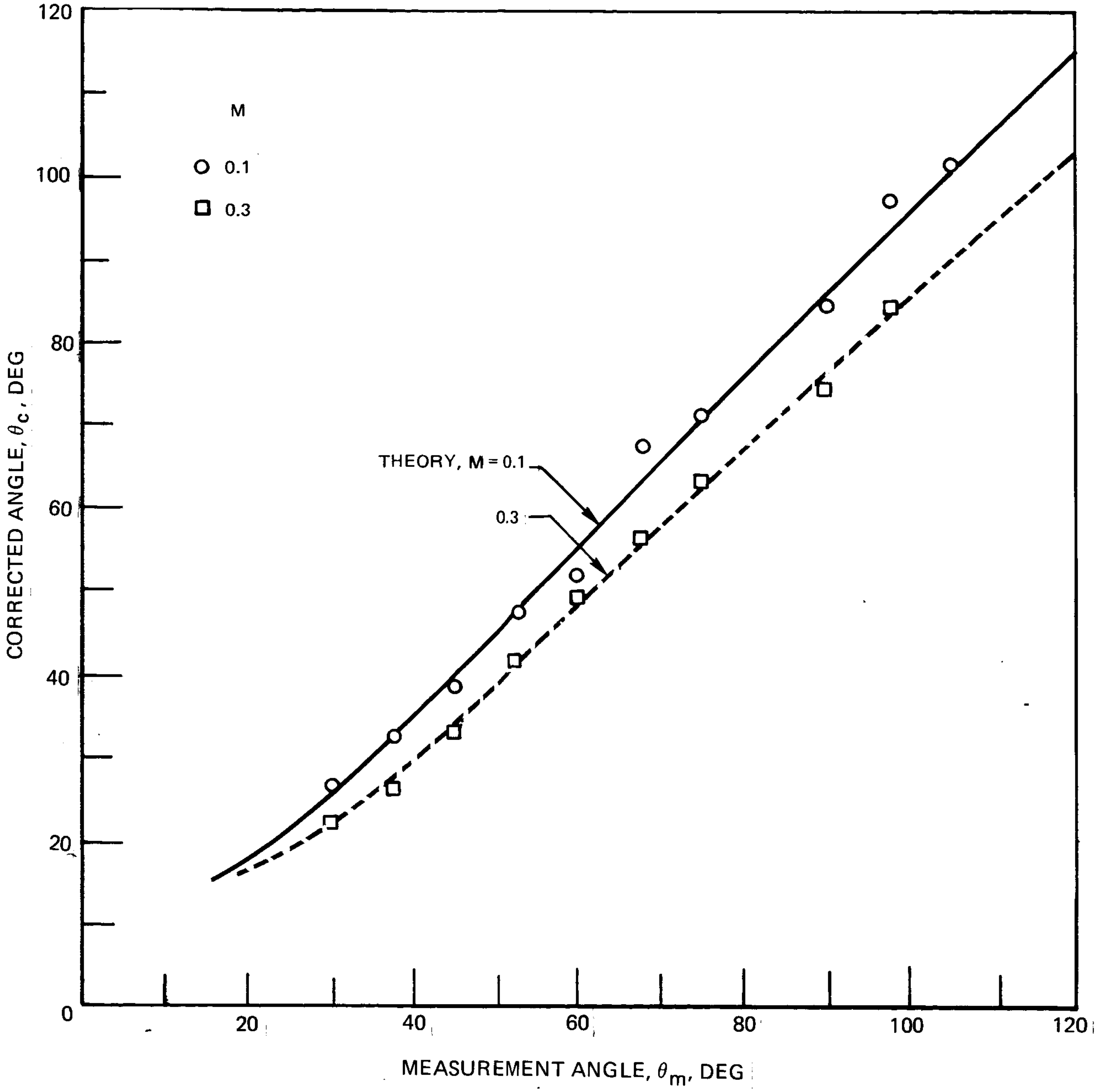

(h) f = 1 kHz

Figure 23— Concluded

77–12–93–1

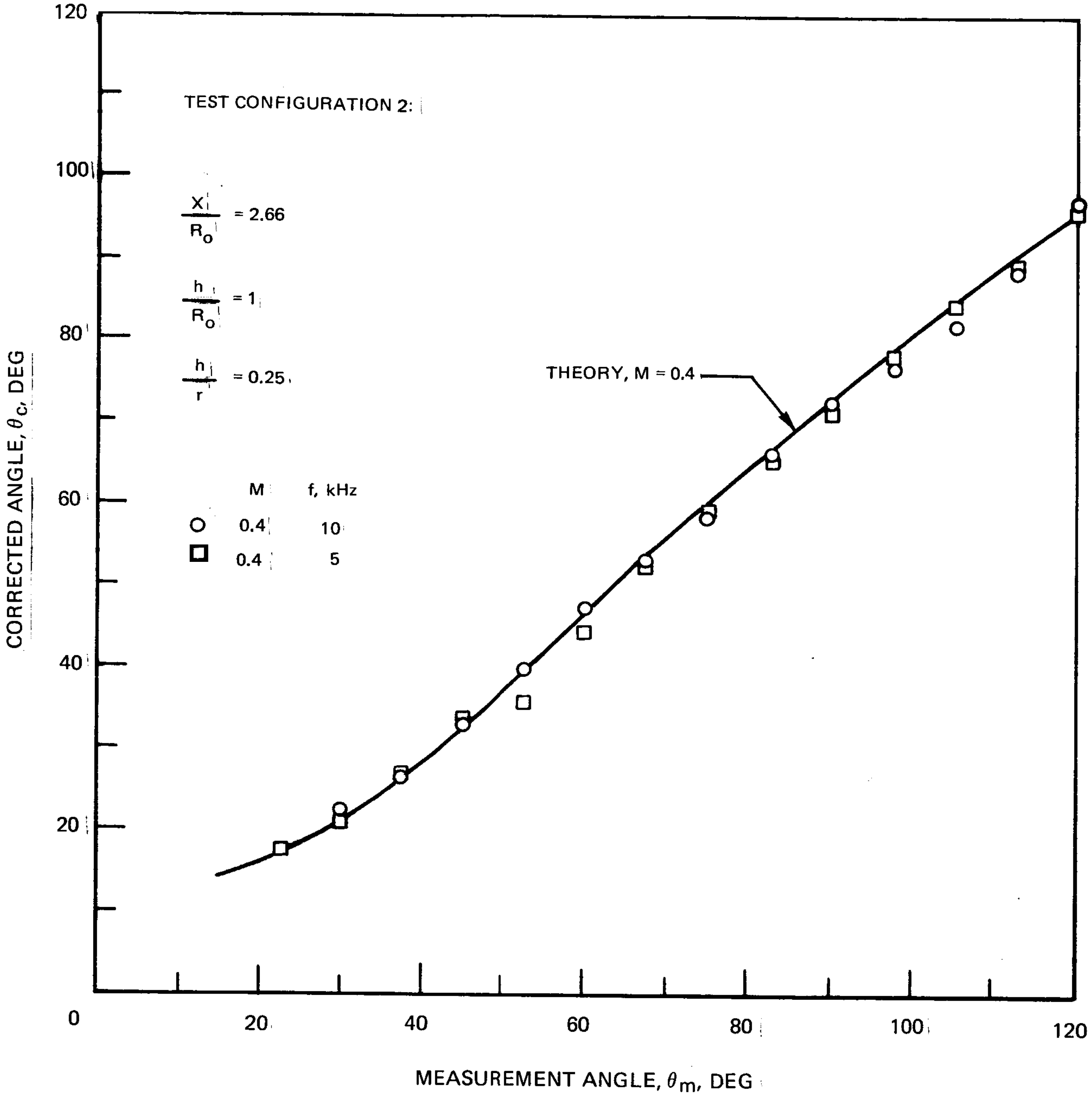

(a) f = 10, 5 kHz

Figure 24 – Comparison of Experimental and Theoretical Refraction Angle Correction as a Function of Mach Number and Frequency. Test Configuration 2.

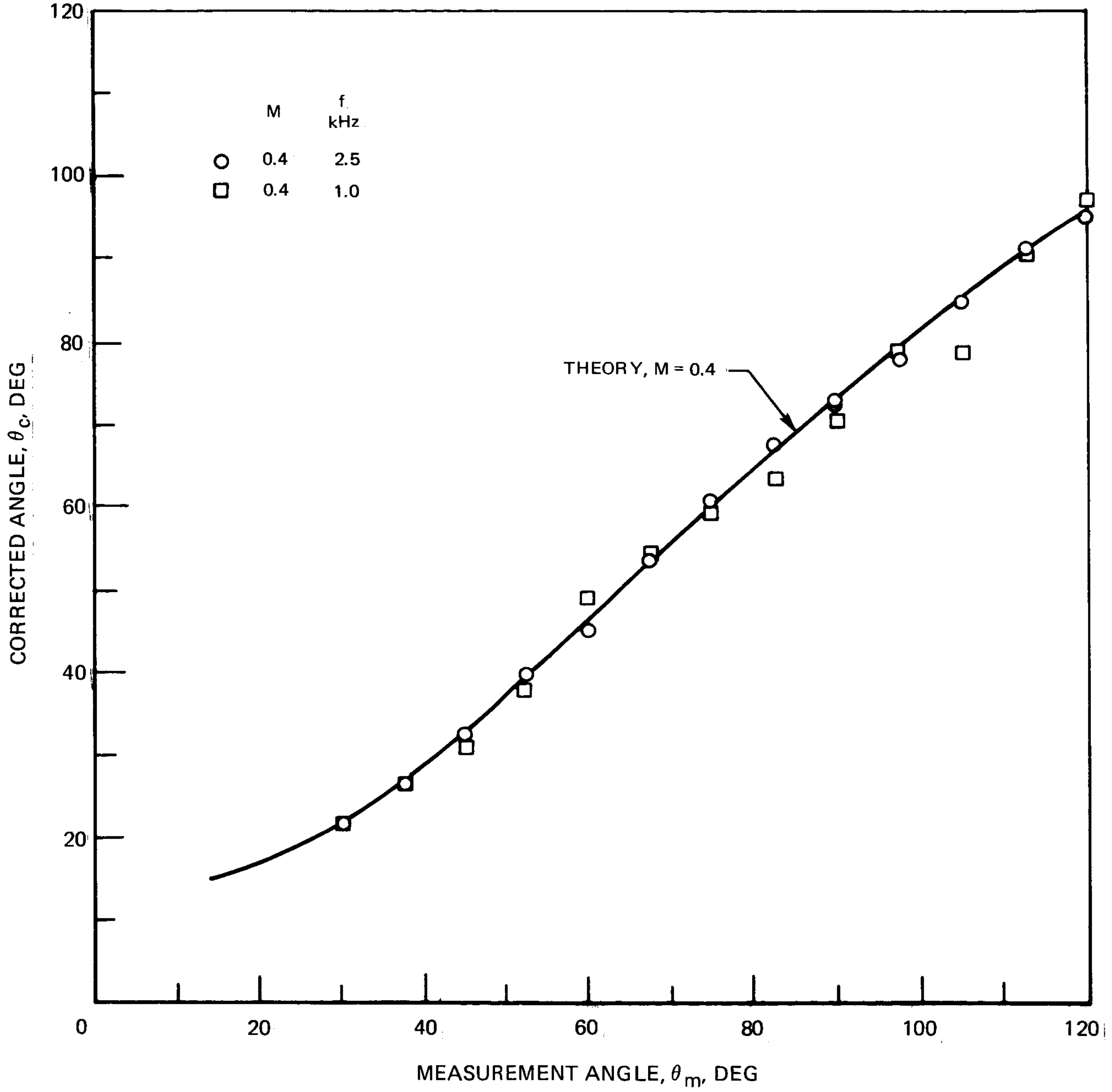

(b) f = 2.5, 1 kHz

Figure 24 — Continued

78–04–76–8

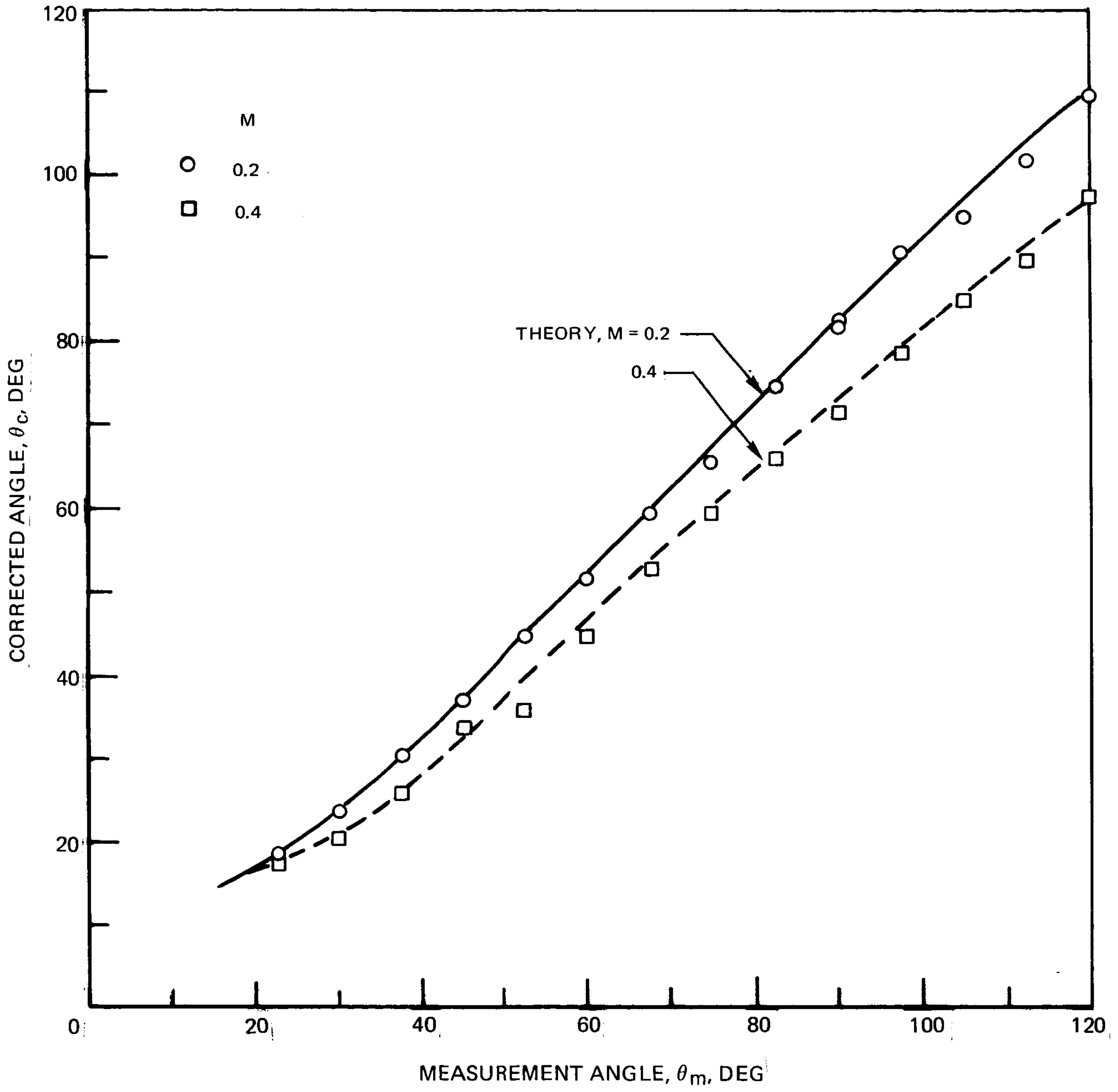

(c) f = 5 kHz

Figure 24 —Concluded

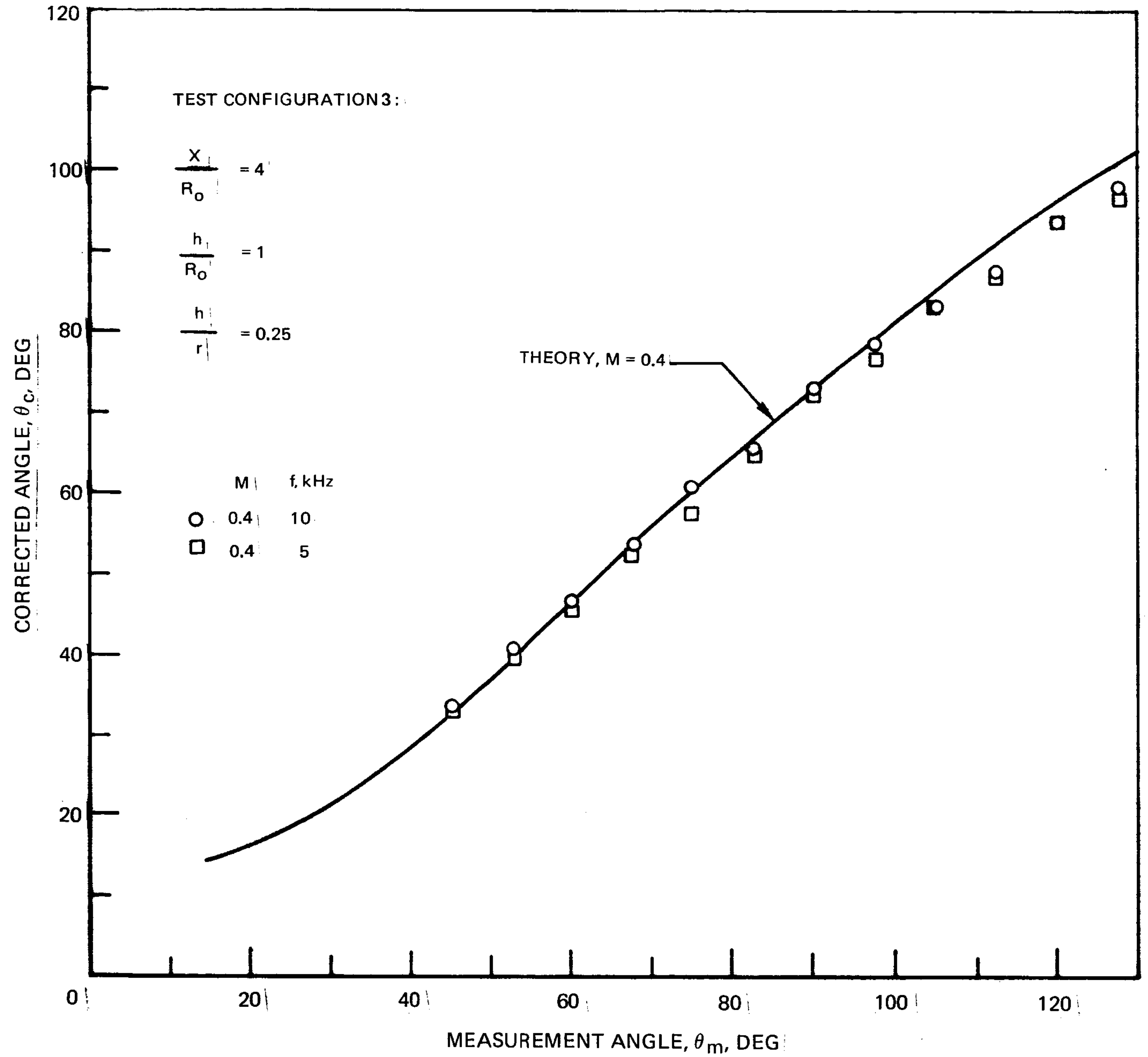

(a) f = 10, 5 kHz

Figure 25—Comparison of Experimental and Theoretical Refraction Angle Correction as a Function of Mach Number and Frequency. Test Configuration 3.

78–04–76–5

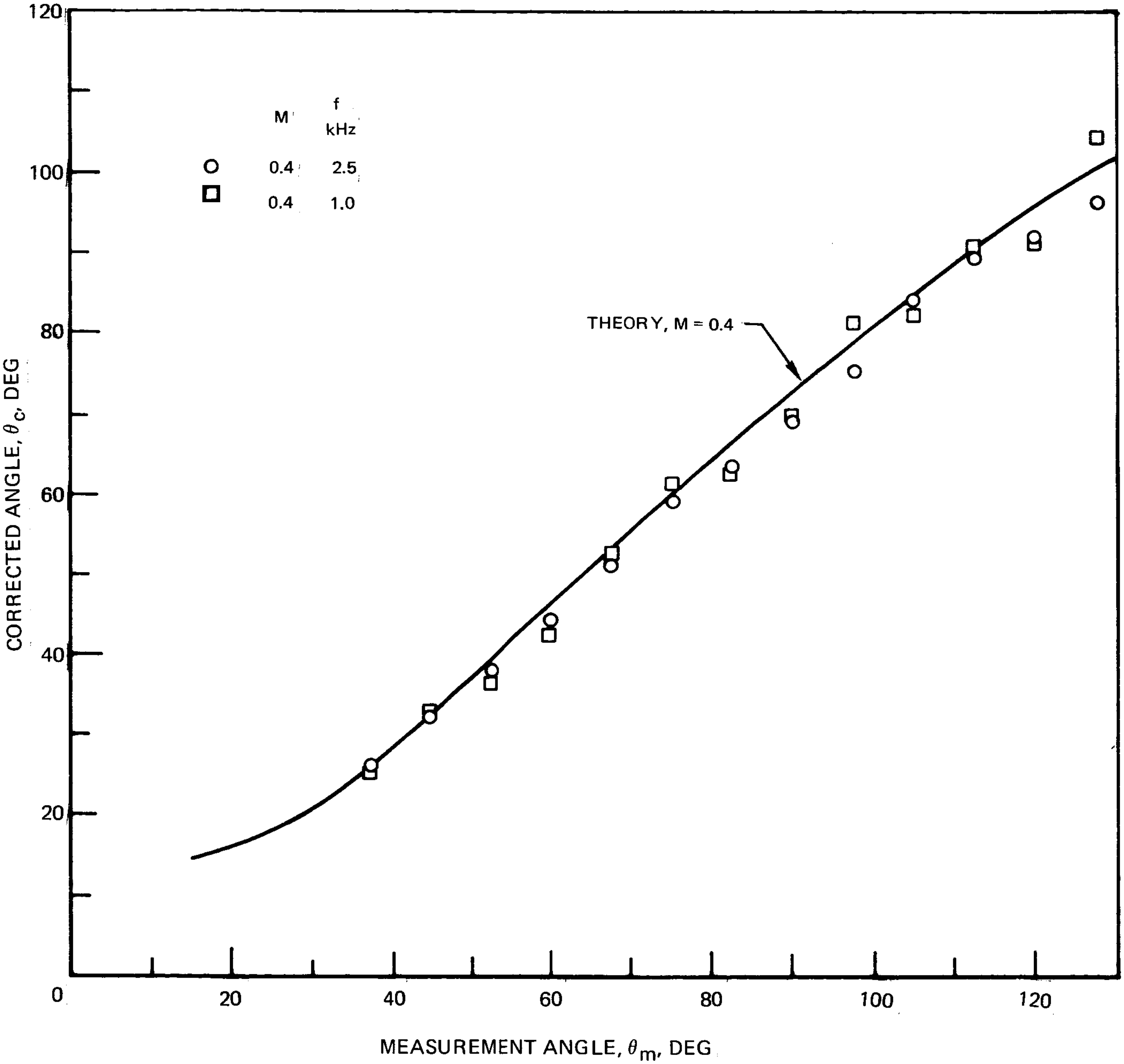

(b) f = 2.5, 1 kHz

Figure 25 – Continued

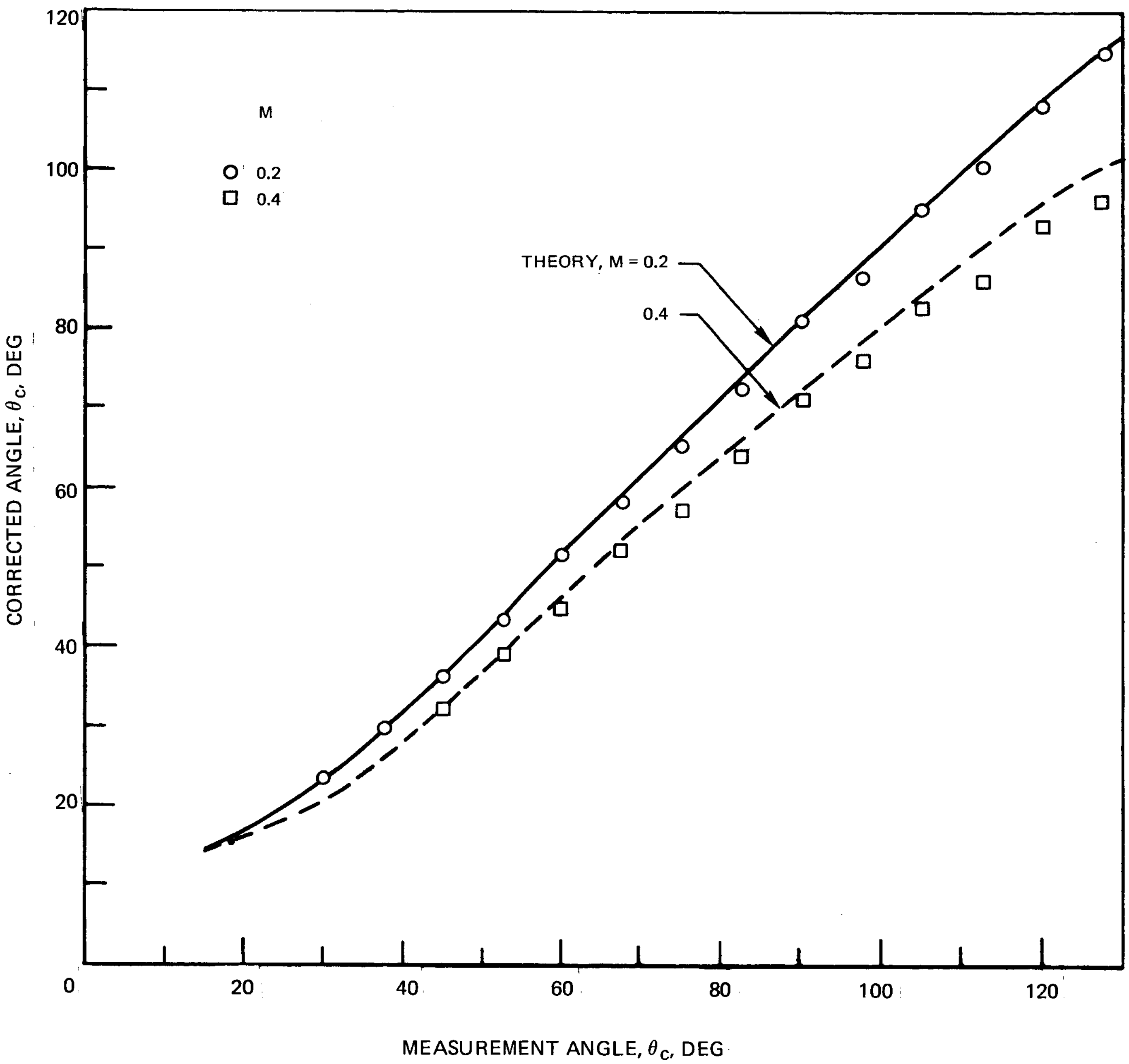

(c) f = 5 kHz

Figure 25—Concluded

78–04–76–6

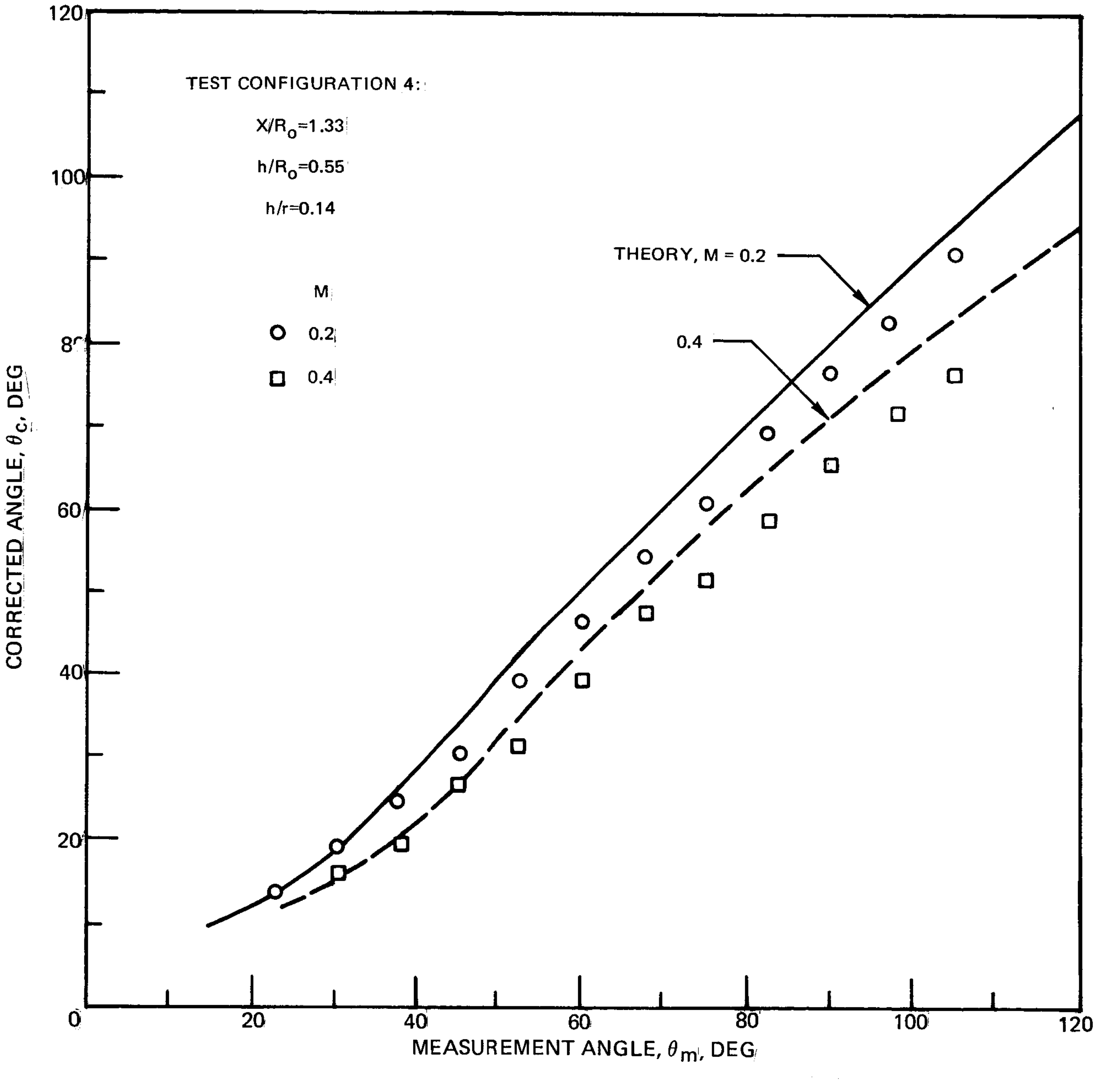

(a) f = 10 kHz

Figure 26.- Comparison of Measured and Theoretical Refraction Angle Correction as a Function of Mach Number and Source Frequency. Test Configuration 4.

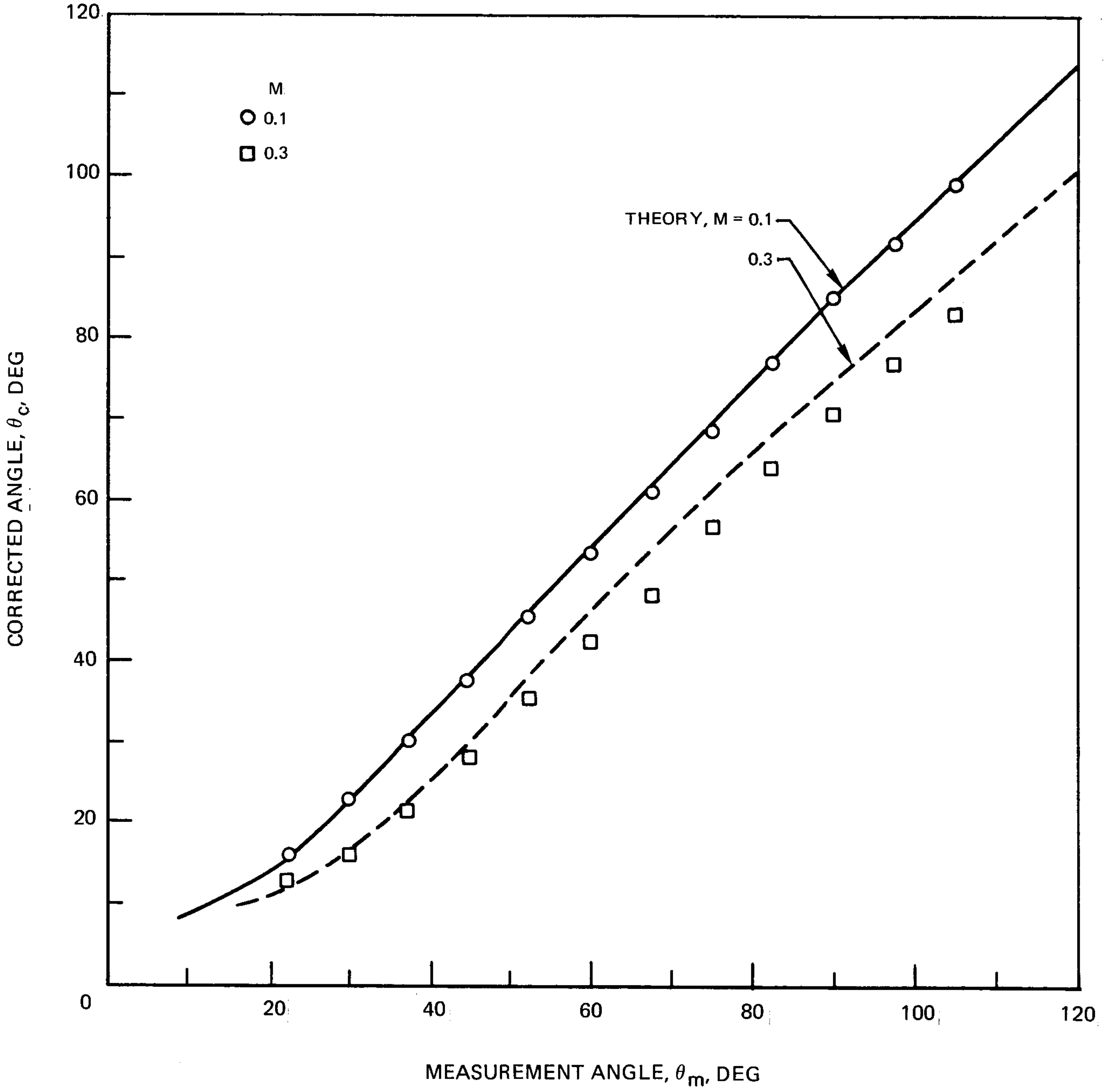

(b) f = 10 kHz

Figure 26— Continued

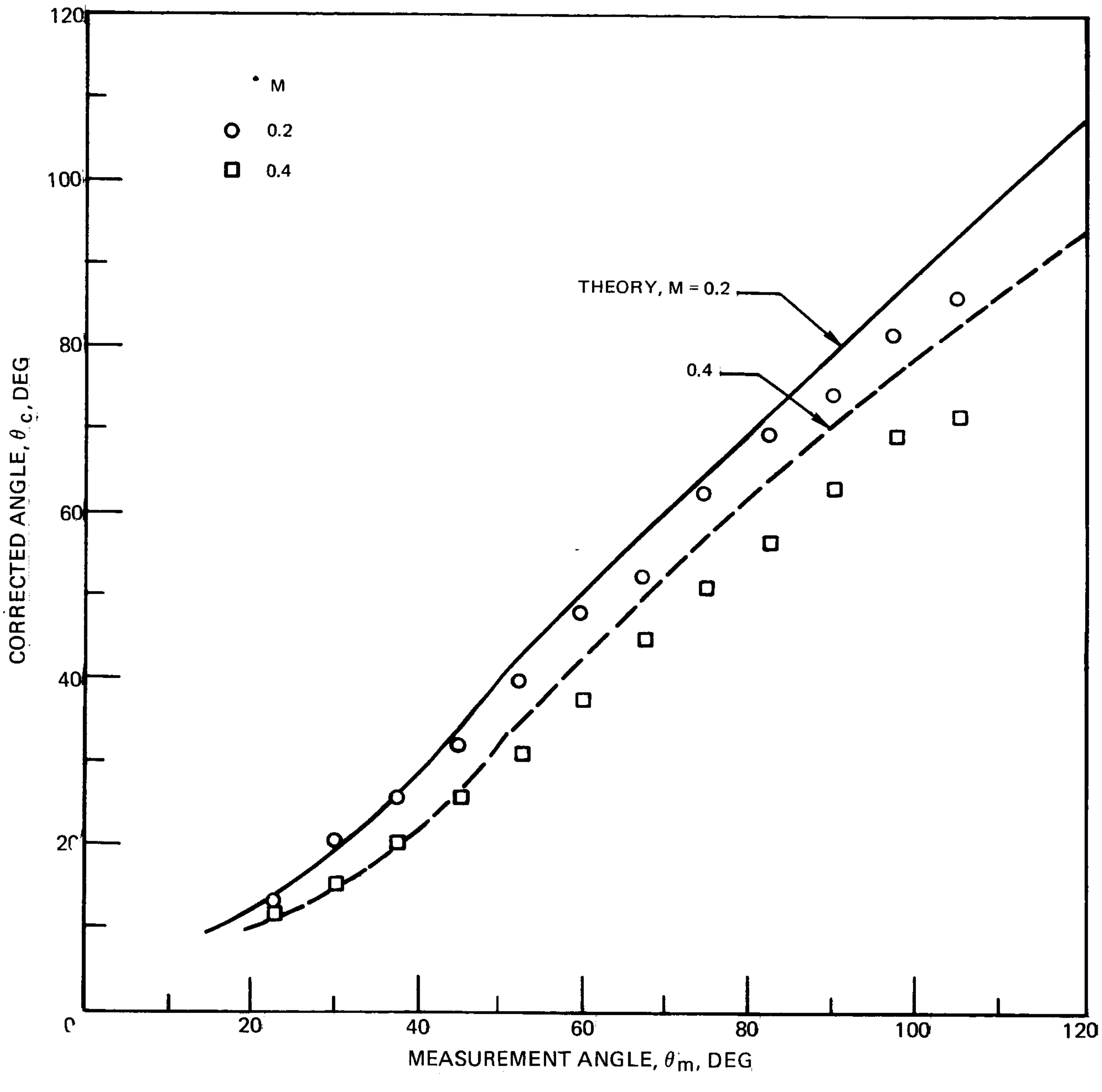

(c) f=5 kHz

Figure 26-Continued

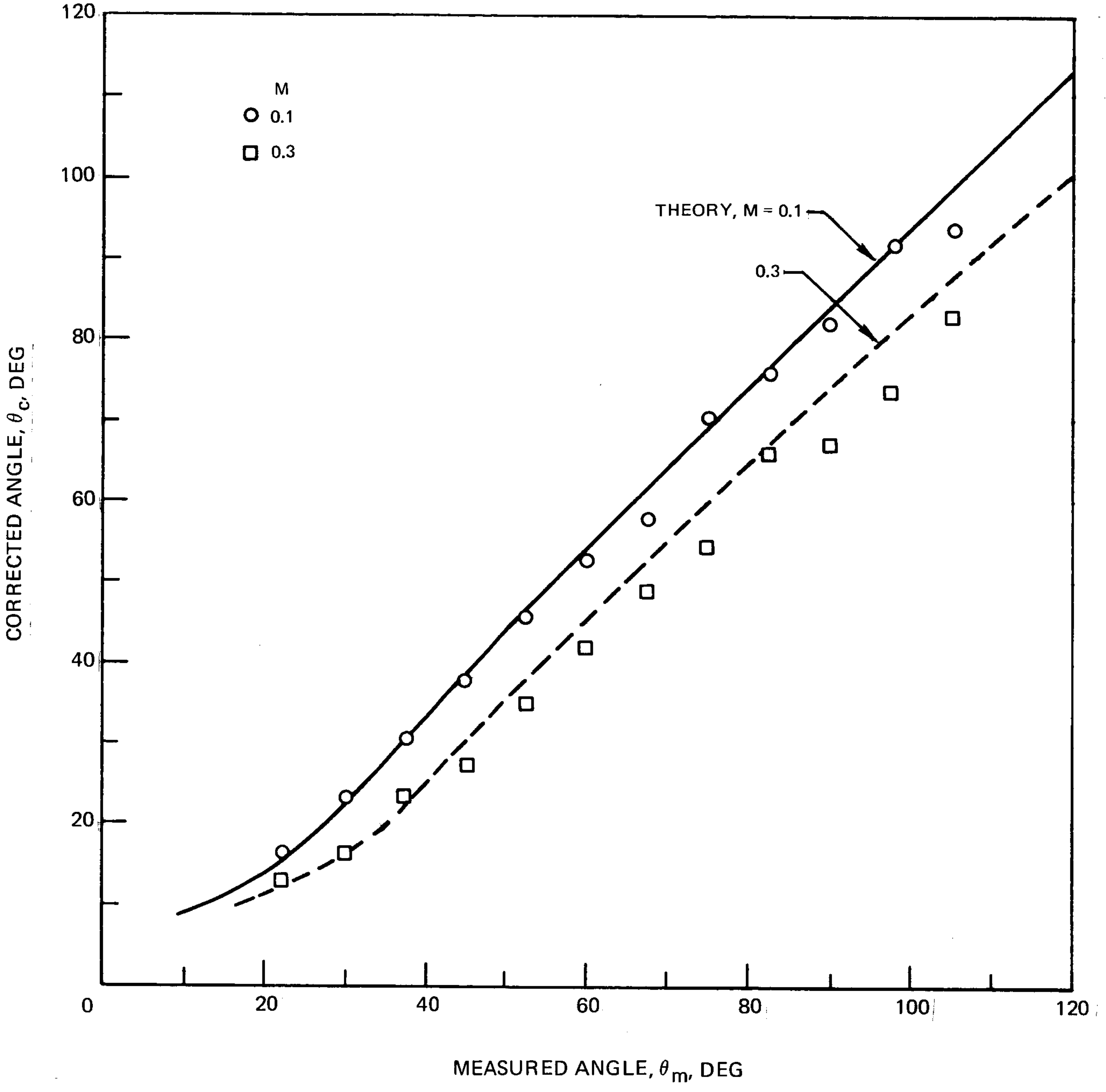

(d) f = 5 kHz

Figure 26– Continued

78–04–116–5

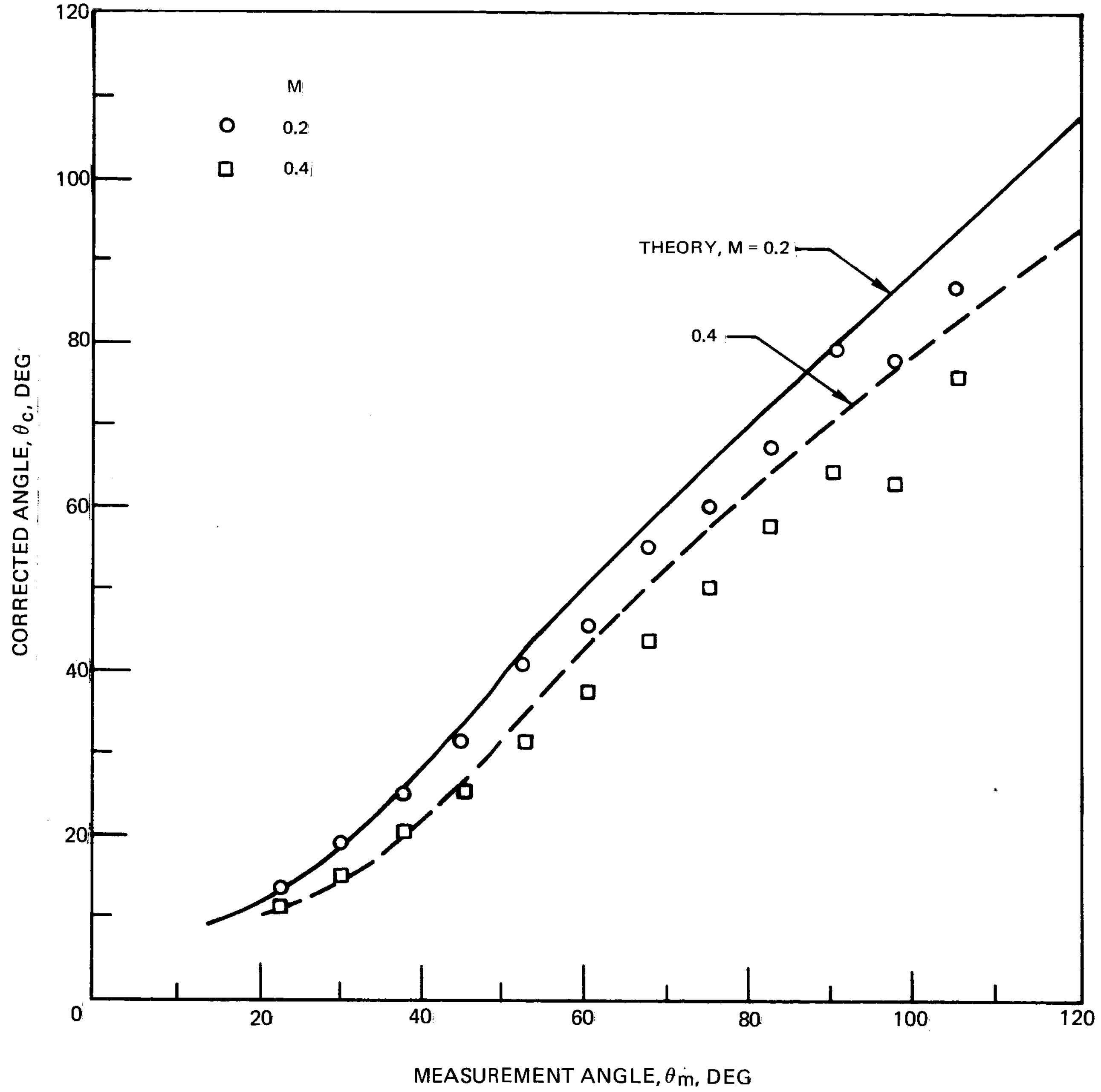

(e) f=2.5 kHz

Figure 26 -Continued

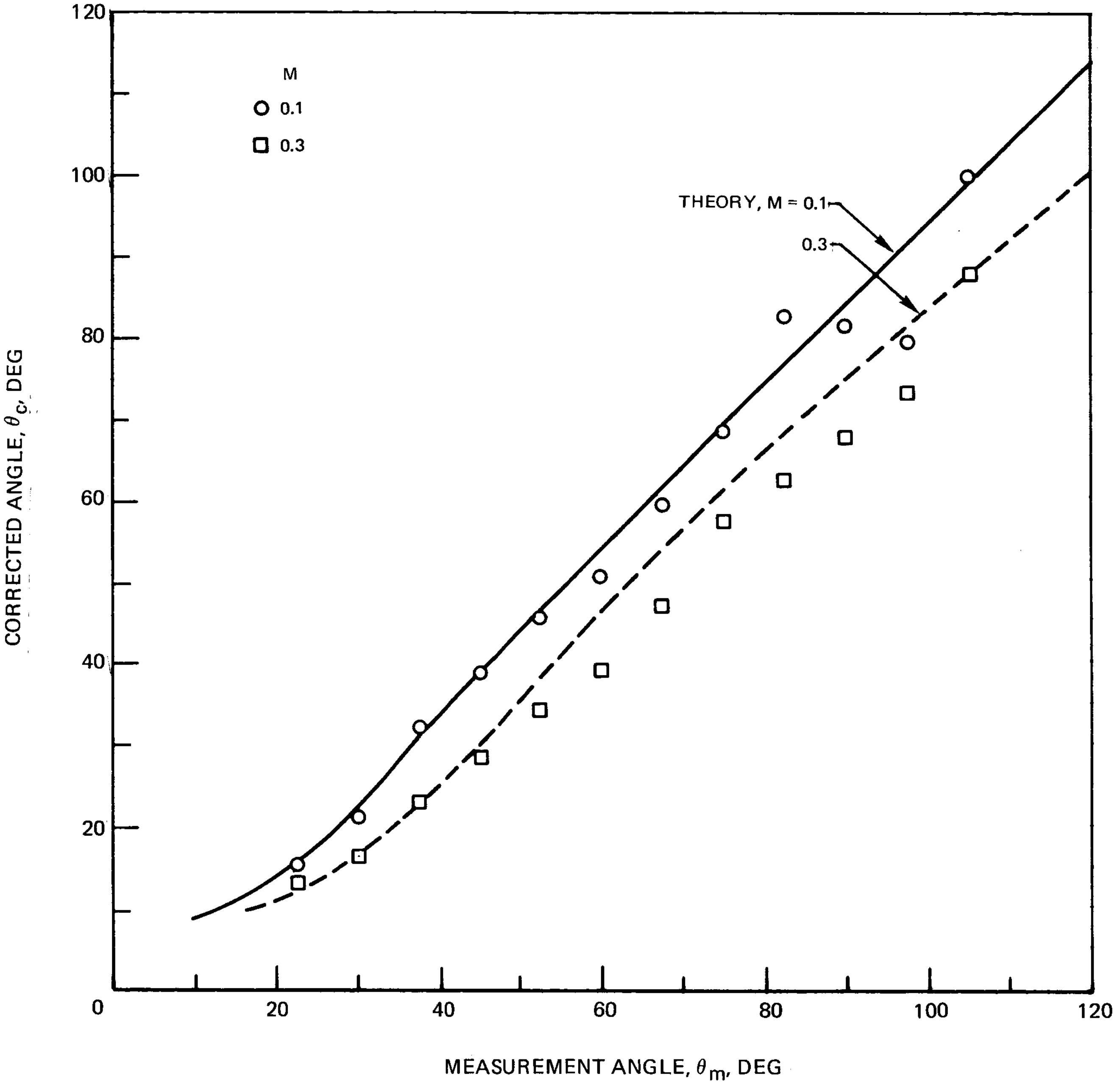

(f) f = 2.5 kHz

Figure 26— Concluded

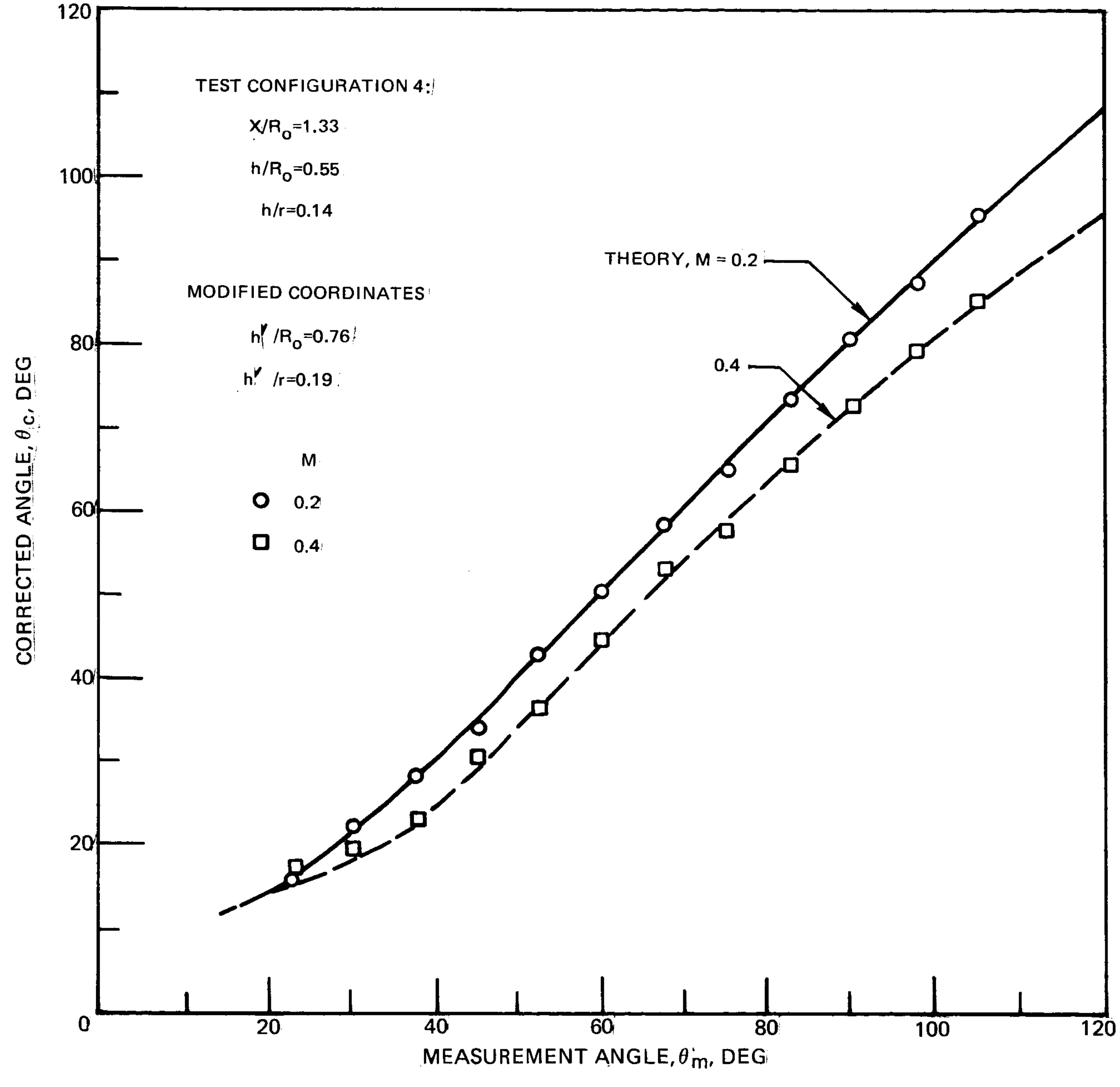

(a) f = 10 kHz

Figure 27-Comparison of Measured and Theoretical Refraction Angle Correction as a Function of Mach Number and Source Frequency Using Modified Source to Shear Layer Separation Distance. Test Configuration 4.

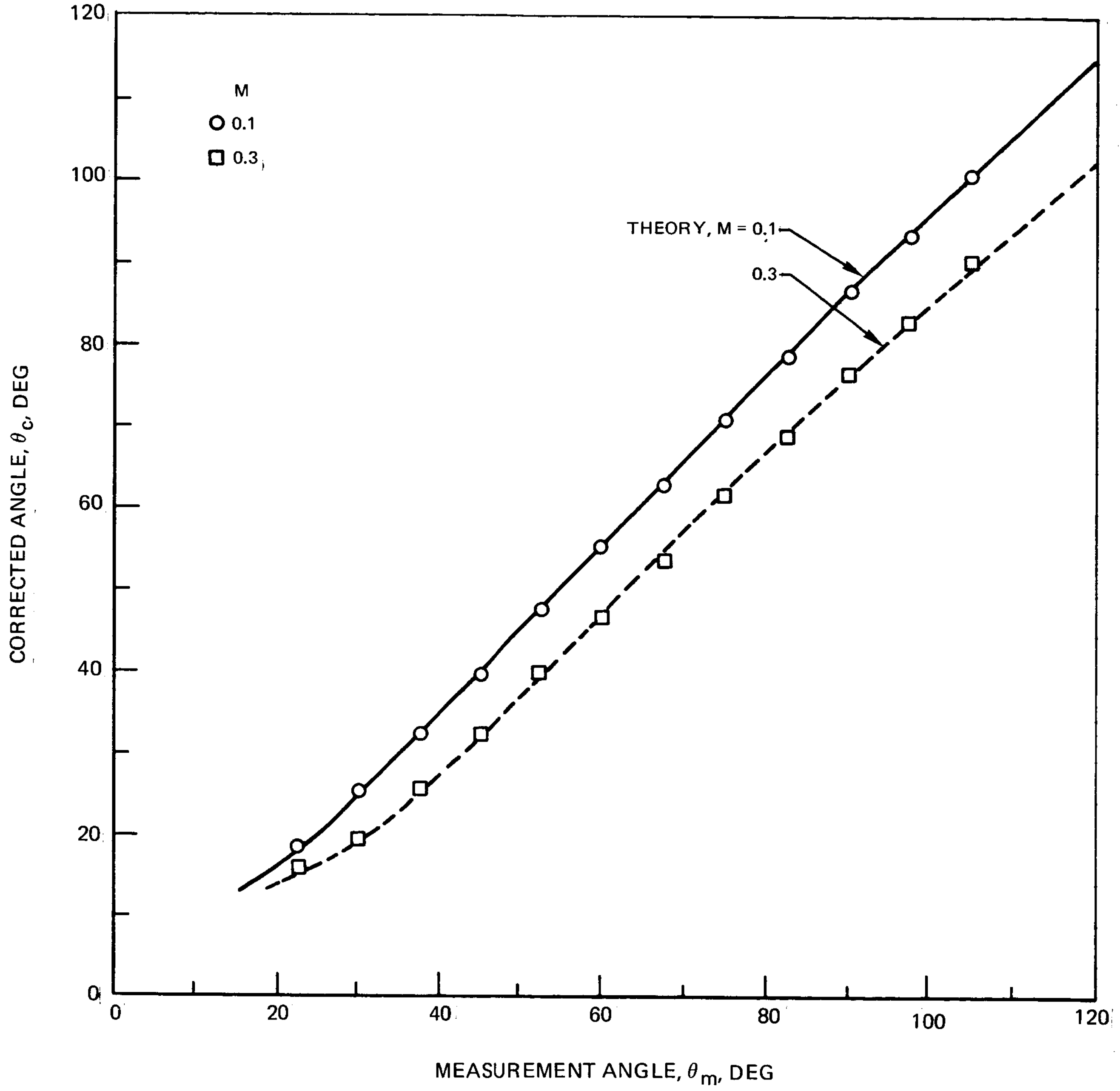

(b) f = 10 kHz

Figure 27 – Continued

78–04–116–3

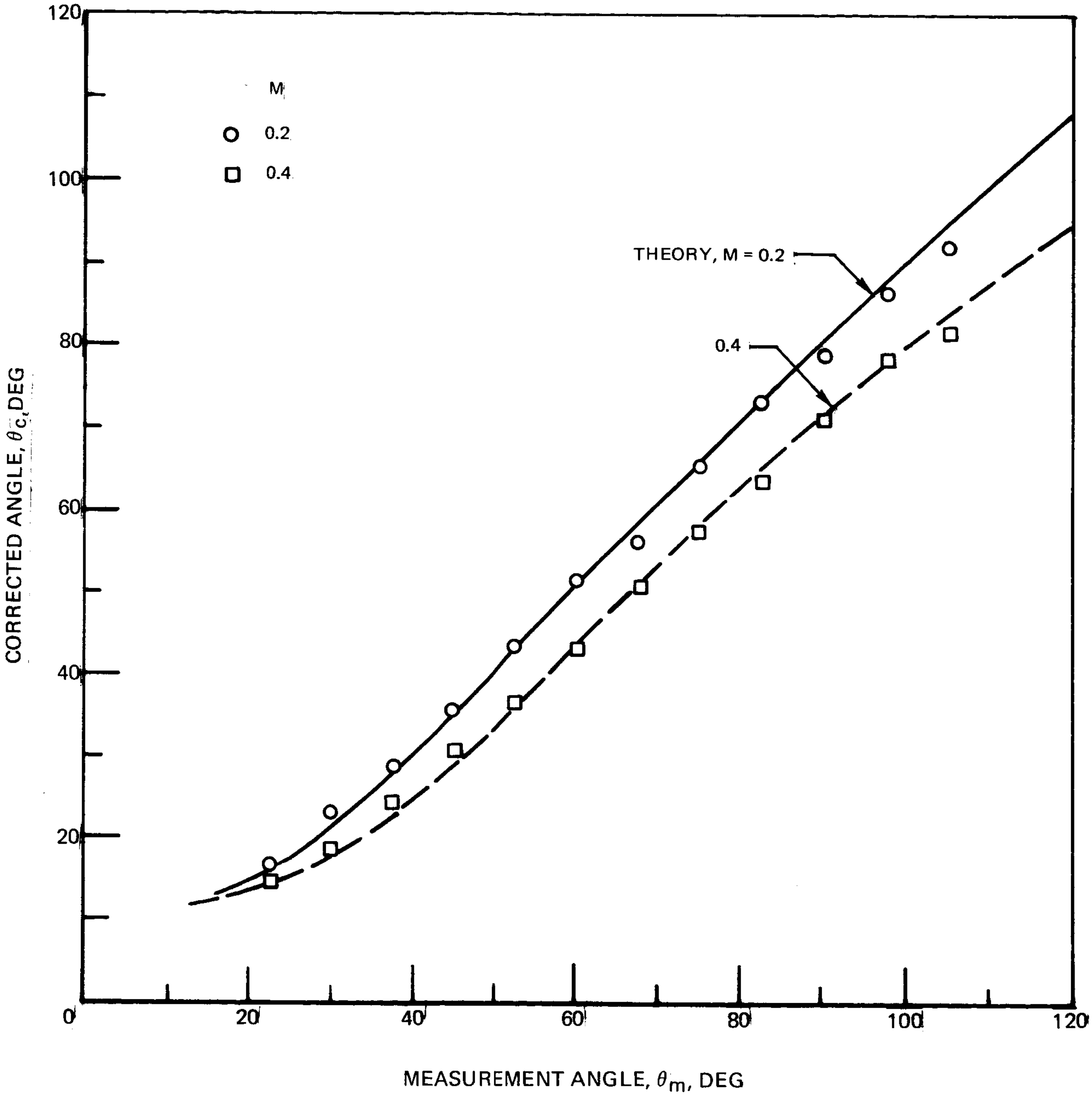

(c) f=5 kHz

Figure 27 -Continued

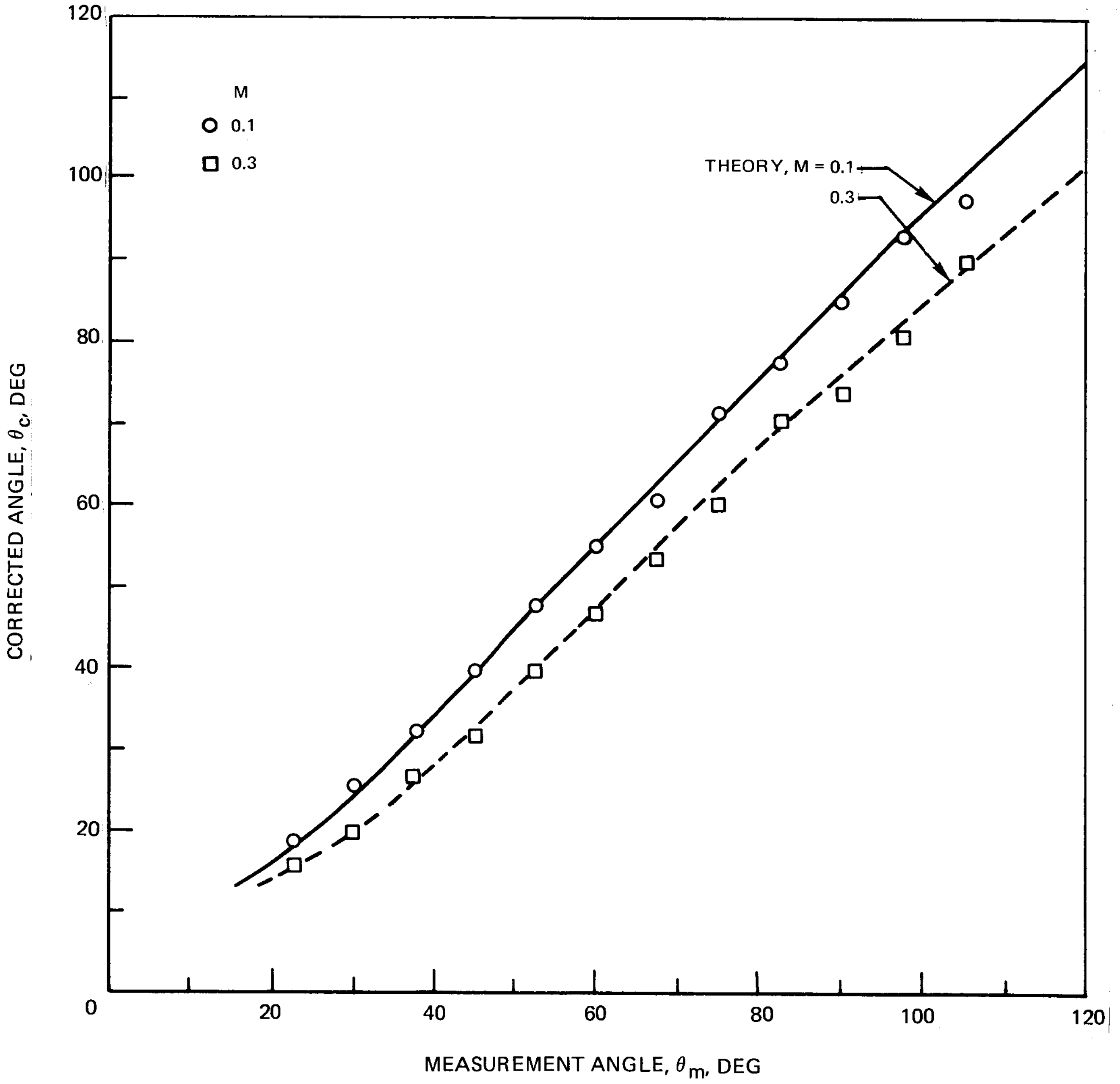

(d) f = 5 kHz

Figure 27– Continued

78–04–116–1

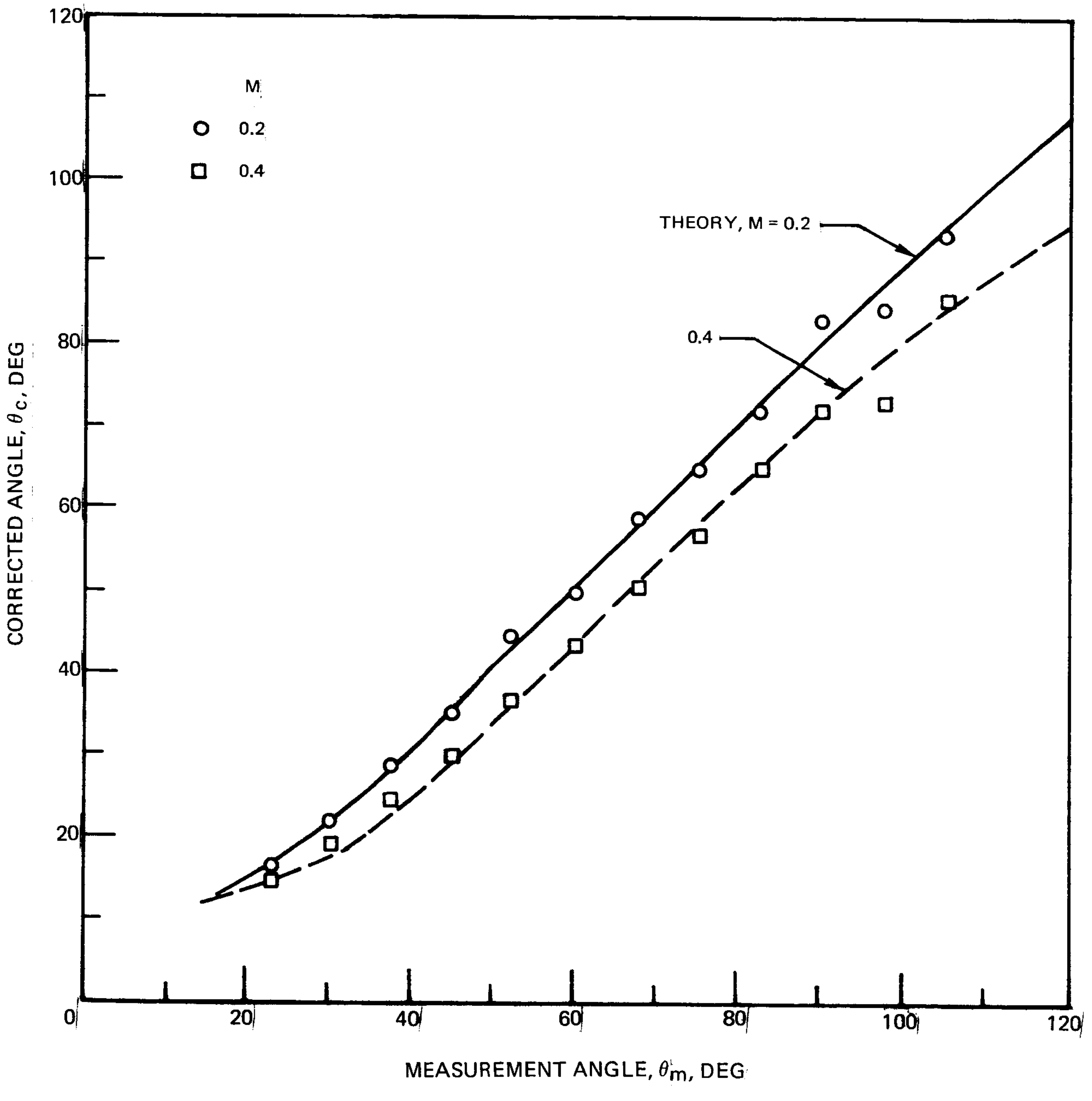

(e) f=2.5kHz

Figure 27-Continued

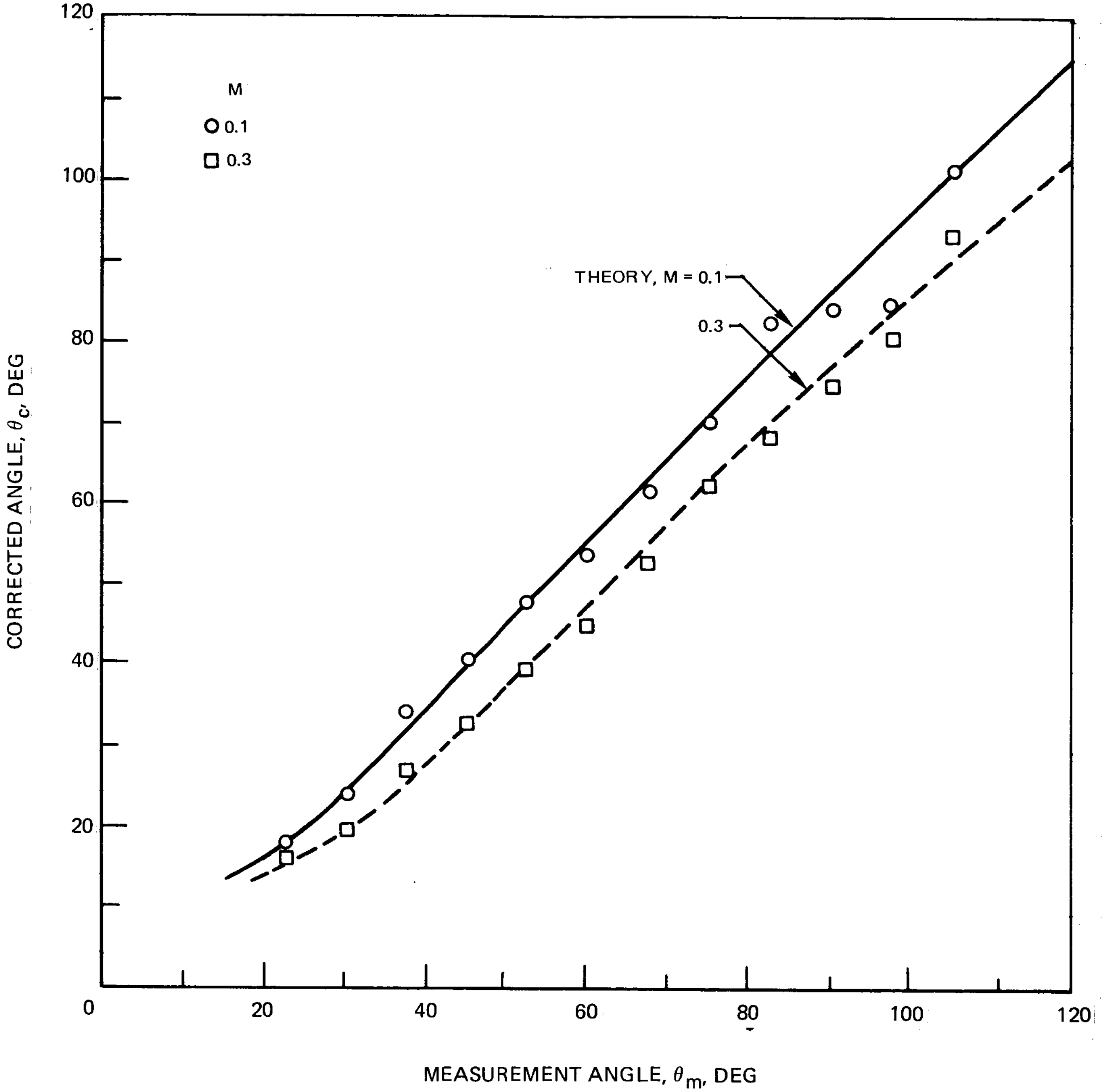

(f) f = 2.5 khz

Figure 27— Concluded

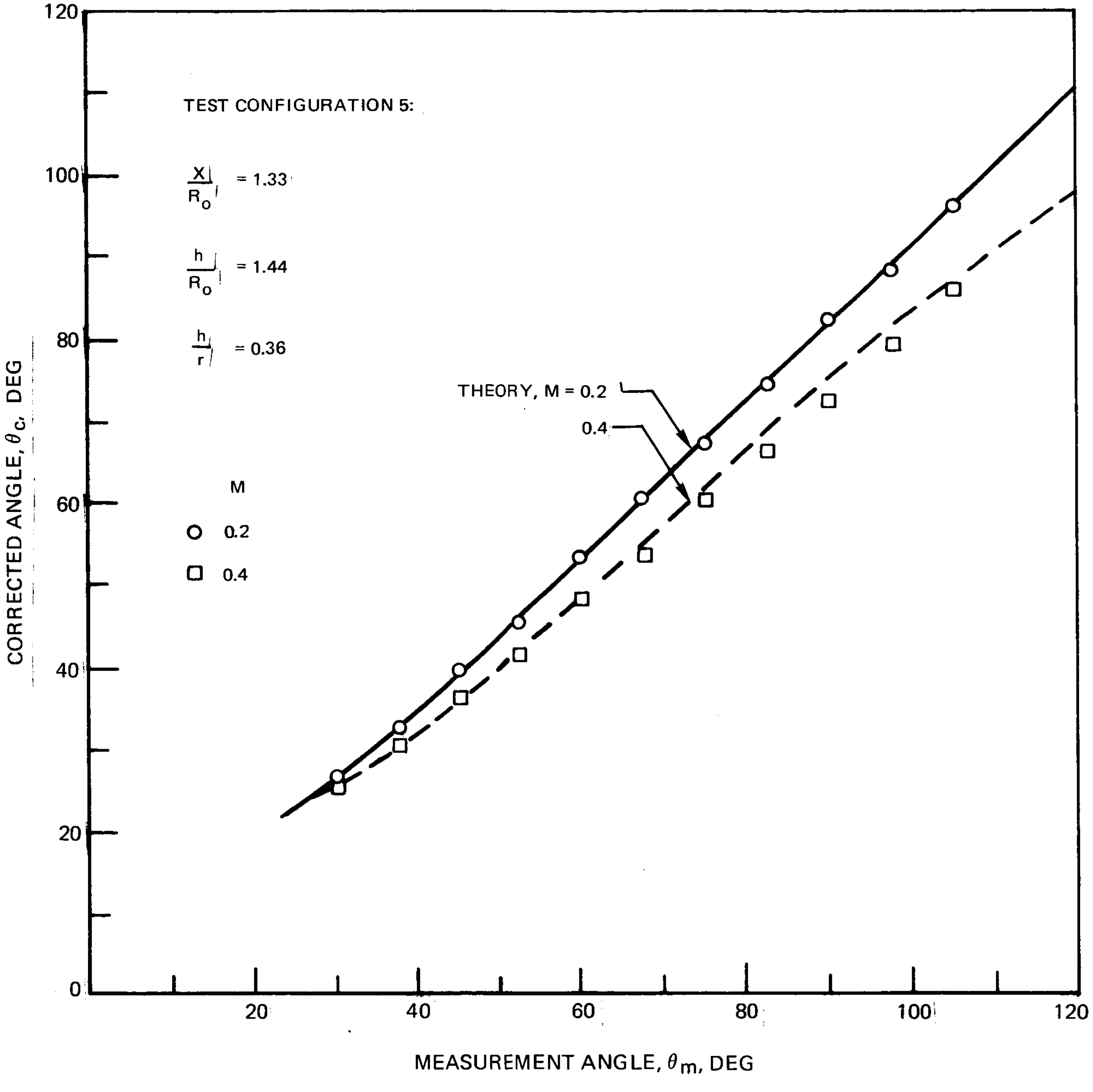

(a) f = 10 kHz

Figure 28 – Comparison of Experimental and Theoretical Refraction Angle Correction as a Function of Mach Number and Frequency. Test Configuration 5.

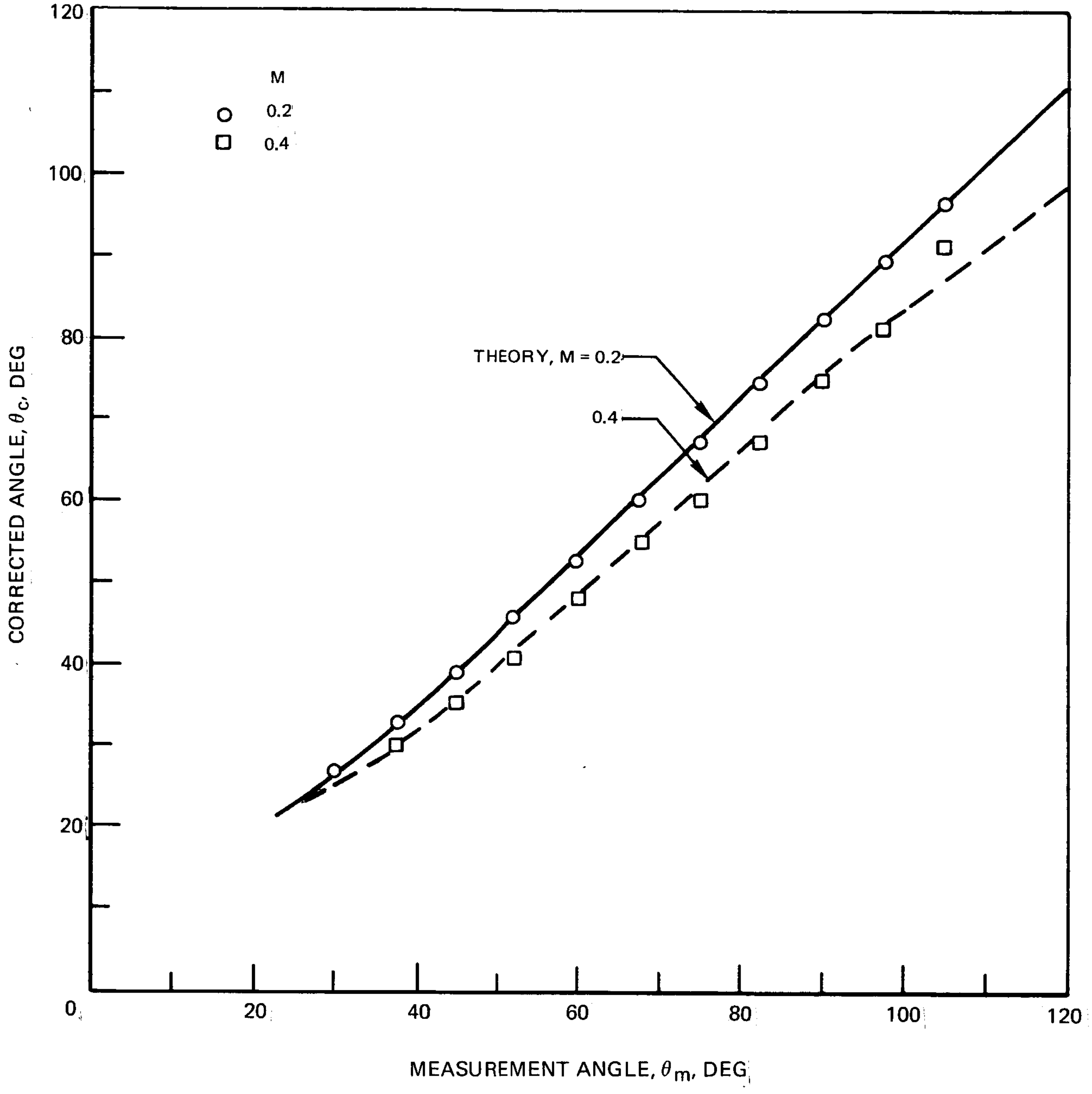

(b) f = 5 kHz

Figure 28—Concluded

78—04—76—7

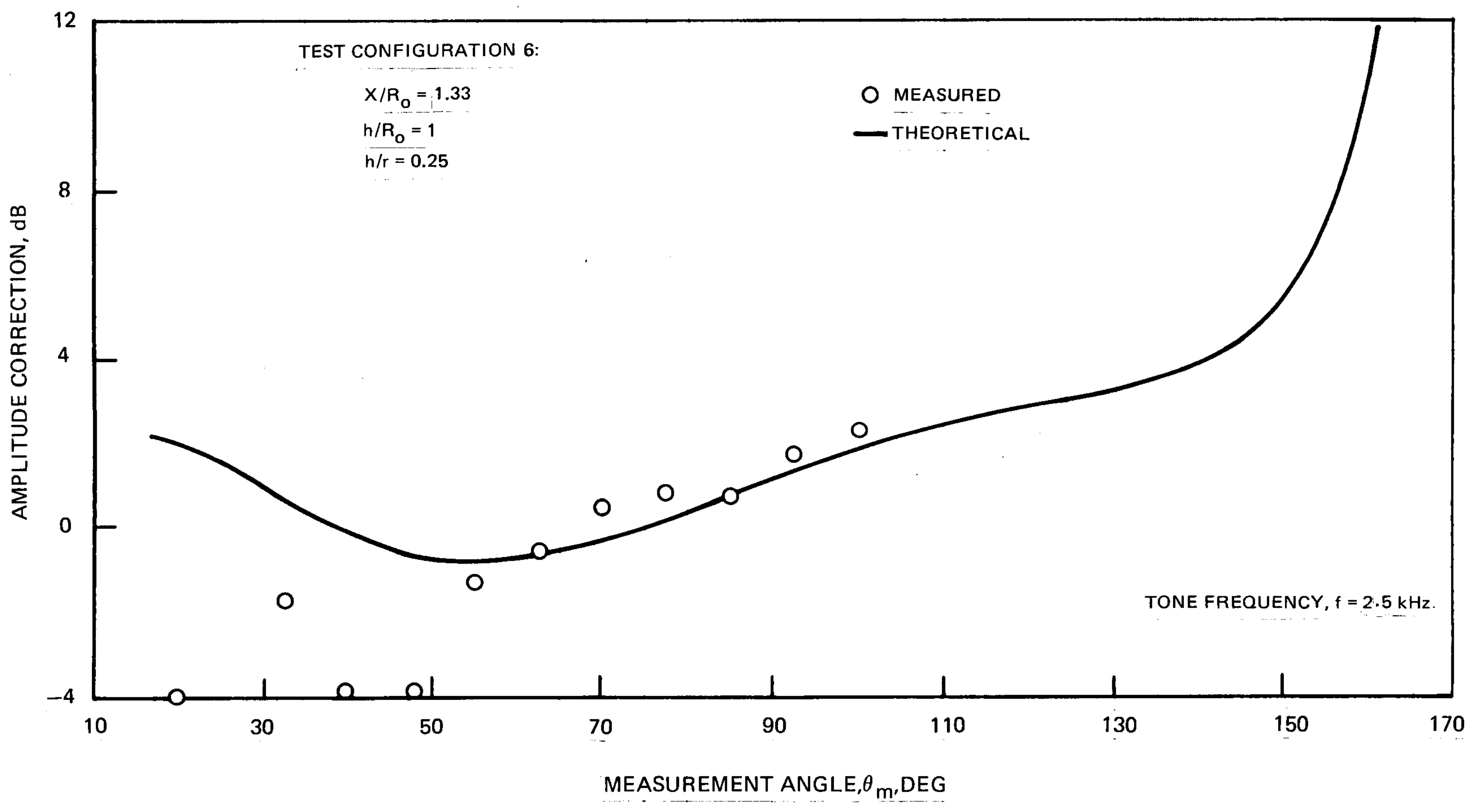

Figure 29—Comparison of Measured and Theoretical Amplitude Refraction Correction at Mach Number, M = 0.42, Test Configuration 6.

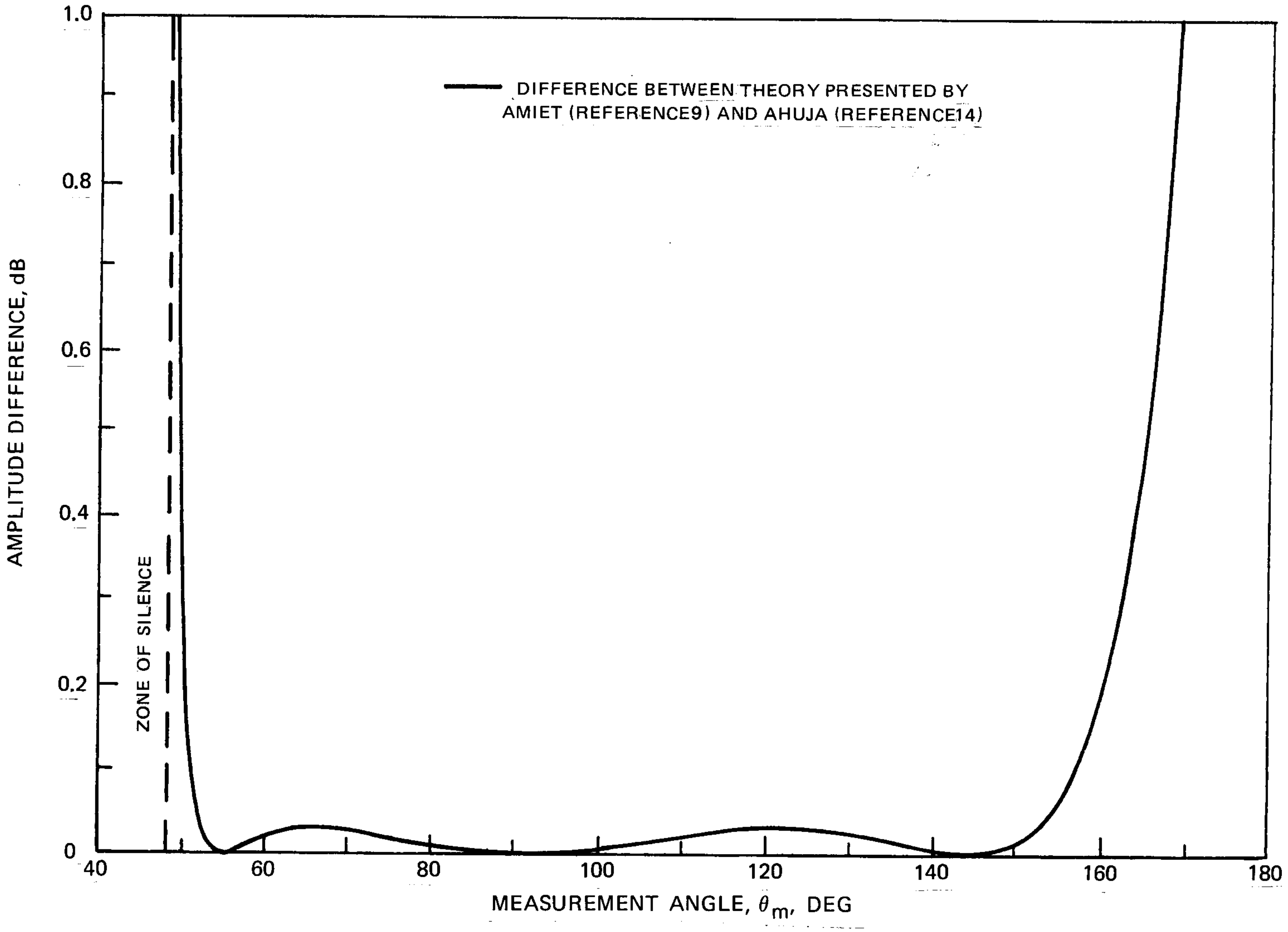

Figure 30—Amplitude Difference Between Existing Refraction Amplitude Correction Theories, Mach Number, M = 0.5, Source on Jet Centerline

77–11 –94–3

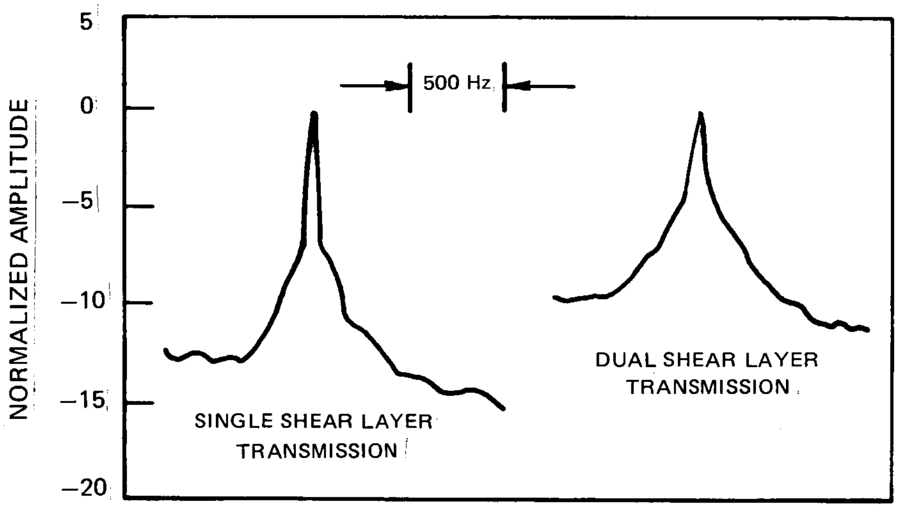

Figure 31 —Effect of Single and Dual Shear Layer Transmission on Discrete Tone Frequency Spectrum at Mach Number, M = 0.4, Frequency, f = 10 kHz, and Axial Source Location $X/R_o = 1.33$

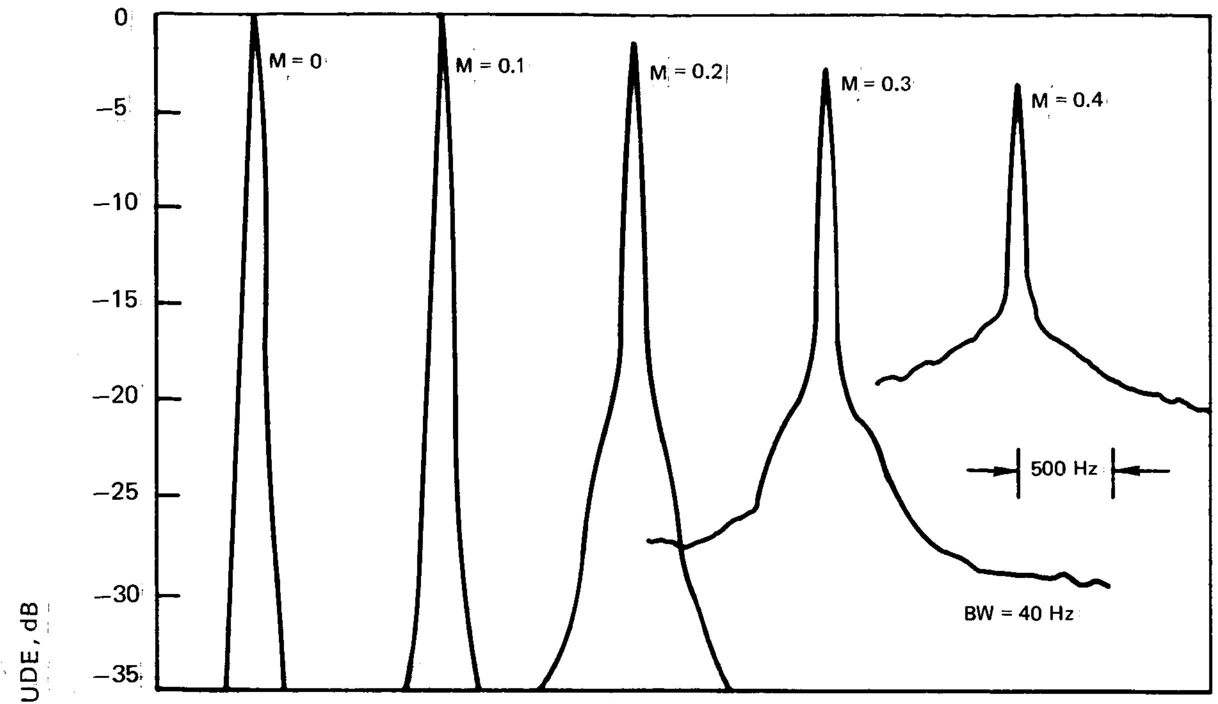

(a) f = 5 kHz

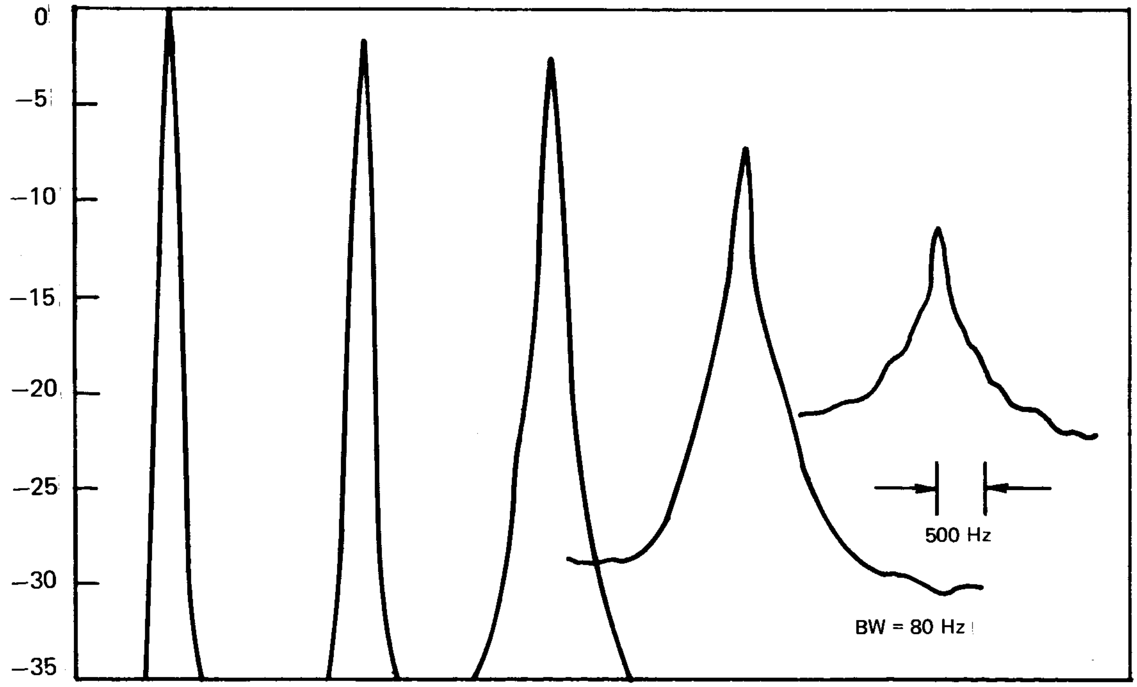

(b) f = 10 kHz

Figure 32–Variation of Discrete Tone Spectrum with Mach Number and Frequency at Axial Source Location $X/R_O = 1.33$

78–04–96–6

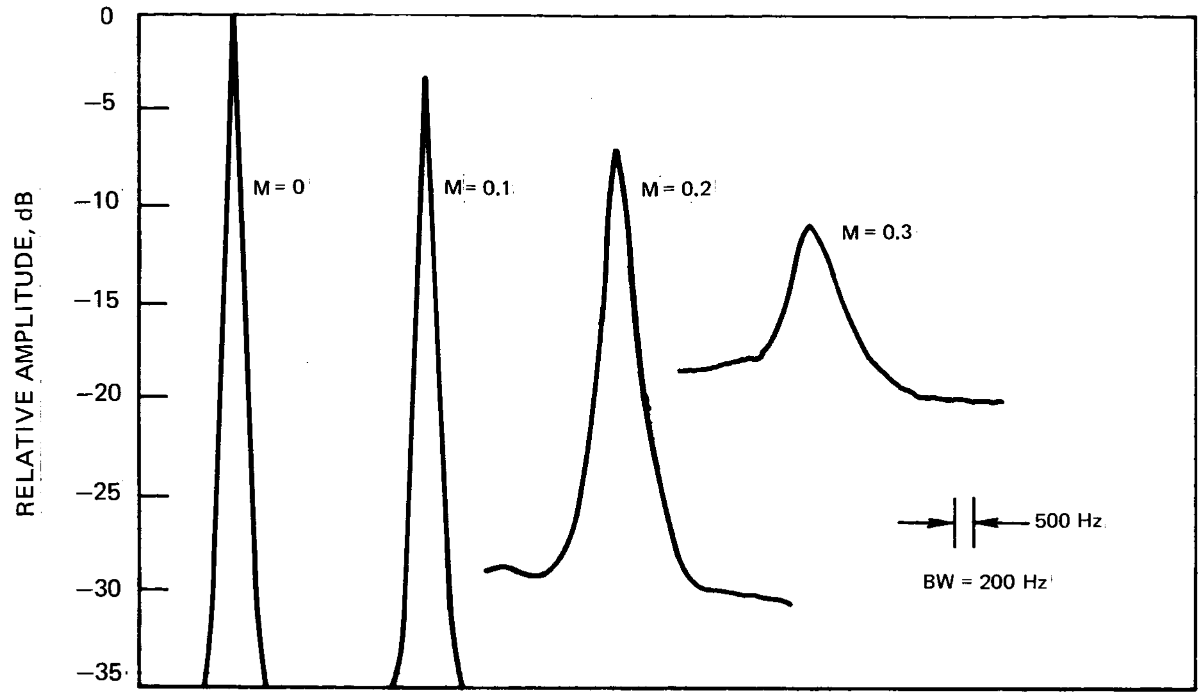

(c) f = 17.5 kHz

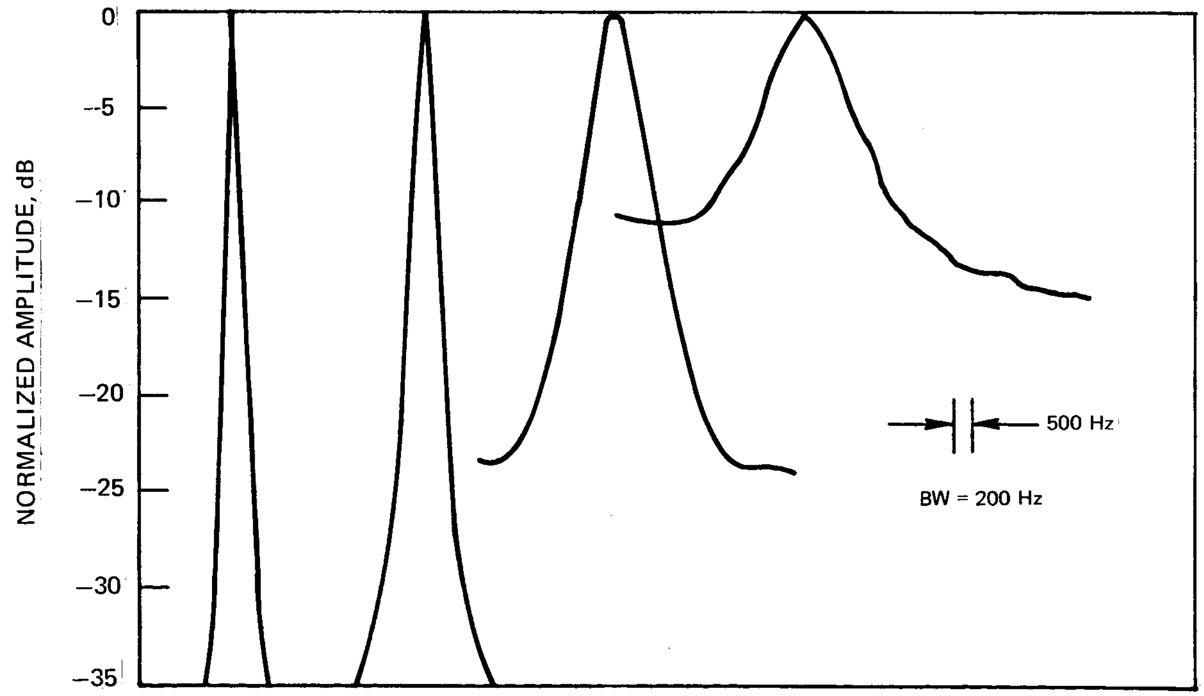

(d) f = 25 kHz

Figure 32—Concluded

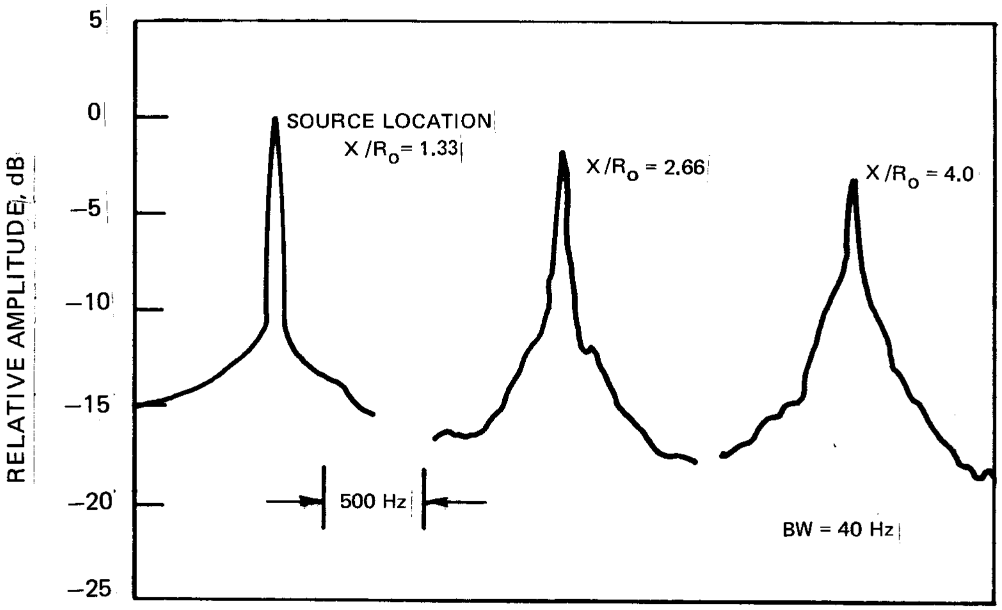

Figure 33—Variation of Discrete Tone Spectrum with Axial Source Location for Mach Number, M = 0.4, and Frequency, f = 5 kHz

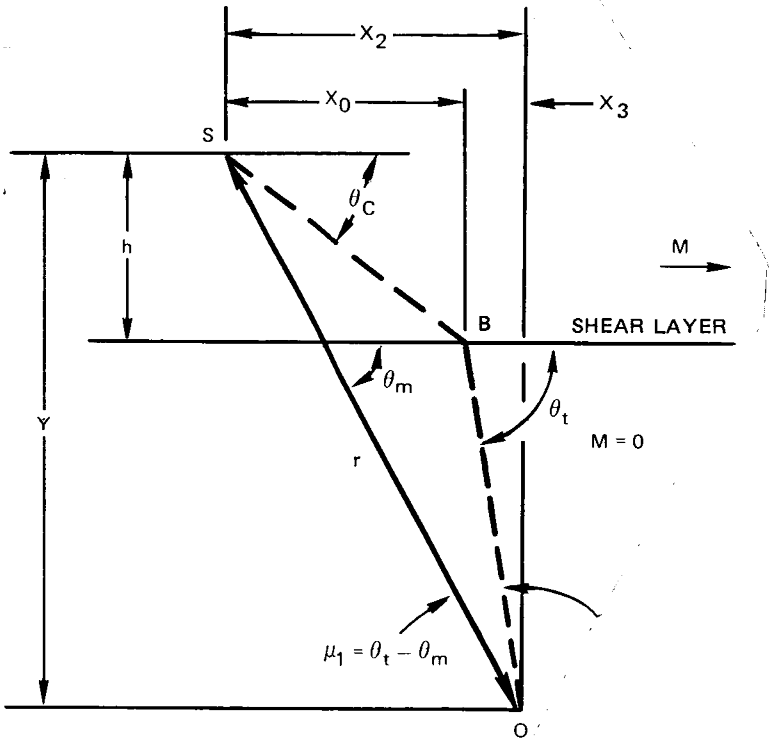

Figure 34 — Geometry for Angle Correction Calculation

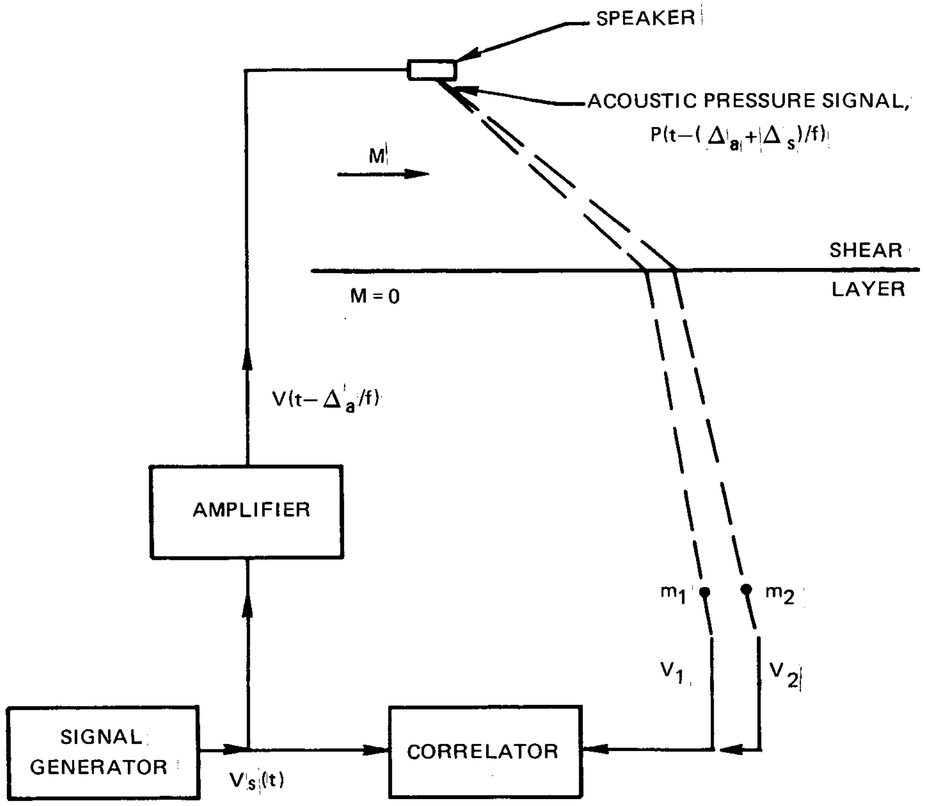

$$V_2 = V_2(t - (\delta + \Delta_2)/f)$$

$$V_1 = V_1(t - (\delta + \Delta + \Delta_1)/f)$$

$$\Lambda = \Delta_a + \Delta_s + \Delta_p$$

Figure 35–Schematic Showing Phase Lag Between Signal Generator and Far–Field Microphone Output

78–04–96–1